České vysoké učení technické v Praze
Fakulta stavební

Katedra mechaniky
Obor: Konstrukce pozemních staveb

Experimentální ověření vlivu tloušťky 3D tištěných vzorků na parametry lomové houževnatosti

Experimental verification of the influence of thickness on 3D printed samples on fracture toughness parameters
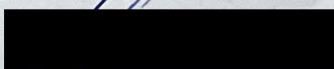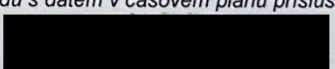
DIPLOMOVÁ PRÁCE

Vypracoval:	Bc. Petr Bočan
Vedoucí práce:	doc. Ing. Aleš Jíra, Ph.D.
Rok:	2024

ČESKÉ VYSOKÉ UČENÍ TECHNICKÉ V PRAZE
Fakulta stavební
Thákurova 7, 166 29 Praha 6

ZADÁNÍ DIPLOMOVÉ PRÁCE
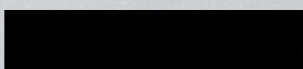
I. OSOBNÍ A STUDIJNÍ ÚDAJE

Příjmení: Bočan   Jméno: Petr   Osobní číslo: 486173

Zadávající katedra: katedra mechaniky - K132

Studijní program: Stavební inženýrství

Studijní obor/specializace: Konstrukce pozemních staveb

II. ÚDAJE K DIPLOMOVÉ PRÁCI

Název diplomové práce: Experimentální ověření vlivu tloušťky 3D tištěných vzorků na parametry lomové houževnatosti

Název diplomové práce anglicky: Experimental Verification of the Influence of Thickness on 3D Printed Samples on Fracture Toughness Parameters.

Pokyny pro vypracování:
Práce bude obsahovat zejména:
- teoretický úvod pro experimentální ověření a výpočet parametrů lomové houževnatosti;
- přehled materiálových parametrů materiálů využitelných v bioaplikacích (zejména Ti6al4V);
- popis a vlastní realizace experimentálních měření, včetně přípravy vzorků;
- vyhodnocení experimentálního měření s cílem porovnat vliv tloušťky vzorků na parametry lomové houževnatosti;
- rozpracovat možnosti numerického modelování provedených experimentů pro vzájemnou verifikaci.
- závěrečné shrnutí.
Práce bude primárně zaměřena na experimentální měření, včetně přípravy vzorků a efektivního uspořádání měřící linky se zapojením metody microDIC. Cílem je určit případnou závislot měřených paramatrů ovlivněých nekvalitou tisku u velmi tenkých vzorků.

Seznam doporučené literatury:
odborné články a publikace dostupné v databázích WoS a Scopus
3D modelování v prostředí CAD
technologické postupy použitého přístrojového vybavení (3D SLS a SLA tisk, pneumatický a elektromechaniký lis, microDIC Dantec)

Jméno vedoucího diplomové práce: doc. Ing. Aleš Jíra, Ph.D.

Datum zadání diplomové práce: 27.9.2023   Termín odevzdání DP v IS KOS: 8.1.2024
                                                  Údaj uveďte v souladu s datem v časovém plánu příslušného ak. roku

_____   _____
Podpis vedoucího práce   Podpis vedoucího katedry

III. PŘEVZETÍ ZADÁNÍ

Beru na vědomí, že jsem povinen vypracovat diplomovou práci samostatně, bez cizí pomoci, s výjimkou poskytnutých konzultací. Seznam použité literatury, jiných pramenů a jmen konzultantů je nutné uvést v diplomové práci a při citování postupovat v souladu s metodickou příručkou ČVUT „Jak psát vysokoškolské závěrečné práce" a metodickým pokynem ČVUT „O dodržování etických principů při přípravě vysokoškolských závěrečných prací".

27.04.2023   _____
_____
Datum převzetí zadání   Podpis studenta(ky)

Conflict of Interest Statement

As the author of this master thesis, I declare no conflict of interest. I claim to have written this master thesis solely myself, provided with professional consultations from my supervisor doc. Ing. Aleš Jíra, Ph.D.

I also declare that all literature and materials used in the writing of this master thesis are properly cited in the References chapter.

On the day ....

Bc. Petr Bočan

Acknowledgment

Abstrakt: V současnosti se v biomedicínských aplikacích hojně zkoumají technologie aditivní výroby. Technologie 3D tisku přináší velké výhody tomuto průmyslu, protože díky ní lze vyrobit složité a rozmanité tvary. Problém však nastává u velmi tenkých vzorků, kde tato technologie stále není dokonalá a vykazuje poměrně velkou nejistotu a defekty výroby. V této práci se zabývám především biomateriály z kovu a polymeru, které jsou využívány pro výrobu náhrad a implantátů. Hlavním aspektem této práce je testování lomové houževnatosti u velmi tenkých vzorků vyrobených pomocí 3D tisku technologií SLS. V práci je podrobně popsána výroba vzorků, návrh a průběh experimentu s následným vyhodnocením hodnot a porovnáním s hodnotami z numerického modelu.

Klíčová slova: Lomová mechanika, 3D tisk, biomateriály, numerická analýza, korelace digitálního obrazu

Abstract: Currently, additive manufacturing technologies are being widely explored in biomedicinal applications. 3D printing technology brings great benefits to this industry as it can produce complex and diverse shapes. The problem then arises with very thin samples, where this technology is still not perfect and shows relatively large uncertainty and manufacturing defects. In this thesis, I am mainly concerned with metal and polymer biomaterials that are used for the fabrication of replacements and implants. The main aspect of this thesis is to test the fracture toughness of very thin specimens fabricated by 3D printing using SLS technology. The fabrication of the specimens, the design and the experiment procedure are described in detail, followed by evaluation of the values and comparison with the values from the numerical model.

Key words: Fracture mechanics, 3D printing, biomaterials, numerical analysis, digital image correlation

Contents

List of Figures

List of Tables

Introduction

In today's era of rapidly advancing technology and innovation, 3D printing has an indispensable place in manufacturing and scientific research across engineering disciplines. Material engineering and biomedicinal application are one of the key areas where this technology is being used. Titanium alloy 3D printing technology enables to creation of any shape of future implant, the design of an optimized surface and the fast individual manufacture of a specific replacement for a specific patient. A significant benefit of the technology is the ability to create an ideal porous structure on the implant surface. This surface can be designed to promote osteointeraction as much as possible, which helps to stabilize the implant in bone for long term, and guarantee its function and lifespan. Considering the size of implant (for example, dental implants have a body length 10 – 15 mm and diameter of 3 – 5 mm), the surface structure is very fine. The thickness of printing structure (200 – 500 μm) is usually at the limit of current 3D printing capabilities and the properties of powder used for printing. Since the implant is loaded by the human body for a long time, it is necessary to verify the mechanical resistance of these small parts, where the disadvantage of printing can have fatal consequences.

This thesis deals with mechanical testing of samples produced by 3D printing. In clinical practice metallic material is primary used for implants, but they are costly to produce, and as this thesis is a pilot study, and will investigate polymer samples produced by 3D printing SLS technology. One of the main motivation for this thesis is to test fracture toughness, which is a key parameter for assessing the material resistance to accidental loading and crack propagation. A proper understanding of the methodology and assessment of fracture toughness of relatively inexpensive polymeric materials is the basis for future extension of the issue to metallic material, particularly titanium alloy. A focused look at metal 3D printing, particularly in the context of intraosseous implants, highlights the importance of this work to the field of medical research. The surface layers these implants, usually very thin and prone to fracture, present a technical call challenge that needs to be addressed though a though a thorough investigation of the mechanical properties of the material.

This thesis addresses not only to deep significance of fracture toughness methodologies, but also the design and optimization of methods and procedures for testing, evaluation and applying this knowledge to metal specimens. I believe that the results of this work will beneficial not only 3D printing technology, but also a wider range of industries including biomedical industry, where the metallic materials are key elements in the manufacturing process of innovation and reliable biomedical implants.

Motivation

In my master thesis, I deal in detail with the fracture mechanics of 3D printed samples. The main objectives include:

- possibilities of experimental analysis of fracture toughness on very thin samples;

- verification and selection of suitable samples that can be evaluated according to the relevant norm;

- design and use complementary experimental methods, such as DIC, for subsequent evaluation;

- development of a basic numerical model and comparison of calculation results with experimental results.

Previous experiment and literature researches show the uncertainty of the measured material parameters, especially that the conventional material model cannot be used for thin samples. My master thesis is to investigate the changes in the mechanical properties of thin samples and to find the limit where the shortcoming of 3D printing are no longer decisive.

The work was to investigate the mechanical properties of 3D printed titanium alloys of α and β crystal structures used in implantology. However, due to the very high financial costs (about 600,-/g per sample), my thesis finally deals with the investigation of samples based on polyamide material (PA12) produced by SLS 3D printing technology. Using this significantly cheaper material and its affordable production, samples from a thickness 500 μm can be produced, which will allow me to fine tune the design and procedure of the experiment. The main objective of my work is to design a fracture toughness experiment on thin polyamide samples, which includes selection of specimen geometry, the design of testing and subsequent evaluation of the results, the monitoring of crack, and then using this knowledge to continue the experiment on titanium alloy specimen in the future.

Chapter 1

Bioengineered materials and Technologies

1.1 Titanium and titanium alloys

The first mentions of titanium dates back to 1791, when R. W. Gregor found and unknown oxide in the iron sand on a sand beach, and this oxide was named "menaccanite". Four years later, the German chemist M. H. Klaproth found an identical oxide in Hungarian mountains and named it titanium, inspired from Greek mythology. Since this discovery, many chemists have tried extract titanium metal, but unsuccessfully. In 1910, M. A. Hunter reduced titanium tetrachloride $TiCl_4$ by sodium metal in closed steel container to obtain pure metallic titanium. Titanium metal was very brittle and could not be cold worked. Over the year, the production process has been refined to process very pure titanium. This process is called the "Hunter process" and it was used until the 1990s as the most common process for titanium production [1].

Another important metallurgist associated with the titanium production process is William Kroll. Kroll first used Hunter process to produce titanium, but in the 1930s he began working on developing a new process [2]. In 1940, he came with the reduction of titanium tetrachloride with magnesium metal. This process is called the "Kroll's process", which is still used for titanium production today [1]. The Kroll process is very expensive and energy intensive, but no one has been able to replace it to this day, and most of the world's titanium production is done using this process [2].

1.1.1 Kroll process

The Kroll process is divided into several production stages. The first process to be carried out is chlorination, in which titanium dioxide TiO_2 is chlorinated in the presence of carbon to produce titanium tetrachloride $TiCl_4$. The next step is the process of separation and reduction of $TiCl_4$ by magnesium metal, from which we

obtain the "titanium sponge" [1]. In the next step, the magnesium is injected into a reduction container filled with argon at temperature of 800 – 1000 °C. In this case, argon is used to prevent oxagen and nitrogen contamination of the titanium sponge. The magnesium reacts with $TiCl_4$ to form liquid magnesium chloride $MgCl_2$ and a hard porous titanium sponge [3]. The final step is electrolysis, in which $MgCl_2$ is separated by a reduction and separate process and than separated into Cl_2 gas and magnesium by electrolisys. Figure 1.1 shown a schematic representation of titanium production in a steel reduce container. After vacuum distillation, an extended cooling process occurs. The titanium sponge is mechanically separated using a die cutter and pulverized into small pieces. After quality control, the titanium sponge starts to melt for the production of titanium ingots. The process of obtaining metallic titanium is demanding for continuous production, so today a batch process is used for the reduction, distillation, cooling and recovery of titanium [1].
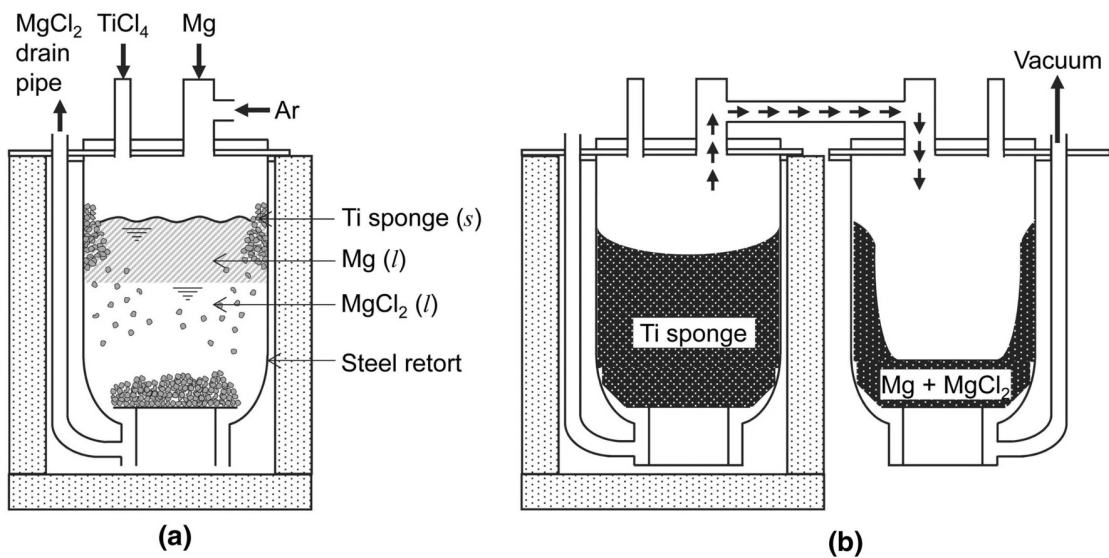
Figure 1.1: Procedure for the production of titanium sponge according to Kroll's process a) Magnesiothermic reduction of $TiCl_4$, b) removal a magnesium and $MgCl_2$ by vacuum distillation [1].

1.1.2 Titanium alloys

Titanium is an allotropic element, meaning that it can occur in two or more different crystal structure [4]. Allotropy is a property of a material that can occurs in a several different structures with different properties. These properties differ in their crystal lattice, the number of atoms in the molecule and physical or mechanical properties. In titanium alloys allotropic transformation is crucial for the monitoring microstructure and property of alloys and depends on the alloying elements added into pure titanium [5].

A pure titanium has a hexagon close packed structure (HCP) at low temperature, also called α titanium, which gives the alloy greater strength, high fracture toughness and low forgeability. While titanium at high temperature has a body centered cube (BCC) structure, also called β titanium, which makes the metal more ductile. The temperature for conversion HCP to BCC is 882 °C and is called beta transus

temperature and depend on the amount of incorporated impurities. The structures of HCP and BCC are shown in Figure 1.2 [4, 6, 7].
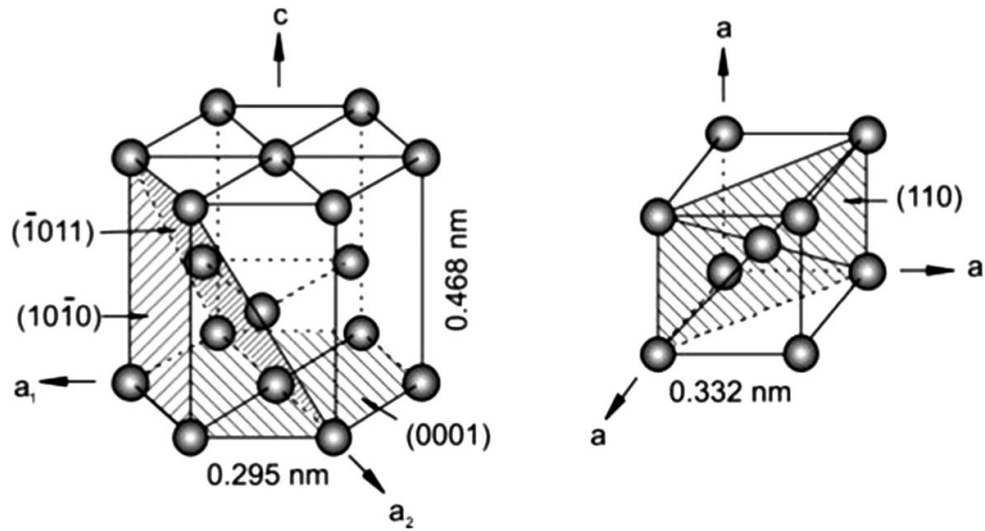
Figure 1.2: Phases of titanium: α phase (left), β phase (right) [8].

Titanium alloys are divided into 5 categories according to structural their properties and the elements present in them. These categories include α alloys, near α alloys, α/β alloys, metastable β alloys and stable β alloys. In production alloys, each added elements to pure titanium affect mechanical properties, because it affect stability between the α and β phases. The stabilizing temperature can be changed by alloying agents, which can change the ratio between α stabilization elements and β stabilization elements. The α stabilization elements include aluminum (Al), gallium (Ga), oxygen (O), nitrogen (N), carbon (C) and the β stabilization elements include vanadium (V), molybdenum (Mo), niobium (Nb), iron (Fe), chrome (Cr), nickel (Ni) [4, 7].

1.1.3 Biomedical titanium alloys

Titanium has been used in medical, surgical and dental devices since World-War II, due to increased demands of the aerospace and military industries, which also use the material extensively. Over time, titanium alloys began to be used as a biomaterial, due to their elasticity, excellent biocompatibility and better corrosion resistance that stainless iron and cobalt-based alloys. These properties were main reason for develop Ti-based alloys in medicine [9].

In biomedicine, titanium alloys are mainly divided according to their biomedical functions. The first major branch is hard tissue replacement, which are mostly caused by accidents, aging and others. Titanium alloys are widely used for replacing the damaged hard tissues with artificial replacement such as bones, joints and dental implants. The low elastic modulus of titanium alloys is considered to be biomedicinal advantage as it leads to less stress shielding. One of the most common application in hard tissue replacement is artificial hip joint or knee joint replacements, both shown in Figure 1.3. Other applications of titanium alloys in biomedicine are in dental

industry, cardiac and cardiovascular problems and in the fixation of bone fracture [9].
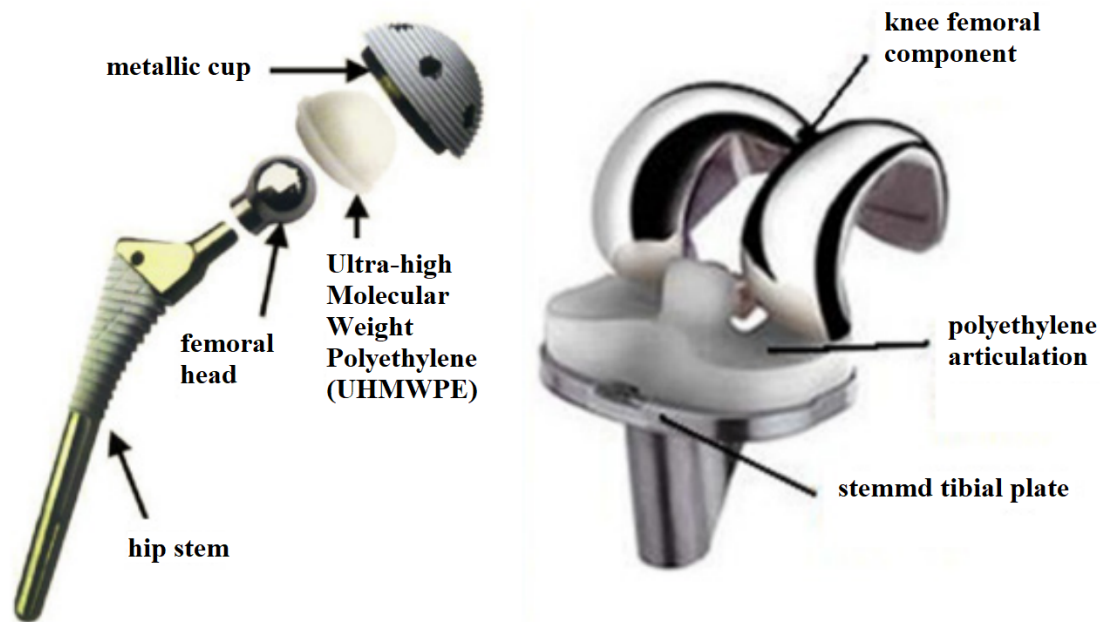
Figure 1.3: Examples of titanium alloys implant: artificial hip joint (left) and knee joint replacement (right) [10].

Currently, the most commonly used alloy for orthopedic and medical application is Ti_6Al_4V, which is $\alpha + \beta$ alloy. The main reasons for its use are good mechanical properties, corrosion resistance in biofluids, biocompatibility and heat treatability. However, the problem arises with wear resistance, even in soft tissue friction. Furthermore, this alloy is quite toxic to the human body, because harmful tissue reactions occur due to release of vanadium ions, which is toxic and carcinogenic element. Aluminium ions in high concentration can cause long-term health disorders such as Alzheimer's and Parkinson's diseases, dementia, adverse tissue and others [11]. Another problem with this implant material is its elasticity modulus, which reaches values of up to 110 GPa, while human cortical bone reaches values of 30 GPa. These differences in values between the implant and human bone lead to stress-shielding effect, which causes a bone adsorption and its potential hazard for patients [12].

Nowadays, β alloys are the most studied alloy that could potentially replace Ti_6Al_4V, due to their strength and good fatigue resistance. It has also been shown that β alloys are more suitable for human bones than α or $\alpha + \beta$ alloys [12]. Orthopedic implants should be able to withstand the cyclic loading caused by body move. These loading causes a concentration of micro-stress, leading to nicks or inhomogeneous microstructure. The ideal implants material should have low elastic modulus, good plasticity and wear resistance in addition to high strength and fatigue resistance [13]. To obtain these material properties, the alloying elements are the most important in β alloys [12].

1.2 Nylon - Polyamide material

Nylons are an important part of thermoplastic polymer family and have many different subtypes (Nylon 6, Nylon 66, Nylon 12 and others). Due to their repeating units linked by amide bonds, nylons are also known as polyamides (PA) [14]. PAs occur naturally in wool or silk, synthetic PAs is usually produced by condensation polymerization and are knows as Perlon, Kevlar and Nomex. Aliphatic PAs, polyphtalamides and aromatic PAs are three main synthetic types of PA. The main mechanical properties of nylons are tough, high tensile strength and elasticity. Other properties of nylon are resistance to abrasion and chemicals such as acids and alkalis or good oil resistance, which is caused to the amide groups in the molecular and the hydrogen bonds between the adjacent molecular chains [15].

In my experiment I investigated polyamide powder material PA12 processed by SLS 3D printing technology, so in this section I will only focus on this material. Nylon 12 has a longer aliphatic chains that the other polyamides, which causes lower mechanical strength and melting temperature. In contrast, nylon 12 exhibits high pressure resistance, impact resistance flexibility, low density and good mechanical resistance [15].

PA12 crystal form contain two main types of polyamide crystal forms, which are known as α and γ. These crystal have subforms known as α', α'' and γ' [16]. Figure 1.4 shown a hydrogen bounds surface of α and γ crystal form. The antiparallel arrangement of the chains is the definition of α-crystal form, where it is easy to achieve a hydrogen bonded surfaces between the extended chains. The γ-crystal form is arranged in parallel and the hydrogen bonded surfaces demand some chain entanglements. The hydrogen bonds are formed between adjacent amide groups of the molecular chain so that hydrogen bonds can be maximized to meet the requirements of the molecule chain arrangement. The hydrogen bonds formed must be arranged linearly [17].
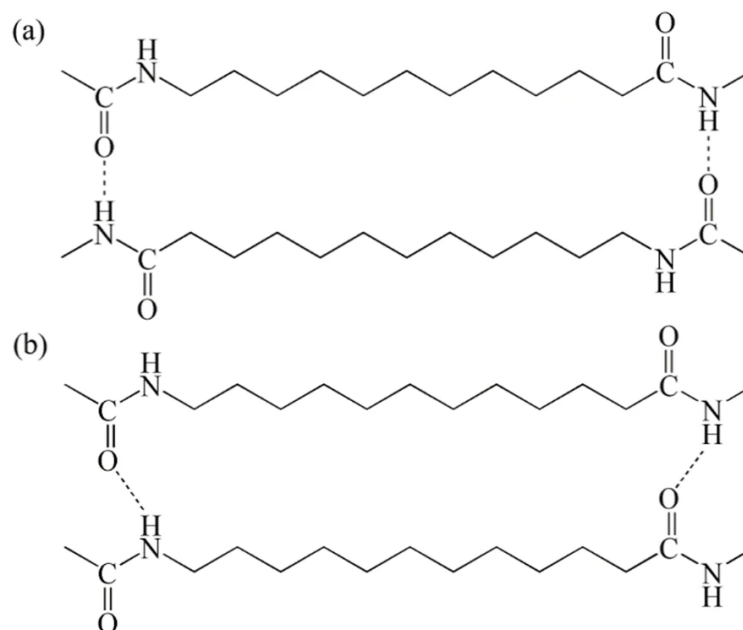
Figure 1.4: Hydrogen bonding surface of nylon 12 crystal forms a) α form b) γ from [17].

The differ between the crystal structure is a way how can be nylon obtained. High preassure or drawing is specifical conditions to obtain a α-crystal form. Also can be taken by cooling the melt or by annealing the γ'-crystal form at high pressure above 500 MPa. The γ-crystal form can be obtain by slowly cooling from the melt or annealing the α or γ' crystal form by a temperature. The γ'-crystal form is very similar to γ-crystal form and can be obtain by quenching from the melt or drawing the α or γ crystal form at low temperature [18].

1.2.1 Biomedical application

Nylon composites have been widely investigated in recent years as a potential replacement for metal implants. In medicine, they are found in the form of sutures, catheters and dental implants [19]. The advantages of nylon composites is their biocompatibility, chemical stability, tunable mechanical qualities and the possibility of manufacture by 3D printing technology, which is a way to make more complex shapes and structures [20]. The reason for biocompatible properties are amide groups in nylon structure, as the amide groups have a similar chemical structure to natural peptides. This means that the immune system protecting the human body can easily accept them [15].

Nylon skin sutures are made up of thin nylon fibers twined together and they are used for their high level of strength, low thickness and flexibility. A natural polymer may be added to the surface of nylon sutures to boost their antibacterial ability due to their properties to protect and close wound. Nylon sutures are non-absorbe sutures, which means that they must be removed after the wound has healed and can remain in the human body for a maximum of 21 day [15, 20].

Another application is catheters, especially cardiac catheters, because there it is possible to create narrow tubes with acceptable dimensional tolerances. During a heartbeat, there is a cyclic compressive load that nylon catheters can withstand due to their elasticity. Nylon polymer can also be create catheters balloons that can help expand and release blockages in blood vessels, improve drug delivery and expand stents for cardiovascular disorders [15, 20].

Nylon is used in dental implants as part of dentures. It is primarily usage is to secure gum and artificial teeth to denture, which provide greater comfort to users due to its flexibility. The lifespan of the implants is estimated to be 5 years or more. The problem arises when bone loss near the implant, leading to fracture of the prosthesis. This relates to the length of the cantilever, which must be less than 20 mm, but the best results implant were achieved when the length was around 15 mm. Nylon mesh is used to increase strength and distribute stress [15].

1.3 3D printing technology

There are many types of additive manufacturing techniques for medical and tissue engineering purpose. Nowadays, the technologies are at such a high level that we are able to print living cells, also known as bioprinting [21]. However, my thesis is mainly concerned with titanium alloys and polymer materials for implants, so I will only discuss the technologies for manufacturing these materials here.

Technology of 3D printing is an additive manufacture used mainly in biomaterials due to the ability to produce a wide range of structures and complex geometries from 3D models. The process consist of printing successive layers of materials that are stacked on top of each other. In 1986, Charles Hull developed the first known 3D printing technology and called it stereolithography (SLA). This technology was followed by the development of technologies such as powder bed fusion, fused deposition modelling (FDM), inkjet printing, contour crafting (CC), and these technologies are shown in the Figure 1.5 [22, 23]. Powder bed fusion was used to produce the samples for my experiments, so I will discuss this technology in detail in the Section 1.3.1.
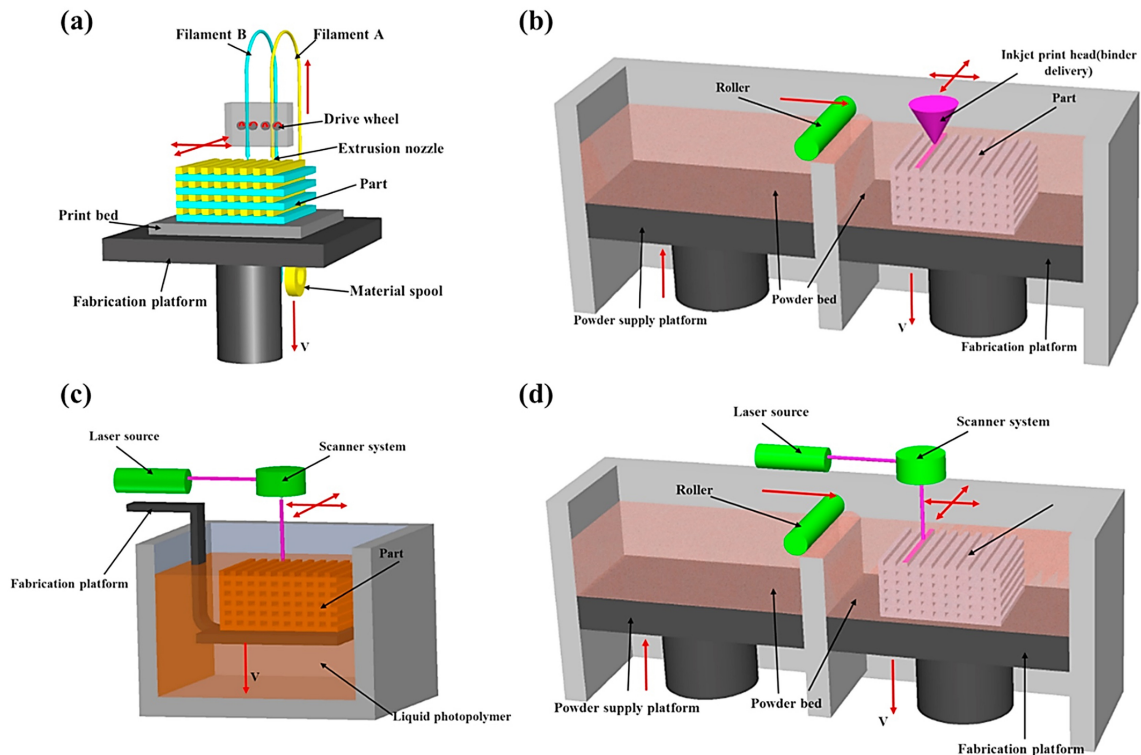
Figure 1.5: Diagram of the four main additive manufacture technologies: a) fused deposit modellinf (FMD), b) inkjet printing, c) stereolithography (SLA), d) power bed fusion (PBF) [24].

1.3.1 Power bed fusion

The development of modern power bed fusion technology was investigated to C. Deckard in the 1980s and commercialized as selective laser sintering (SLS) [25]. In

biomaterials, it is the most common technology for manufacturing metallic parts. In PBF technology, an energy source is used to selectively bond or melt powder particles layers by layers, to subsequently create the desired geometry. There are many heat sources such as pulsed laser, electron beam or ultraviolet light. Metals require high temperature for melting and therefore need high energy density for particles consolidation. In that fact, laser and electron beam are the most used types of heat sources for metal fabrication [26].

Generally, PBF can be divide into 3 steps: powder recoating, energy input and cooling. The powder recoating process consists of the movement of a roller (recoater) that spreads a fresh layer of powder to the fabrication piston. The energy input causes the transfer of heat from the machine to the powder particles. This is usually a combination of heat energy input from room temperature to an elevated isothermal processing temperature (the bed temperature) and energy input from infrared sources. In laser sintering (LS), the infrared source is the laser beam, while in other types such as high speed sintering (HSS) and multi jet fusion (MJF), the infrared lamps are the sources. The final step, cooling, causes solidification through heat loss, where printed layer drops to bed temperature and than the temperature drops to room temperature. Figure 1.5 shows a close-up view of selective laser sintering(SLS) process [27].
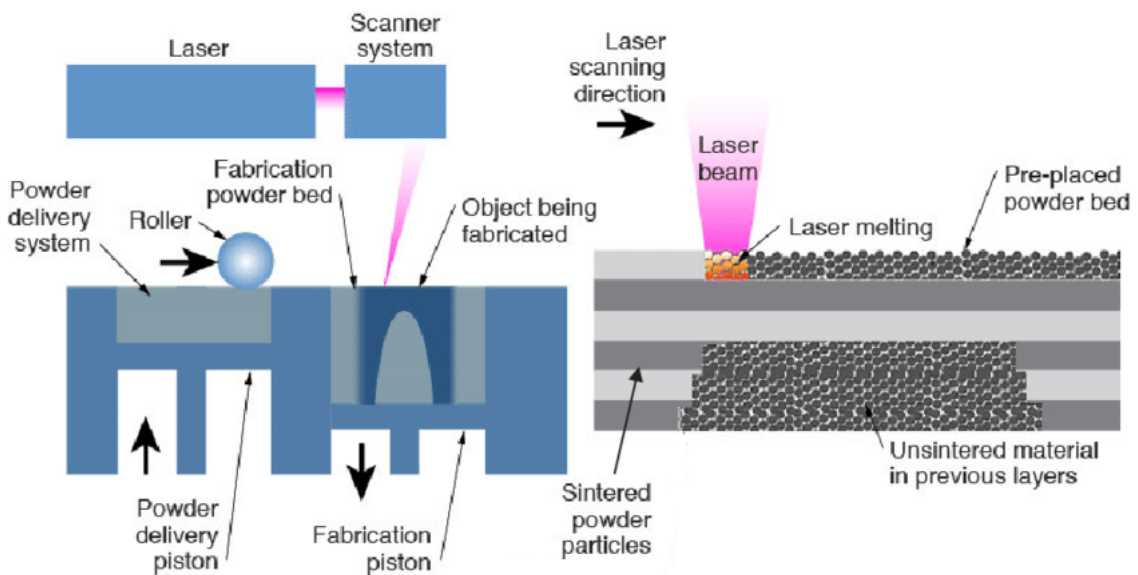
Figure 1.6: Schematic of power bed fusion printing technology [28].

1.3.2 Weaknesses in technology

Powder 3D printing technologies (SLM, SLS, EBM) are a great tool for create complex shapes and structures, as shown in the Figure 1.7. These formations can have different spatial arrangement in terms of the aesthetics or mechanical load capacity, depending on the efficiency of the environment they are intended for. By narrowing to 3D technologies applicable in bioimplantology, the focus narrows to applications primarily in the form of intraosseous replacements (typically titanium alloys) or external fixation sleeves.

Figure 1.7: Demonstration of the application of 3D printing in medicine. 3D printed acetabular component of a trabecular titanium alloy hip implant – Lima® (left) and 3D printed polymer fixation orthosis as a replacement (right) [29].

When focus on the intraosseous parts of implants and the production of the applications by 3D printing, it is necessary to taken into account the requirement for quality osseointegration, in which the implant is stabilized in the bone. With 3D printing is possible to create a special porous layer consisting of beam or wall system, which helps the bone cells to grow into the implant [30]. The porous structure thus created must be optimized in terms of mechanical load capacity, but the pore size must still be taken into account, which according to the literature studied should be in range of $200 – 800$ μm [31, 32, 33].

In fact that diameter of dental implants usually ranged between $3.0 – 5.5$ mm is evident that porous layer must be very thin. The lack of space for surface treatment and the desire to reduce global modulus of elasticity of the porous layer to the level of the bone tissue so as to avoid an effect called stress shielding means the need to create very thin beams or walls of the final structure [34]. This pushes the manufacturing process to its technological limits and results in frequent defects already at the manufacturing stage. Any defect in an implant that is intended to work in the human body for a long time is very dangerous, as it can cause necrosis and ultimately cause it to come loose.

Basic mechanical tests carried out within the framework of the TAČR project [35] showed problems with the fine beam structure. Discontinuities and inconsistent beam thicknesses were found in fabrication of optimized trabecular structures for surface use on dental and hip implants with each beam thickness of approximately $150 – 350$ μm. Figure 1.8 shows the discontinuities and inconsistent beam thicknesses of each beams.
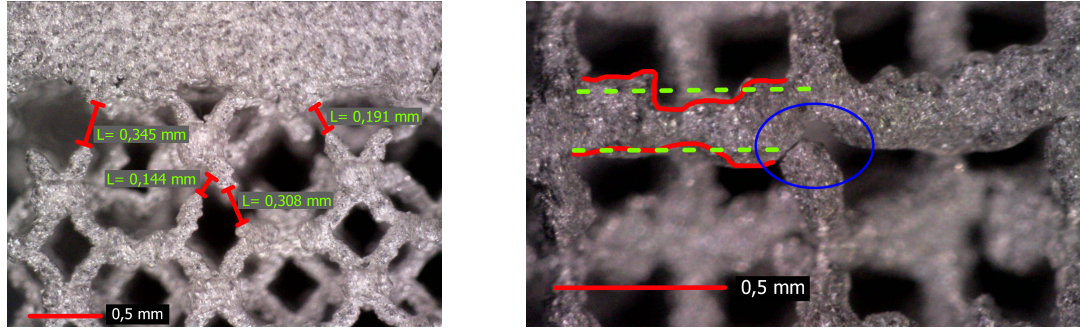
Figure 1.8: Discontinuities of individual beams of the trabecular structure shown by optical microscope (left) and inconsistent trabecular width (right) [35].

The beam structure concept has ceased to be an option for osseointegration surface and has been replaced by a more reliable wall system. This system of gyroid structures is less susceptible to local defects while retaining the ability to define exact porosity and pore size [30]. Gyroid is continuous structure with 3 more periodic morphology, constant curvature and interconnected and open pores [36]. This arrangement depends on the boundary curvature parameter, which makes it possible to define the structure as wall or beam and at the same time to influence its porosity [37]. Unfortunately, even when the gyroid wall structure is applied the wall thickness is in the range of $150 - 350$ μm, which is at the limit of the printability of current 3D printers.

Experiment studies bending and simple tension testing of very thin specimens have shown that it is not possible to use the manufacturer guaranteed mechanical parameters for thin specimens, for example for numerical calculations [38]. The load-deflection graphs in Figure 1.9 show another negative for thin samples. These is the large number of inadequately welded powder beads into the main body that can be chemically etched from the sample surface. The removed powder beads subsequently weaken the specimen, resulting in a decrease in load carrying capacity and basis mechanical properties such as modulus of elasticity. However, as can be seen in the graphs above, as the thickness of the sample increases, the effect of post-etching disappears and the samples subsequently achieve the expected mechanical properties.

Thus, one significant 3D printing error that is apparent in thin samples is insufficiently welded powder beads, and the other error is inconsistent sample width. Considering that the powder fraction of Ti_6Al_4V material is usually in the rage of $30 - 70$ μ, the roughened surface will have a significant effect on its material parameters in thin samples. Within the framework of the GAČR project No. 23-04971S, the researches are working on the analysis of thin samples and the correlation of experiments with numerical calculation. According to the preliminary results, the Table 1.1 shows a significant difference between the measured elastic modulus (E_r) and the elastic modulus determined by theoretical calculation, in which the actual values of displacement and force from experiments are input, but the theoretical dimensions of the specimen as the model was created for 3D printing.
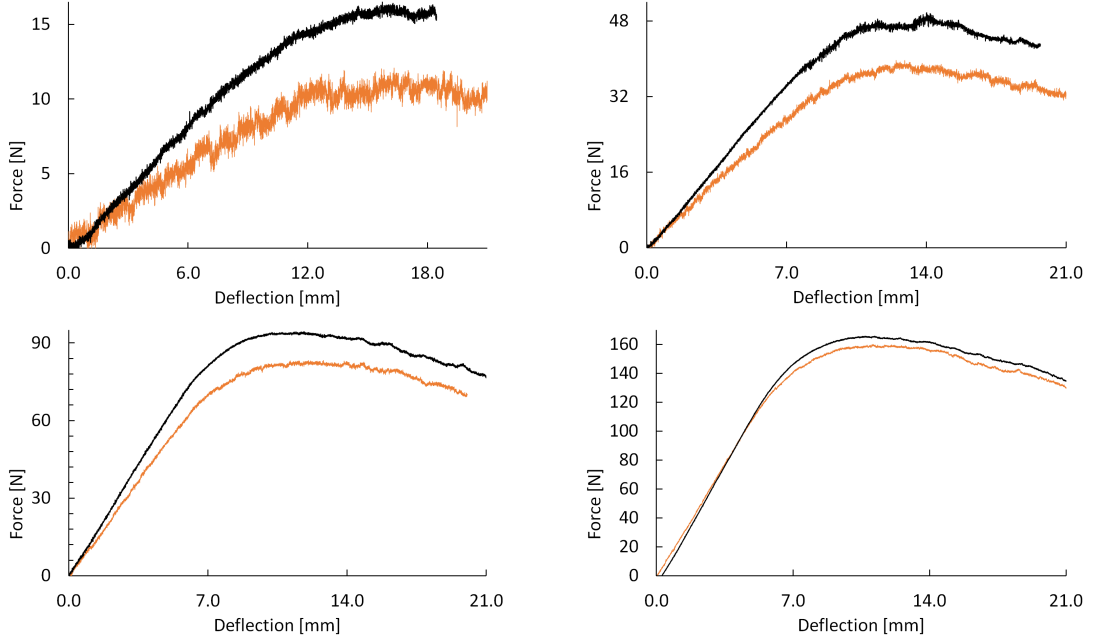
Figure 1.9: Dependence of deflection on load force in a simple bending test. The specimens differed in width which was 500, 750, 1000 and 1250 μm. Black line are specimens without surface etching, orange line are specimens with surface etching [38].

plate dim.	500 μm	750 μm	1000 μm	1250 μm
modulus	without chemical etching			
E_r [GPa]	65 ± 7	92 ± 6	111 ± 4	116 ± 4
E_t [GPa]	118 ± 9	119 ± 7	119 ± 5	118 ± 4

Table 1.1: Overview of recalculated values of global elastic moduli, where E_t is calculated from theoretical dimensions (geometry before printing) and E_r is calculated from real dimensions adjusted for 3D printing-related imperfections [38].

Thus, powder 3D printing technology has significant shortcoming in its application to very thin samples. Therefore, in order to use it in bioapplications and implantology, it is necessary to be able determine the degree of inaccuracy and deviation of actual properties from theoretical ones. It will then be possible to replace very expensive experimental testing with numerical simulations. However, this requires the development of a high quality material model that can cover these shortcomings.

Chapter 2

Fracture mechanics

Fracture mechanic is the study of engineering mechanical where the resistance of a material to crack propagation is measured and is called fracture toughness. Fracture toughness values can serve as one the main material properties and quality for typical engineering structure [39]. Fracturing of material is cased by the finite strength of atomic bonds. When a material begins to fail, cracks are responsible for amplifying local stress states that lead to fracture [40].

In fracture mechanics studies, two main parameters called fracture energy G and stress intensity factor K are often determined and presented [41]. The fracture energy is defined as the amount of energy needed to create one unit of area of a continuous crack and is the fundamental quantity that governs crack propagation [42]. While stress intensity factor is based on three different modes (mode I, mode II, mode II) and can specify the mechanical behaviour of material with crack [43].

2.1   Introduction to fracture mechanics

The first references to fracture toughness were discover in 1838 in Albert's work, which investigated the collapse of a mine chain under cyclic load. Porcelet called this process "fatigue" in his book published in 1839. The first study about fatigue were carried out by Wöhler, where he observed the collapse of the rails after many "cycle" applied by the train. Over time, it has become clean that predicting fracture initiation of structure is very important. There was an idea that the ability to absorb energy is the main property that prevents the formation of a crack. Because of this idea, deformations of materials without breaking them began to observe [44].

Another contribution to the study of fatigue was made by Considère, who proved by calculation that in a material governed by a simple power law hardening, the onset of plastic instability occurs when the actual strain equals to the power law exponent. Because of this calculation, the collapse of structure could be predicted and a selected suitable material for the structure. Based on Considère's calculation Charpy developed new method in 1901, which is now known as the Charpy V-notch impact test. This method has a great influence on a fracture control and is still used

for selection of structure materials [44].

Initial work on elastic crack problems is attributed to Inglis, who was inspirated by previous work by Weighart and Kolosov. Inglis solve the maximum tensile stress on an elliptical hole in a two-dimensional infinite sheet under uniaxial tension. Figure 2.1 shown elliptical hole and an example where is radius $r = 0$ means that the ellipse becomes a mode I crack [45].
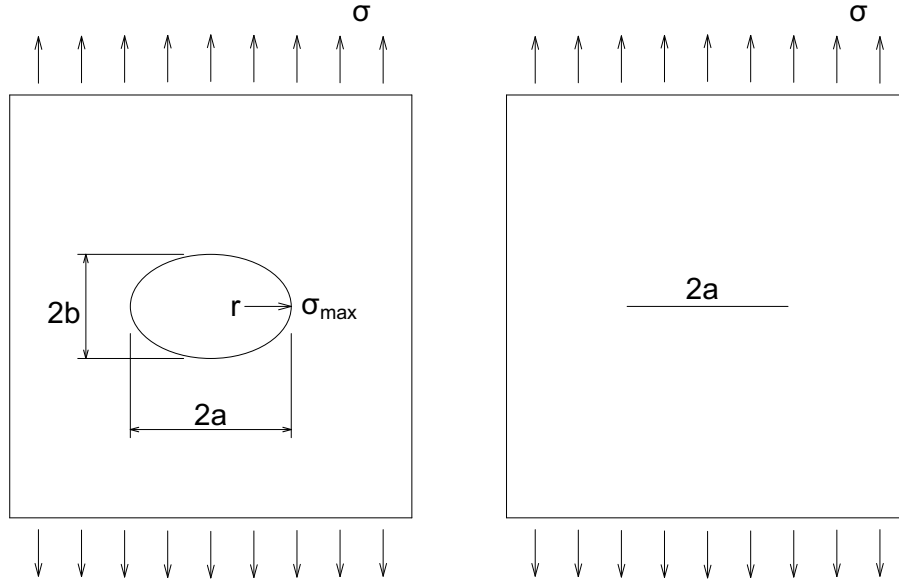
Figure 2.1: Elliptical hole in a two dimensional infinite sheet under uniaxial tension [45].

The equation for the maximum tensile stress is based on the surface of elliptical hole. The major and minor axes of the elliptical are denoted as a and b [46].

$$\left(\frac{x^2}{a^2}\right) + \left(\frac{y^2}{b^2}\right) = 1 \tag{2.1}$$

The radius of curvature at $x = \pm a$ and $y = 0$ is denoted as r which can be related to a and b as is shown in 2.2 [46].

$$r = \left(\frac{b^2}{a}\right) \tag{2.2}$$

Based on the previous equations, Inglis could find that the maximum tensile stress at the ends of major axis of the ellipse and this is described in the Eq. 2.3 [45].

$$\sigma_{max} = \sigma\left(1 + \frac{2a}{b}\right) = \sigma\left(1 + 2\sqrt{\frac{a}{r}}\right) \tag{2.3}$$

The Inglis calculation represent the problem shown in the figure 2.1 on the right. In the limit of a perfectly sharp crack, the stress at the crack tip approaches infinity, and

this is clearly nonphysical because material generally undergoes some local yielding to blunt the crack tip. Based on Inglish's calculation, Griffith focused on the energy balance of the material instead of maximal stresses at the crack tip [47].

2.2   Fracture energy

Based on linear-elastic fracture mechanics (LEFM), Griffith presented his theory of energy criterion for the fracture propagation of cracks in solids. He investigated glass specimens and developed an association between the size of crack and the fracture stress. According to this theory, a crack will propagated in a material if the elastic strain energy is greater than or equal to the energy required to form the crack surface [48]. In his view, the weakening of material by crack is real problem in which the strain energy is reduction, when the crack propagates, and this leads to an increase in surface energy due to an increase in surface area [49].

Imagine a large or infinity brittle plate containing single central crack of length 2a with two crack tips, as is shown on Figure 2.2. When is plate loaded by uniform tensile along the x-axis, the stored elastic strain energy is realised in a cylindrical volume of material of length B [50].
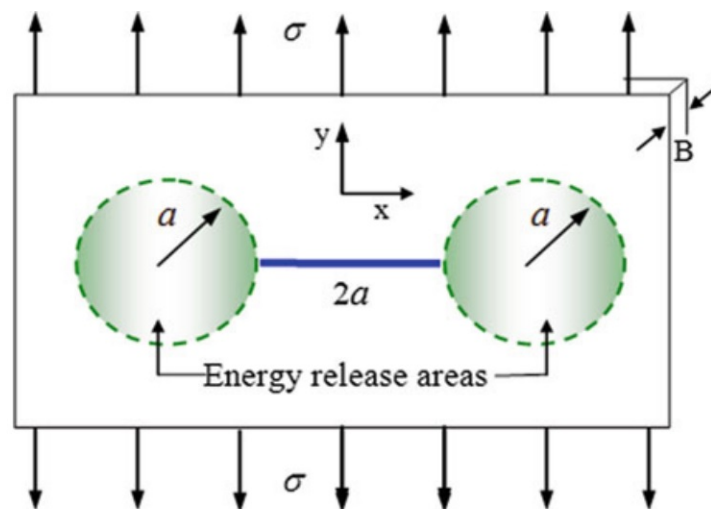
Figure 2.2: Large or infinity brittle with containing single central crack and two idealized energy release areas [50].

To increase a crack size, potential energy must be available in the plate to overcome the surface energy of material. The Griffith energy balance for the increment increase in the crack area is described by equilibrium conditions in Eq. 2.4 [51].

$$-\frac{D\Pi}{dA} = \frac{dW_s}{dA}$$ (2.4)

where Π is the potential energy supplied by the internal strain energy and external forces and W_s is the work required to create new surface [51]. When an elastic or brittle solid body is loaded from the crack faces, the product of the released elastic strain energy density and cylindrical volume element, where this energy is released, yields the elastic strain energy as:

$$W_e = -(2\pi a^2 B) \int \sigma \, d\epsilon = -(2\pi a^2 B) \int E' \epsilon \, d\epsilon$$

$$W_e = -(2\pi a^2 B) \frac{E' \epsilon^2}{2} = -(\pi a^2 B) \frac{\sigma^2}{E'}$$

(2.5)

where $E' = E/(1-\nu^2)$ is condition for plane-stress, ν is Poisson's ratio, E is Modulus of elasticity, ϵ is elastic strain, σ is applied remote stress, a is one-half crack length and B is thickness [50]. Than Griffith use the elastic stress analyses of Inglis to show that:

$$\Pi = \Pi_0 - (\pi a^2 B) \frac{\sigma^2}{E'}$$

(2.6)

where Π_0 is the potential energy of an uncracked plate. The crack requires the creation of two surface energy:

$$W_s = 2(2aB\gamma_s)$$

(2.7)

where γ_s is specific surface energy for atomic bond breakage [51].

For and elastically stressed solid body, potential energy in the Griffith energy balance decrease and the surface energy increase because of the growing crack, which creates new surface. This potential energy can be expressed as:

$$W = W_s + W_e = 2(2aB\gamma_s) - (\pi a^2 B) \frac{\sigma^2}{E'}$$

(2.8)

The total potential energy per unit thickness is obtained by dividing Eq. 2.8 by the thickness B as:

$$U = U_s + U_e = 2(2a\gamma_s) - \frac{\pi a^2 \sigma^2}{E'}$$

(2.9)

where U_s is elastic surface energy per unit thickness and U_e is released elastic energy per unit thickness. Griffith's energy criterion for crack growth is $U_e > U_s$ when $\frac{dU}{da} = 0$. Under these conditions it is possible to express the energy needed for crack growth as:

$$G_c = \frac{\sigma^2 a \pi}{E'}$$

(2.10)

The stress in Eq. 2.11 is predicted fracture stress σ_f, thus:

$$\sigma_f = \sqrt{\frac{G_c E'}{\pi a}} = \frac{K_c}{\sqrt{\pi a}} \tag{2.11}$$

where K_c is called stress intensity factor which is the critical value of material also known as fracture toughness [50, 52].

The Griffith energy criterion is focused on brittle materials. He described that the properties of the end-region are influenced by the energy-absorbing capacity. Irwin and Orowan expanded this theory for non-brittle material (especially for metals) [53]. When a crack propagates in the presence of plastic deformation at the crack-tip, a certain amount of energy is expended to create a new surface beyond the elastic energy. Assuming that a plastic zone does not change with size crack, plastically deformed material lies adjacent to the edges of crack as shown in Figure 2.3 [54].
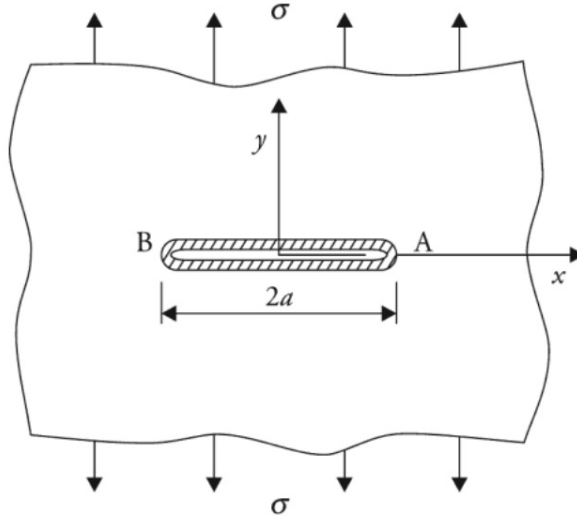
Figure 2.3: Plastic zone of deformed material adjoining crack edges [54].

The size of the plastic zone at the crack-tip is so low compared to size of the crack or thickness of the specimen that the global elastic strain energy can by calculated using elasticity methods. The energy balance of the unstable extension can be given by the relation:

$$\frac{\Delta W_e}{2\Delta a} \geq \frac{\Delta W_s}{2\Delta a} + 2\gamma_p \tag{2.12}$$

or

$$\frac{\sigma^2 \pi a}{E} \geq 2\gamma_s + 2\gamma_p \tag{2.13}$$

where γ_s is surface energy and γ_p is the energy per unit for plastic deformation. In that case of $\gamma_p >> \gamma_s$ with a small-scale yielding at the crack-tip, σ_f can be

described as:

$$\sigma_f = \sqrt{\frac{2E\gamma_p}{\pi a}} \tag{2.14}$$

This can be used to determine the load that a given structure will sustain if the size of the defect is known or to determine the tolerable defects at a given load. This can be taken as a basis for design against damage [54, 55].

2.3   Stress intensity factor

For a crack, there are three independent moments for the top and bottom crack surface. These moments are divided into three basic modes shown on Figure 2.4, which shows the displacement of the crack [56].
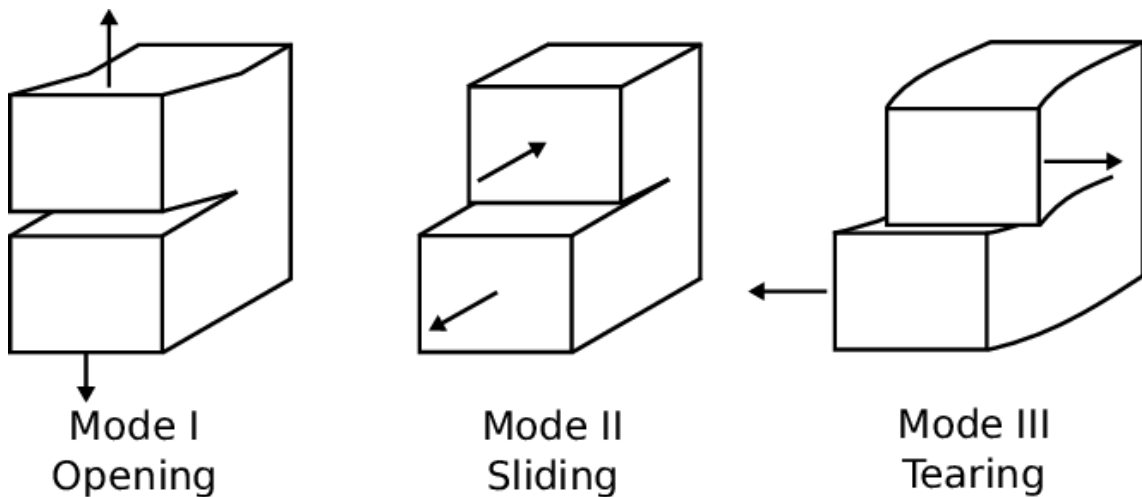
Figure 2.4: Modes of crack deformation [57].

Mode I represents opening of the crack by tensile loading and the crack surface is symmetrically separated. In Mode II, the crack surface slide symmetrically and is loaded by shear. Mode III is also loaded by shear and the crack surface is displaced in different directions relative to each other [56].

Westergaard came up with a theory for solving a certain class of plane elasticity problem using the invented Airy stress function. He solving the problem on an infinity plate, where he established boundary conditions for the uniform stress σ, shear stress τ and out of plate shear stress τ. Infinity plate contains a crack length $2a$ which occupies the segment $-a \leq x \leq a$ along the x-axis shown in Figure 2.5.

Westergaard's function for these three type of stresses defined as:

$$Z_I = \frac{\sigma z^2}{\sqrt{z^2 - a^2}} \qquad Z_{II} = -\frac{i\tau z}{\sqrt{z^2 - a^2}} \qquad Z'_{III} = \frac{\tau z}{\sqrt{z^2 - a^2}} \tag{2.15}$$

where z is a complex variable, a is half of crack length and σ, τ are type of stresses [56].
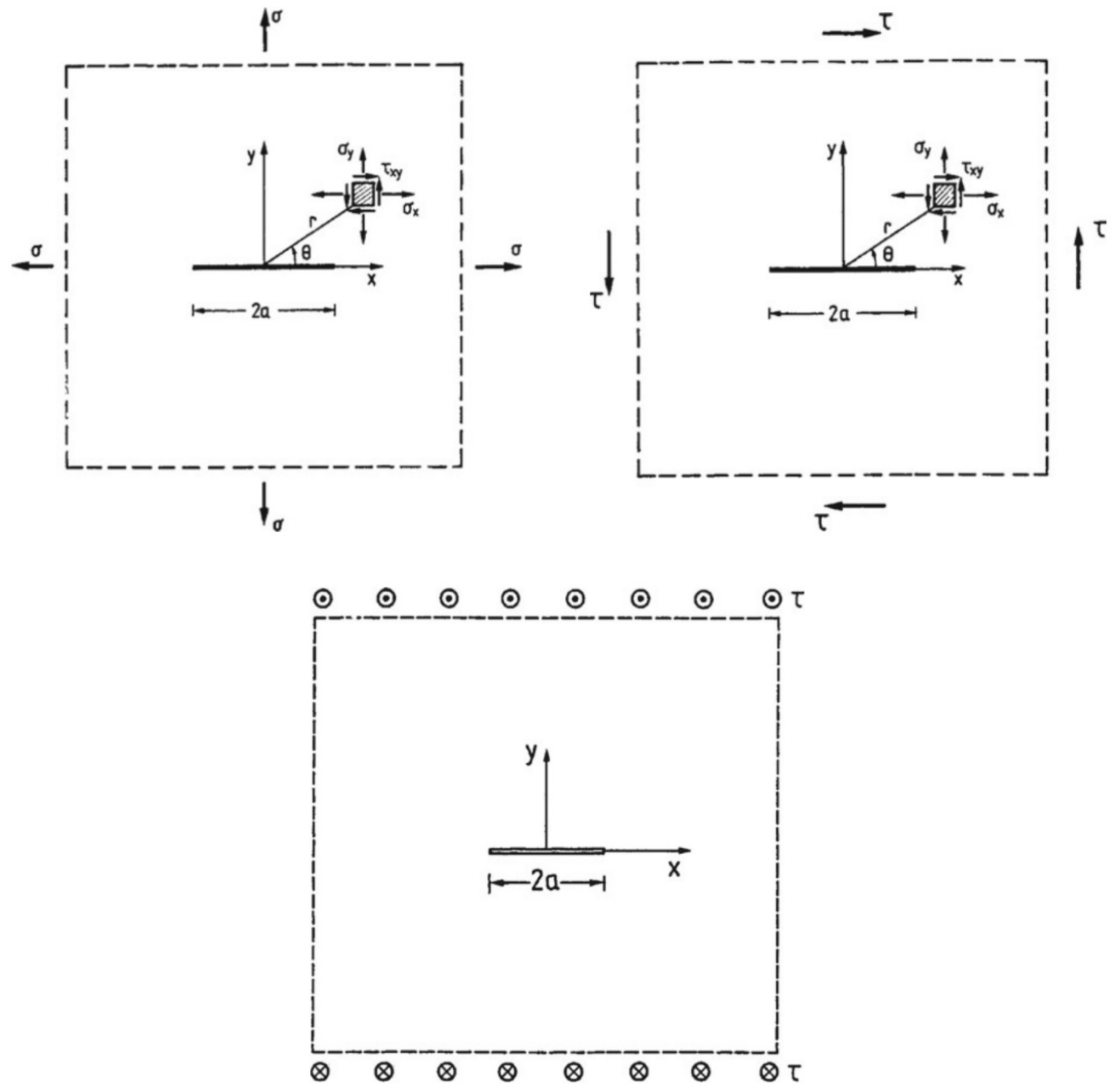
Figure 2.5: An infinity plate with crack of length $2a$ loaded by uniform and shear stress. [56].

Irwin expressed the stresses near the crack tip according to the analytical function Eq. 2.15, where the origin of the coordinate system is located at the crack tip ($z = a$) and built an equation for the stress and displacement for all modes [56].

For pure opening mode (Mode I) he described stresses as:

$$\sigma_x = \frac{K_I}{\sqrt{2\pi r}} \cos\left(\frac{\theta}{2}\right) \left[1 - \sin\left(\frac{\theta}{2}\right) \sin\left(\frac{3\theta}{2}\right)\right] \tag{2.16}$$

$$\sigma_y = \sigma_y = \frac{K_I}{\sqrt{2\pi r}} \cos\left(\frac{\theta}{2}\right) \left[1 + \sin\left(\frac{\theta}{2}\right) \sin\left(\frac{3\theta}{2}\right)\right] \tag{2.17}$$

$$\tau_{xy} = \frac{K_I}{\sqrt{2\pi r}} \cos\left(\frac{\theta}{2}\right) \sin\left(\frac{\theta}{2}\right) \cos\left(\frac{3\theta}{2}\right) \tag{2.18}$$

and the near crack-tip displacement field as:

$$u = \frac{K_I}{\sqrt{2\mu}} \sqrt{\frac{r}{2\pi}} \cos\left(\frac{\theta}{2}\right) \left[\kappa - 1 + 2\sin^2\left(\frac{\theta}{2}\right)\right] \tag{2.19}$$

$$v = \frac{K_I}{\sqrt{2\mu}} \sqrt{\frac{r}{2\pi}} \sin\left(\frac{\theta}{2}\right) \left[\kappa + 1 - 2\cos^2\left(\frac{\theta}{2}\right)\right] \tag{2.20}$$

In the same way he express stresses for plane sliding mode (Mode II) as:

$$\sigma_x = -\frac{K_{II}}{\sqrt{2\pi r}} \sin\left(\frac{\theta}{2}\right) \left[2 + \cos\left(\frac{\theta}{2}\right) \cos\left(\frac{3\theta}{2}\right)\right] \tag{2.21}$$

$$\sigma_y = \frac{K_{II}}{\sqrt{2\pi r}} \left[1 - \sin\left(\frac{\theta}{2}\right) \sin\left(\frac{3\theta}{2}\right)\right] \tag{2.22}$$

$$\tau_{xy} = \frac{K_{II}}{\sqrt{2\pi r}} \cos\left(\frac{\theta}{2}\right) \sin\left(\frac{\theta}{2}\right) \cos\left(\frac{3\theta}{2}\right) \tag{2.23}$$

and

$$u = \frac{K_{II}}{\sqrt{2\mu}} \sqrt{\frac{r}{2\pi}} \sin\left(\frac{\theta}{2}\right) \left[\kappa + 1 + 2\cos^2\left(\frac{\theta}{2}\right)\right] \tag{2.24}$$

$$v = \frac{K_{II}}{\sqrt{2\mu}} \sqrt{\frac{r}{2\pi}} \cos\left(\frac{\theta}{2}\right) \left[\kappa - 1 - 2\sin^2\left(\frac{\theta}{2}\right)\right] \tag{2.25}$$

where $K_I = \sigma_{yy}\sqrt{\pi a}$ and $K_{II} = \tau_{yx}\sqrt{\pi a}$ are stress intensity factors for Mode I and Mode II, $\kappa = 3 - 4\nu$ for plane strain and $\kappa = (3 - \nu)/(1 + \nu)$ for plane stress, μ is

the shear modulus, r and θ are co-ordinates in a conventional polar system centered at the crack-tip [58, 59, 60].

Mode III is a special case because displacements u and v are equals to 0, while displacement w is a function of the in-plane coordinates, which means $u = v = 0$ and $w = w_{(x,y)}$. Since the displacement is only w, the only non-zero stress components are τ_{yz} and τ_{yz} and these can be defined as:

$$\tau_{xz} = -\frac{K_{III}}{\sqrt{2\pi r}} \sin\left(\frac{\theta}{2}\right) \tag{2.26}$$

$$\tau_{yz} = \frac{K_{III}}{\sqrt{2\pi r}} \cos\left(\frac{\theta}{2}\right) \tag{2.27}$$

and the displacement w is described as:

$$w = 2\frac{K_{III}}{\mu}\sqrt{\frac{r}{2\pi}}\sin\left(\frac{\theta}{2}\right) \tag{2.28}$$

where $K_{III} = \tau_{yz}\sqrt{\pi a}$ is stress intensity factor for Mode III, μ is the shear modulus, r and θ are co-ordinates in a conventional polar system centered at the crack-tip [56, 60].

The stress intensity factors K_I, K_{II} and K_{III} can be evaluated from the above relations for stress components with respect to the limit value $r \to 0$ as follows [61, 60]:

$$K_I = \lim_{r \to 0} \sqrt{2\pi r}\ \sigma_{yy(r,\theta=0)} \tag{2.29}$$

$$K_{II} = \lim_{r \to 0} \sqrt{2\pi r}\ \tau_{yx(r,\theta=0)} \tag{2.30}$$

$$K_{III} = \lim_{r \to 0} \sqrt{2\pi r}\ \tau_{yz(r,\theta=0)} \tag{2.31}$$

2.4 Relation between G and K

The above equations shown that the stress intensity factor K is an important parameter to obtain the stress field near the crack. A crack is formed when K reaches critical value K_C, this value does not depend to the geometry or shape of the specimen. Critical values is determined from experiment where specimen is made with a machine crack and loaded until failure, after failure length of the crack and maximal stress are measured. From these parameters, the value of K_C can be determinate. This values is taken as material property named toughness (resistance to fracture)

and it is assumed that the same material will fail when the K reach K_C independent of its shape and load [60].

The stress intensity factor K and it's critical value K_C and and fracture energy G is very important for fracture. The combination of these values for fracture in any of the three modes can be determined as:

$$
\begin{aligned}
G\delta a = \delta W &= 2 \times \frac{1}{2} \int_0^{\delta a} \left(\sigma_{yy,a} u_{y,a+\delta a} + \tau_{yx,a} u_{x,a+\delta a} + \ldots \right) dx \\
&= \int_0^{\delta a} \left[\frac{K_{I,a}}{\sqrt{2\pi x}} \frac{K_{I,a+\delta a}}{4\mu} \sqrt{\frac{\delta a - x}{2\pi}} \left(2\kappa + 2 \right) + \ldots \right] dx
\end{aligned}
\tag{2.32}
$$

because $K_{I,a}$ and $K_{I,a+\delta a}$ are very close together can be replaced by K_I as:

$$
= \frac{1+\nu}{2\pi E'} K_I^2 \int_0^{\delta a} \sqrt{\frac{\delta a - x}{2\pi}} \left(\kappa + 1 \right) dx + \ldots
\tag{2.33}
$$

in case $x = \delta a \sin^2 \theta$ with $dx = \delta a 2 \sin \theta \cos \theta d\theta$ the equation is:

$$
\begin{aligned}
&= \frac{1+\nu}{\pi E'} (\kappa + 1) K_I^2 \delta a \int_0^{\frac{\pi}{2}} \cos^2 \theta \, d\theta + \ldots \\
&= \frac{1+\nu}{2\pi E'} (\kappa + 1) K_I^2 \delta a \int_0^{\frac{\pi}{2}} \left(1 + \cos 2\theta \right) d\theta + \ldots
\end{aligned}
\tag{2.34}
$$

that finally obtain:

$$
G_I = \frac{K_I^2}{E'}
\tag{2.35}
$$

$$
G_{II} = \frac{K_{II}^2}{E'}
\tag{2.36}
$$

$$
G_{III} = \frac{K_{III}^2}{2\mu}
\tag{2.37}
$$

and this can be expressed as:

$$
G = \frac{K_I^2}{E'} + \frac{K_{II}^2}{E'} + \frac{K_{III}^2}{2\mu}
\tag{2.38}
$$

where $E' = E/(1-\nu^2)$ is plain strain each SIF mode contributes to the crack surface displacement and giving the property of additivity of strain energy release rate per unit of crack surface [60, 62].

Chapter 3

Experiment and Results for PA12 material

3.1 Experiment design according to EN ISO 12737

The geometry of the sample and the calculation of the fracture toughness values was designed according to EN ISO 12737 Metallic materials - Determination of plane-strain fracture toughness. Chapter 7 "Sample size, arrangement and preparation" describes that the sample width B, crack length a and ligament length W must be greater than $2,5*(K_{Ic}/R_{p0,2})^2$, where $R_{p0,2}$ the agreed yield strength of the material. Since this conditions cannot be met prior to experiments, the sample geometry must be chosen conservatively and is shown on Figure 3.1 [63].
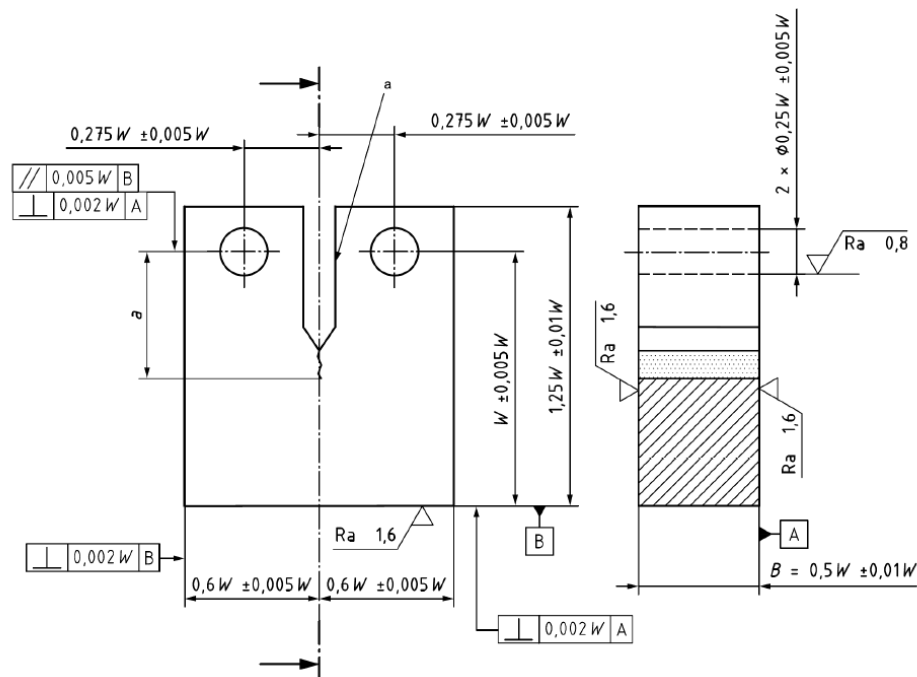
Figure 3.1: Recommended sample geometry for fracture toughness experiments according to EN ISO 12737 [63].

24

It is recommended to choose the ligament length W as twice of the sample width B. Also, the crack length a should satisfy the condition $a = (0, 45 - 0, 55) * W$. If the ratio W/B is other than 2, the norm allows for alternative dimensions where ratio should be in the interval $2 < W/B < 4$ [63].

The sample is loaded to the maximal force F_{max} which is recorded. The load curve is interspersed with the intercept F_5 from the point 0 with the directive $(F/V)_5 = 0, 95 * (F/V)_0$, where $(F/V)_0$ is tangential of the linear part. The force F_Q is determined by shape of load curve as is shown on Figure 3.2 [63].
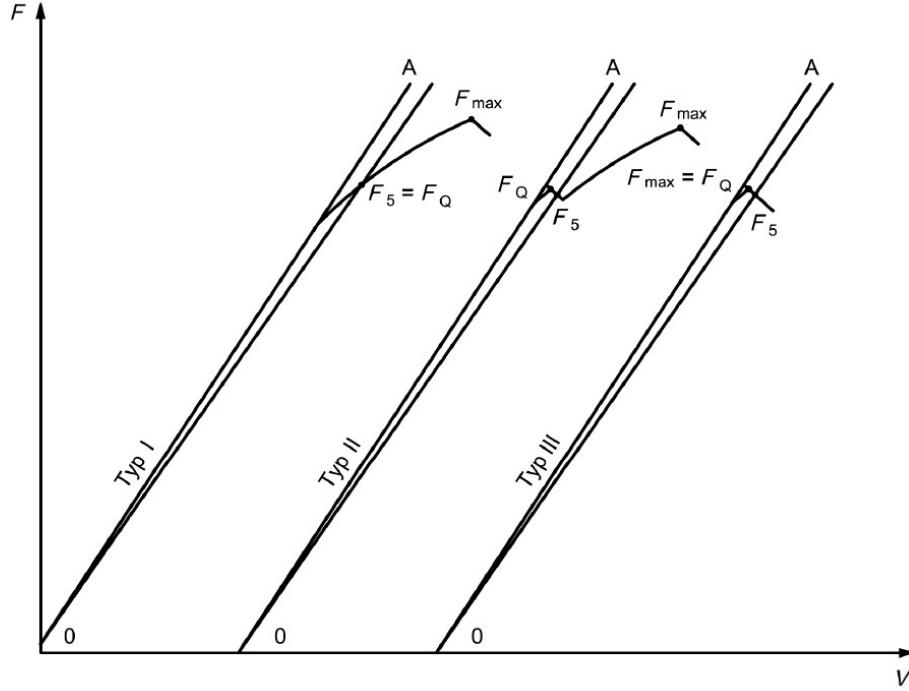
Figure 3.2: Determination of the force F_Q according to EN ISO 12737 , F is force and V is the crack opening [63].

Then the ratio F_{max}/F_Q is calculated, which must not exceed 1.1. The calculated ratio $2, 5 * (K_Q/R_{p0,2})^2$ and if it does not reach the value of sample width B, length of the ligament W and crack length a then $K_Q = K_{Ic}$. The calculation of the fracture toughness value K_Q is given in the Equation 3.1 and 3.2, where value of the F_Q is given in kilonewton and B, W are given in centimeters [63].

$$f(a/W) = (2+a/W)*\frac{0, 886 + 4, 64(a/W) - 13, 32(a/W)^2 + 14, 72(a/W)^3 - 5, 6(a/W)^4}{(1 - a/W)^{\frac{2}{3}}}$$

$$(3.1)$$

$$K_Q = \frac{F_Q}{B\sqrt{W}} * f(a/W) \tag{3.2}$$

It is important to know that I designed experiment for very thin width samples, which means that most of the condition described in EN ISO 12737 was not met. In

particular, the condition that ligament length W be twice of the sample width B was not met . The norm served as the basis for to design the samples geometry presented in Section 3.2 and to calculate the fracture toughness value presented Section 3.4.

3.2 Samples geometry for experiments

In this thesis were designed 4 types of geometry for samples. The geometry is created according to the instructions from the EN ISO 12737 [63] described detail in the Section 3.1. ARCHICAD 25 was used to create the 3D models. Sample shapes were designed using the Profile Manager and were utilized to create 3D models with 6 different thicknesses (0.50, 0.75, 1.00, 1.25, 1.50 and 2.00 mm). The 3D models can be easily exported to a .stl file, which is required for 3D printing. The dimensions of samples are shown in Figure 3.3.

SAMPLE 1
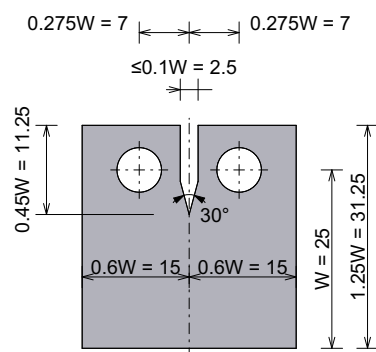
SAMPLE 2
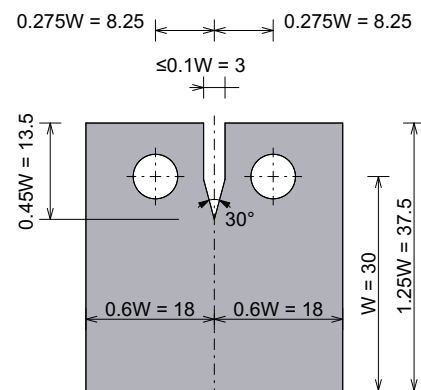
SAMPLE 3
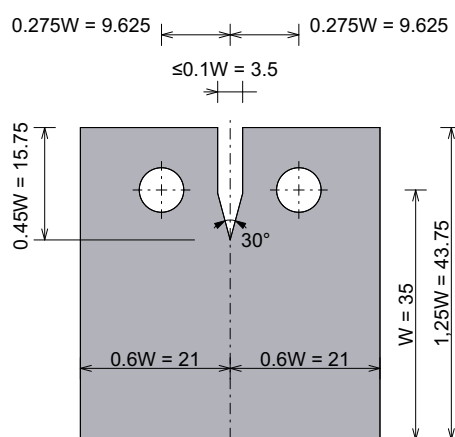
SAMPLE 4
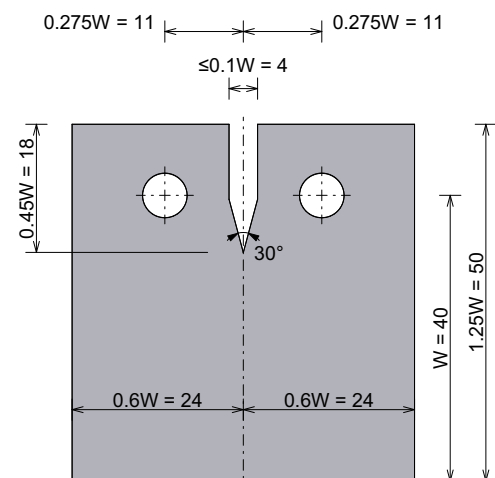
Figure 3.3: Samples geometry according to EN ISO 12737

The material used for my experiment was PA12 Smooth material, whose properties are described in Section 1.2. The material in powder form was printed on a Synterit Lisa Pro using SLS 3D printing technology. The 3D models in .stl format were imported into Sinterit Studio software, which generates the S-code for printing. The default setting values for the PA12 smooth material were generated by the software. Figure 3.4 shown the different stages of printing in Sinterit Studio.
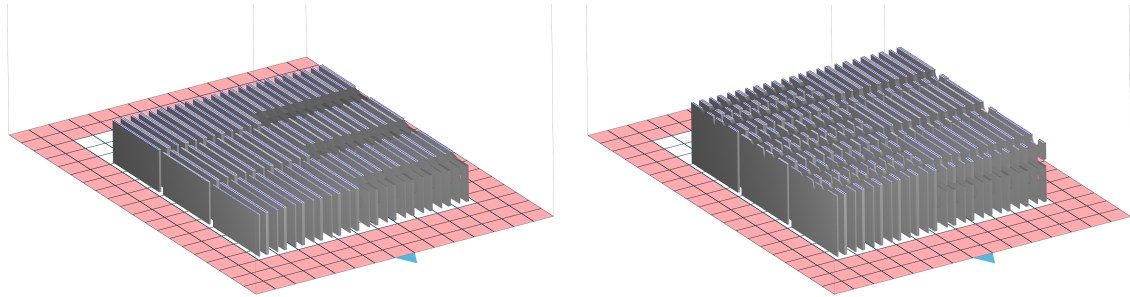
Figure 3.4: Two stages of printing process in Sinterit Studio.

As shown Figure 3.5 the printer has 2 beds, one of which is feed bed and he other is print bed. The feed bed must be filled with powder before printing. The software tells us how much powder is needed to print the samples. For example, when I printed 72 specimens of the Sample 2, I had to use about 3 liters of powder and the printing took about 26 hours. When printing, the feed bed moves up by the height of the printed layer, which is 0.125 mm in my case. As the feed bed moves up, the recoater moves from one side to the other side to spread the powder on the print bed. In this bed, the laser burns the samples according to the S-code. Figure 3.6 shows the inside the printer and the individual components.
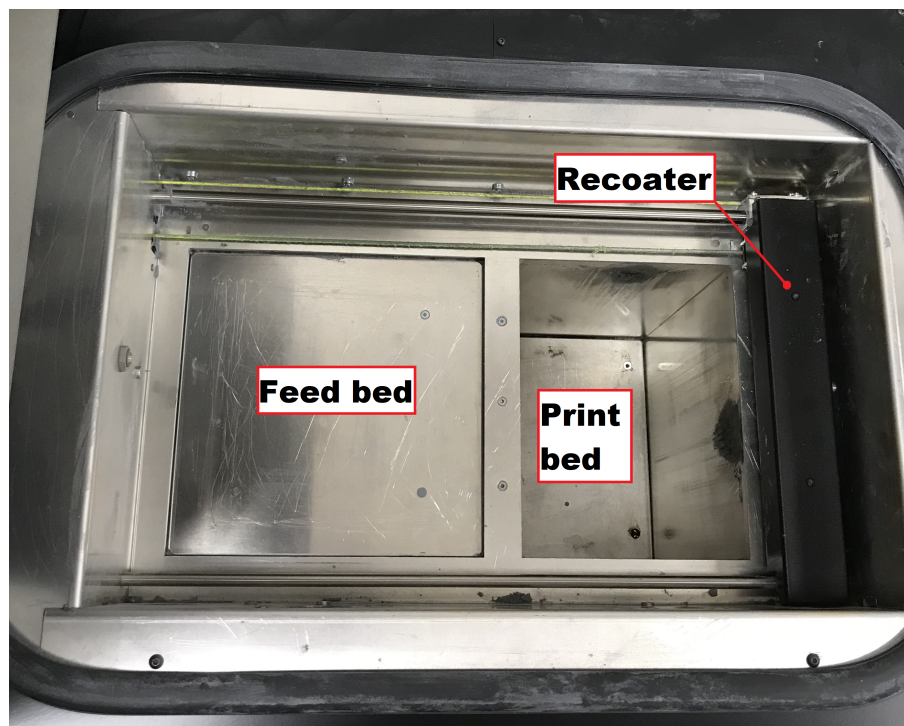
Figure 3.5: The inside of a 3D printer printing with SLS technology, a feed bed for powder filling, a print bed for printed samples and a recoater for spread the powder.
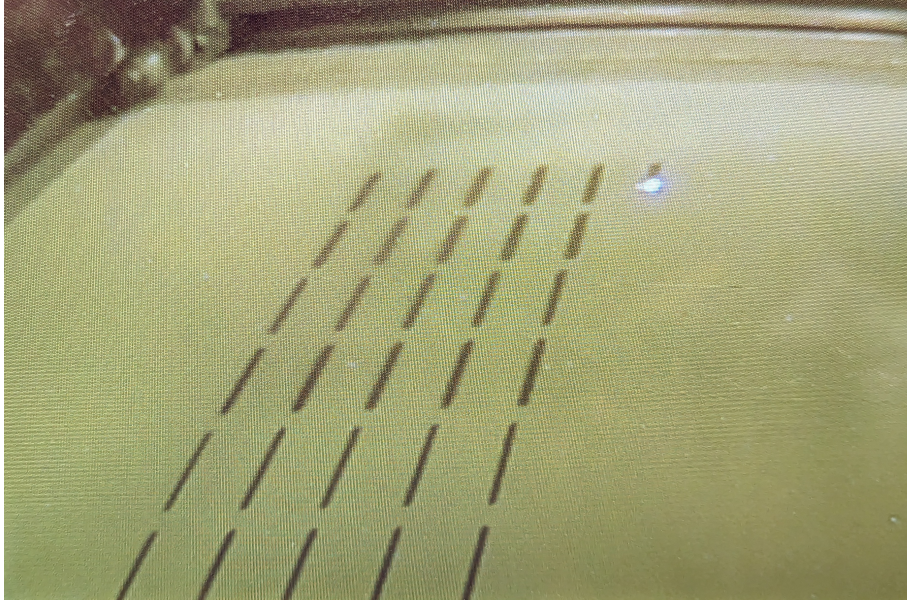
Figure 3.6: Samples during printing inside the printer.

After printing, I had to wait for the samples to cool down. ¨Then I could then remove the printed samples from the print bed and use a powder sieve to remove the dust from the samples. I roughly cleaned the dust off the samples and then I was able to clean to their final form with a fine abrasive with sandblaster as shown in Figure 3.7. For the pre-test experiment, 96 samples were printed, cleaned and prepared for the experiments, and about 140 samples were prepared for the next test.
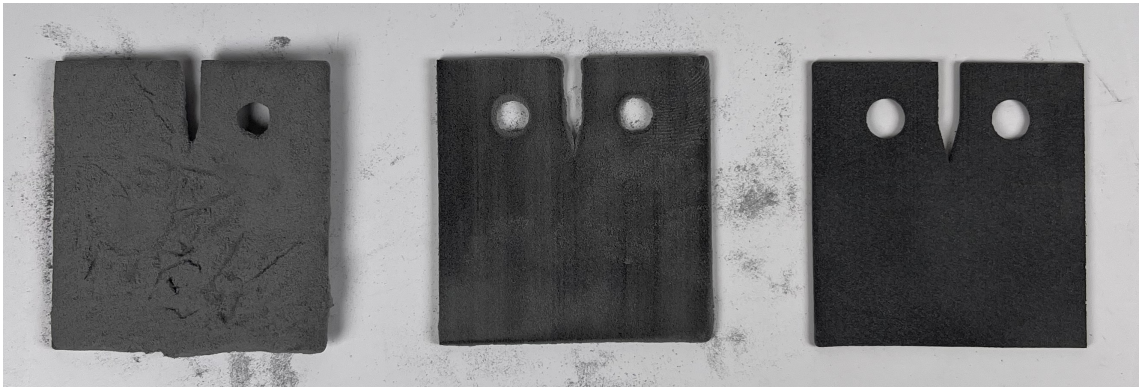
Figure 3.7: Three types of sample after printing: the left sample is fresh out of the printer, the middle sample is roughly cleaned and the right sample is cleaned with a fine abrasive.

3.3 Research experiments and pre-tests for PA12 material

First, I conducted a literature review to identify relevant experiments that shown us results of fracture toughness for 3D printed PA12 material. Other thesis indicated various differences in their findings. These differences can be attributed to different geometry, width or testing methods. The works of J. Schneider and S. Kumar focused on ligament length (10, 15 and 20 mm). In their experiment, 1 mm thickness test specimens were used and a bending test was conducted. The results revealed a dependence on ligament length, with fracture toughness K_{IC} values ranging from 3.7 to 4.5. [64] The subsequent thesis by A. Salazar investigated the influence of three distinct temperature conditions (23 °C - under dry and water-conditioned specimens, and -50 °C). The fracture toughness results under dry conditions ranged from 2.7 to 3.2, while under water-conditioned conditions, the values were observed to be around 1.3. [65] The final chosen thesis, authored by D. I. Stoia and colleagues, focused on exploring the impact of varying printing orientations and process energy. The outcomes of these experiments yielded results ranging from 0.8 to 2.2. [66]

After the literature review I started with pre-test of PA12 material produced by SLM 3D printing technology. These experiments were performed to set up the testing machine and determine the appropriate sample geometry for the following experiments. The pre-test were designed and calculated according to the procedure given in EN ISO 12737 [63]. To ensure a smaller deviation between the results, the crack length a was not measured but was considered as $0,5 * W$. The results of the pre-test experiment are shown in Table 3.1.

B [mm]	VZOREK 1	VZOREK 2	VZOREK 3	VZOREK 4
0.50	1.79 ±0.19	2.97 ±0.08	2.38 ±0.32	2.43 ±0.41
0.75	1.58 ±0.1	3.55 ±0.68	2.18 ±0.29	2.45 ±0.53
1.00	2.49 ±0.09	3.42 ±0.57	3.03 ±0.14	2.9 ±0.54
1.25	3.08 ±0.26	3.88 ±0.29	3.27 ±0.23	3.25 ±0.52
1.50	3.49 ±0.43	4.33 ±0.35	3.89 ±0.26	3.2 ±0.15
2.00	3.83 ±0.09	4.97 ±0.24	4.8 ±0.25	4.39 ±0.26

Table 3.1: Pre-test experiment results of K_Q for PA12 material.

Graphs showing the differences in values of fracture toughness for different geometries and width of samples are shown on Figure 3.8. For each sample, graphs were created indicating the error rates of the result. These graphs were interleaved with a linear line to find the best fit to the curve of fracture toughness values. The graphs for each sample can be seen in Figure 3.9.
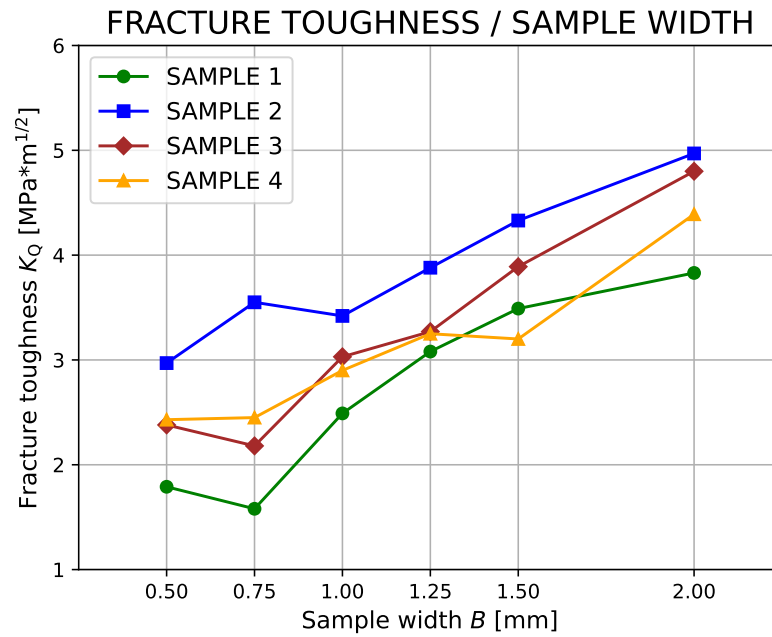
Figure 3.8: Graph with fracture toughness values for different samples geometries and different thicknesses. The values are used from Table 3.1.
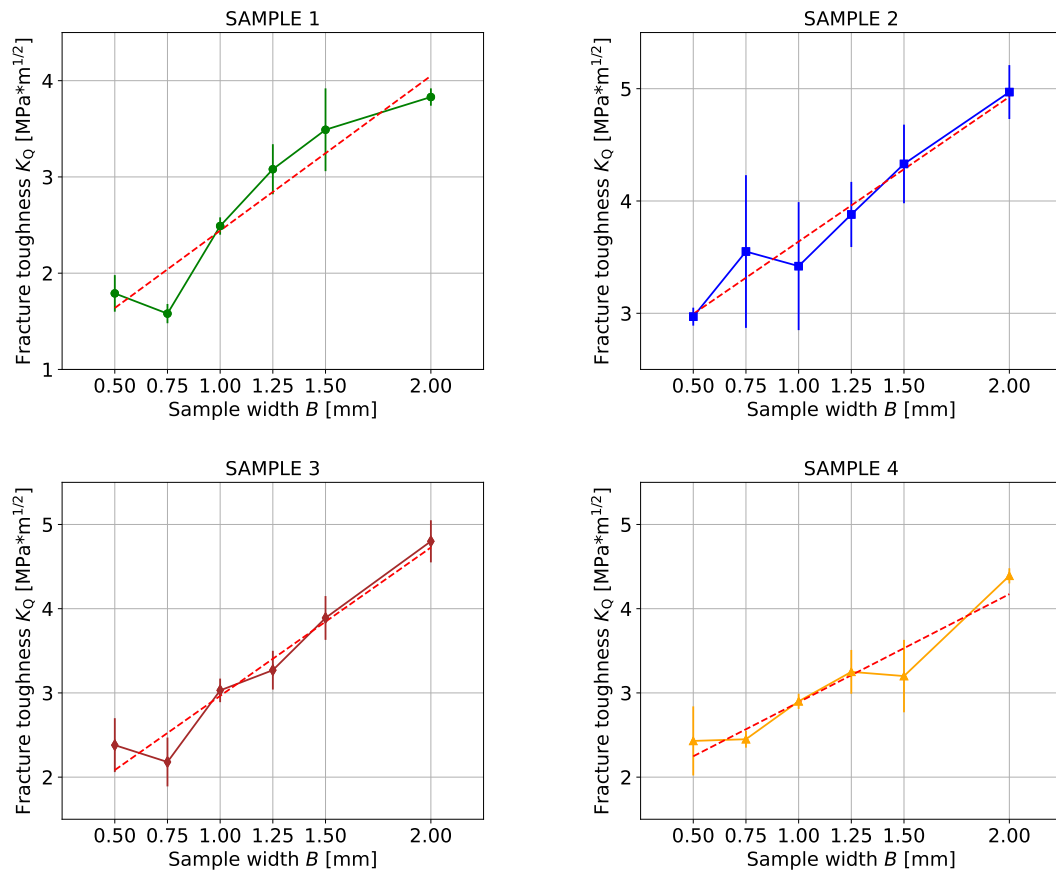
Figure 3.9: Graphs with fracture toughness values as a function of the thickness of each samples. The graph shows the deviation of the values obtained. The curve is interleaved with a straight line representing a linear progression.

The main factor in the selection of samples for future experiment was the fit of linear line to the curve of fracture toughness values. Another factor in the selection of the sample was the torsion of the sample at its free end during the loading. Torsion was not investigated in detail in pre-test, but less torsion can be expected for smaller samples. For example, Sample 4 has a free end length from the grips of approximately 40 mm, whereas for Sample 1 this length is 25 mm, therefore less torsion of the end of Sample 1 can be expected. Sample loading and cleaning manipulation were the final factor for sample selection.

From these criteria and the values obtained, **SAMPLE 2** and **SAMPLE 3** were selected. These samples had ideal dimensions for manipulation in the experiments, their curve is sufficiently coincident with a linear line and their free edge lengths are lower than those of Sample 4. After this selection, an experiment were designed for two orientation of printed samples, which are shown in Figure 3.10. The polyamide powder layers were laser sintered at a different angles, where H sample layers are designed to be perpendicular to the potential crack propagation and the V samples have the layers printed parallel to the potential crack propagation.
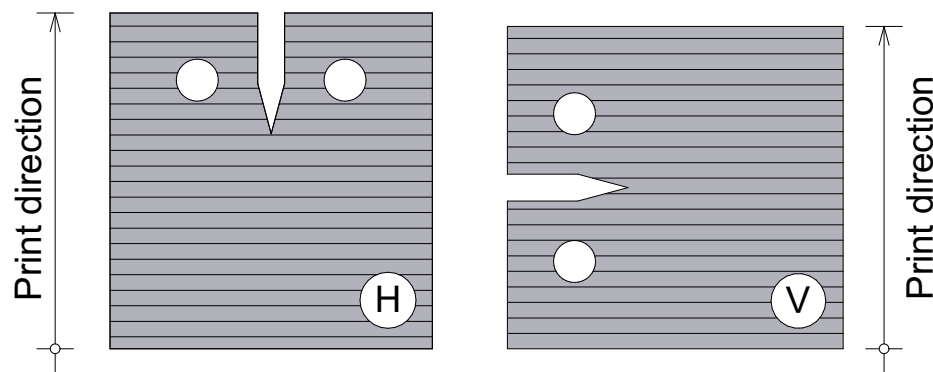
Figure 3.10: Demonstration of the two types of different sample printing orientations.

3.4 Fracture toughness results

After pre-test of 4 types of samples and selecting 2 types for further experiments, I started testing samples in different print orientation. The measurement set-up included Mark-10 load press and 3D macro digital image correlation (DIC) consisting of 2 cameras and lighting, as shown in Figure 3.11. Both of these measurement instruments were connected to a laptop computer with software IntelliMESUR recording the values from the Mark-10 loading and Instra 4D V4.10 software capturing and post-processing the 3D DIC images.
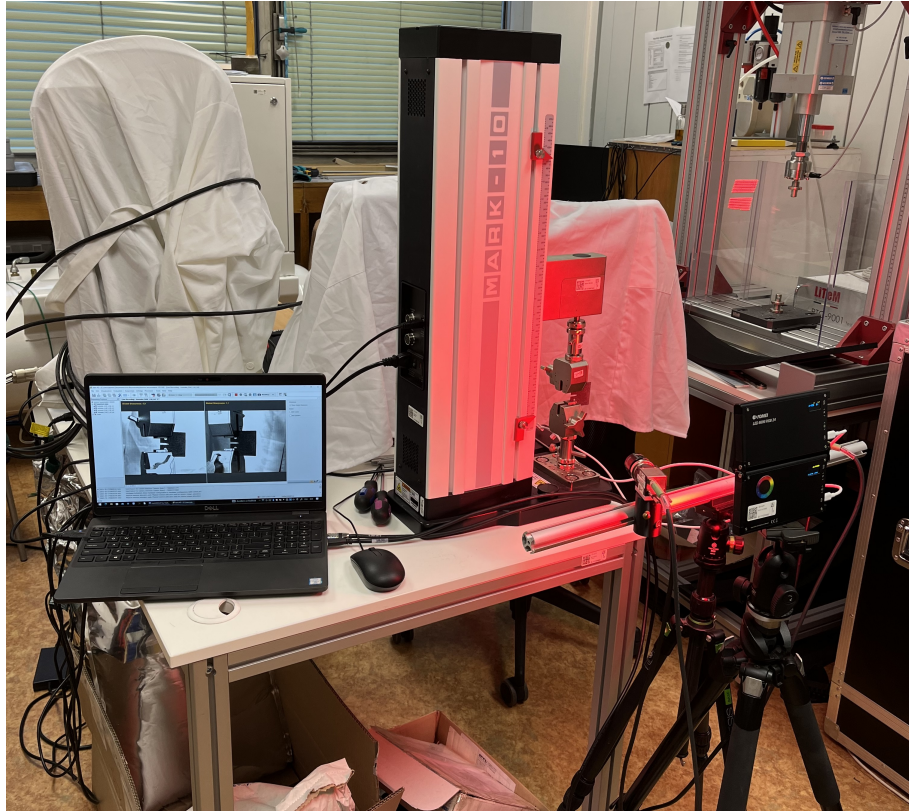
Figure 3.11: A measurement set-up including of a Mark-10 load press and 3D DIC consisting of 2 cameras and lighting. Both of these measuring machines are connected to laptop computer, which stores data from the experiment.

For DIC measurements, the sample must be provided by speckle pattern. This pattern is used to mark out points from which the displacement of the specimen can be monitored or stress and strains values can be calculated. The DIC follows the processing of two consecutive images taken from different loading phases. The images are divided into small subset windows and these subsets are monitored. These subsets are also known as zones of interest. In the Figure 3.12 is shown basic principles of subset monitoring in DIC [67].
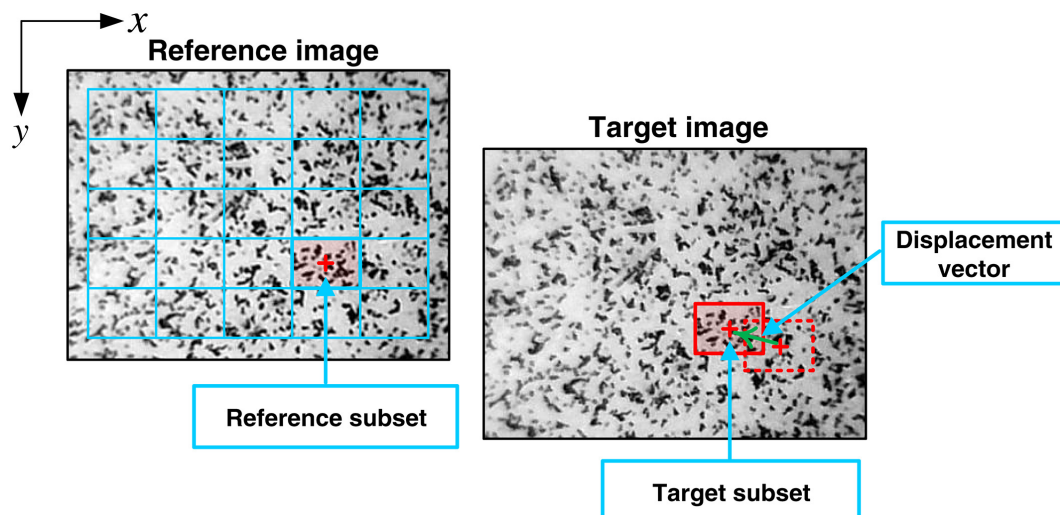
Figure 3.12: Scheme of subset displacement before and after sample deformation [67].

Based on sensitivity of DIC, it is necessary to create a very fine pattern so that the software can more easily find as many subsets as possible, also labeled as starting points. To create the speckle pattern on my samples, I used spray paint with white and black. I applied white paint first, which served as a base and highlight for the second layer of black paint. The black paint had to be applied very sensitive to made small dots as it shown in Figure 3.13 on left sample.
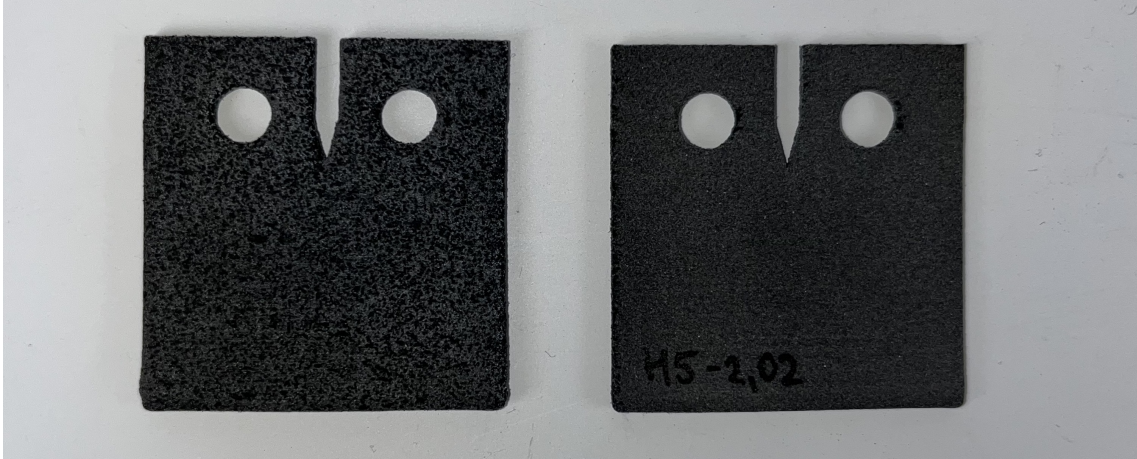
Figure 3.13: The sample on left with the speckle pattern before the experiment, the sample on the right without speckle pattern.

The use of DIC has proven very important for my experiment. In more than one quarter of the specimens, crack propagation occurred along the entire length of specimen and it was very difficult to stop the loading before the specimen deformed completely. This problem solved DIC, where from the low images taken, it was possible to find an image that showed the length of the crack before the specimen was fully deformed. For example, Figure 3.14 shown two different steps before and after the sample is destroy by the crack. The left image (step 54) was the last image before full deformation and from this image the crack length can be determined.
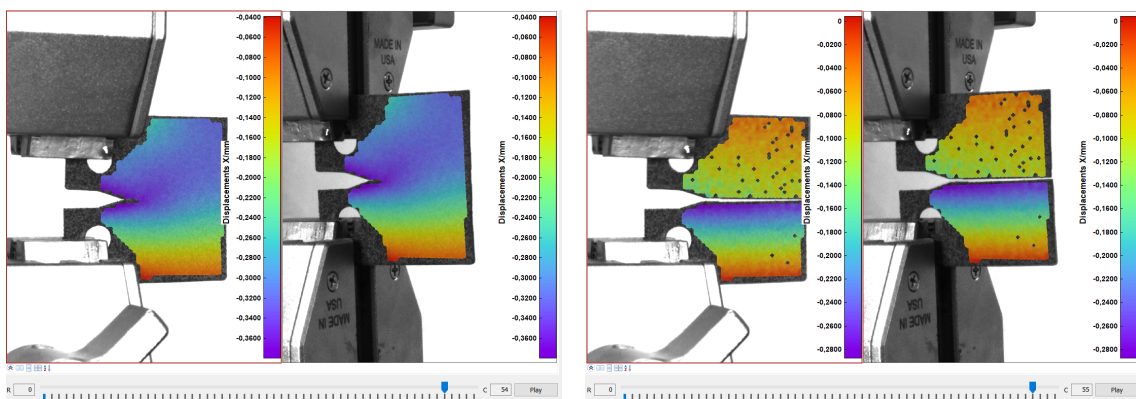
Figure 3.14: Two images showing the crack formation on left (step 54) and crack propagation along the length of the specimen on right (step 55).

I used a function in Instra 4D V4.10 named line gauge object to determine the length of the crack. This function defines two points that then crate a line. This line can display many parameters such as the position of the points or the length of

the points between each other, which was an important parameter for me. I tried to place the first point near the tip where crack propagation started, and I placed the second point at the end of the crack length, as shown in Figure 3.15.
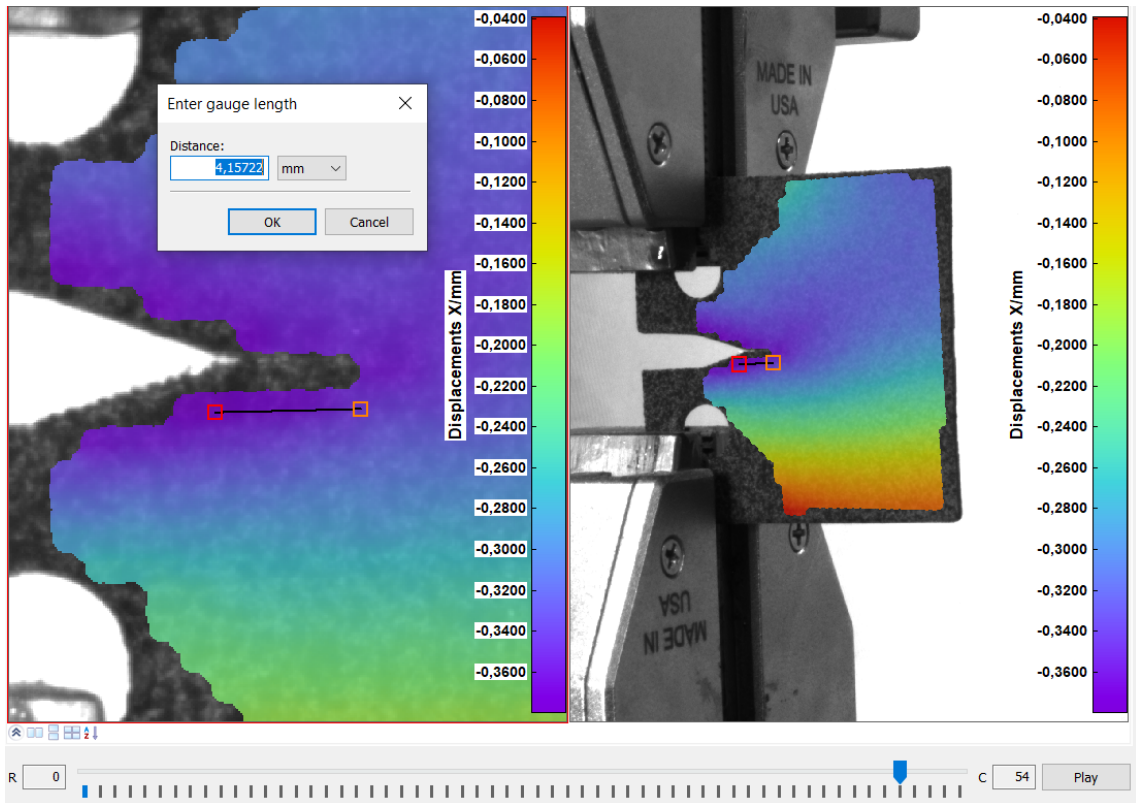
Figure 3.15: Example of determining the crack length in Istra 4D by using function line.

Samples with crack length determined by DIC are marked with * in Section 3.4.1 and Section 3.4.2. The second marking of samples marked with + is for samples where the crack propagation did not start at the tip but at another location. Both of these cracks propagation problems are illustrated in Figure 3.16.
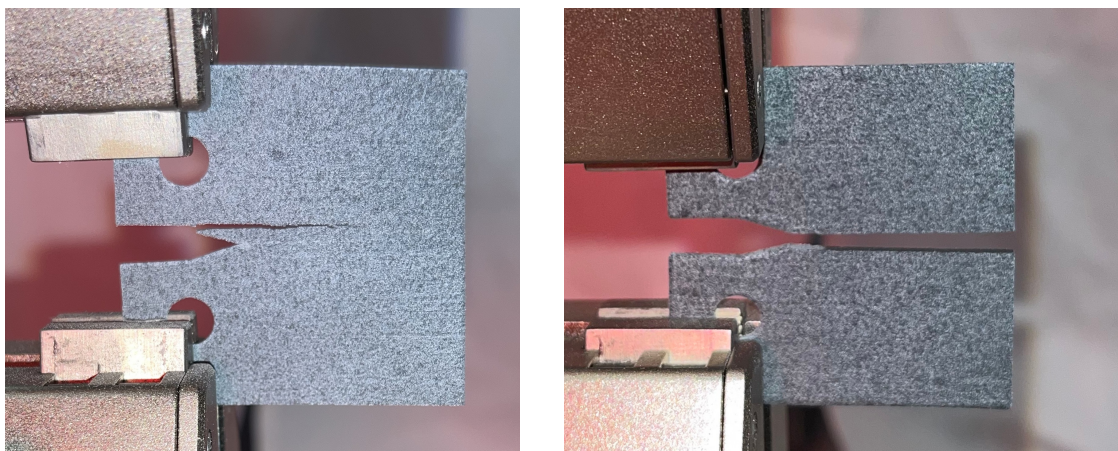
Figure 3.16: A sample with a crack not propagating at the tip in the left image and a sample with crack propagation entire length of the specimen in the right image.

3.4.1 Experimental data - SAMPLE 2

In this section, data of the SAMPLE 2 measurements are processed. First, I started with test on SAMPLE 2 printed in the horizontal direction. Because crack propagation in specimens printed in the horizontal direction is affected by the orientation of printed layers, it was easy to stop loading before the crack propagated the full length of the specimen. The crack propagation on SAMPLE 2 specimens printed in the horizontal direction is shown in Figure 3.17.

Figure 3.17: Cracks of all SAMPLE 2 for PA12 material printed in horizontal direction.

The processed data are shown in Figure 3.18, where six graphs containing load diagrams for each specimens with different widths are presented. The x-axis shows distance in millimetres and the y-axis shows the load in newtons. These graphs shown relationship between the width of the specimens and the maximum load for crack formation.
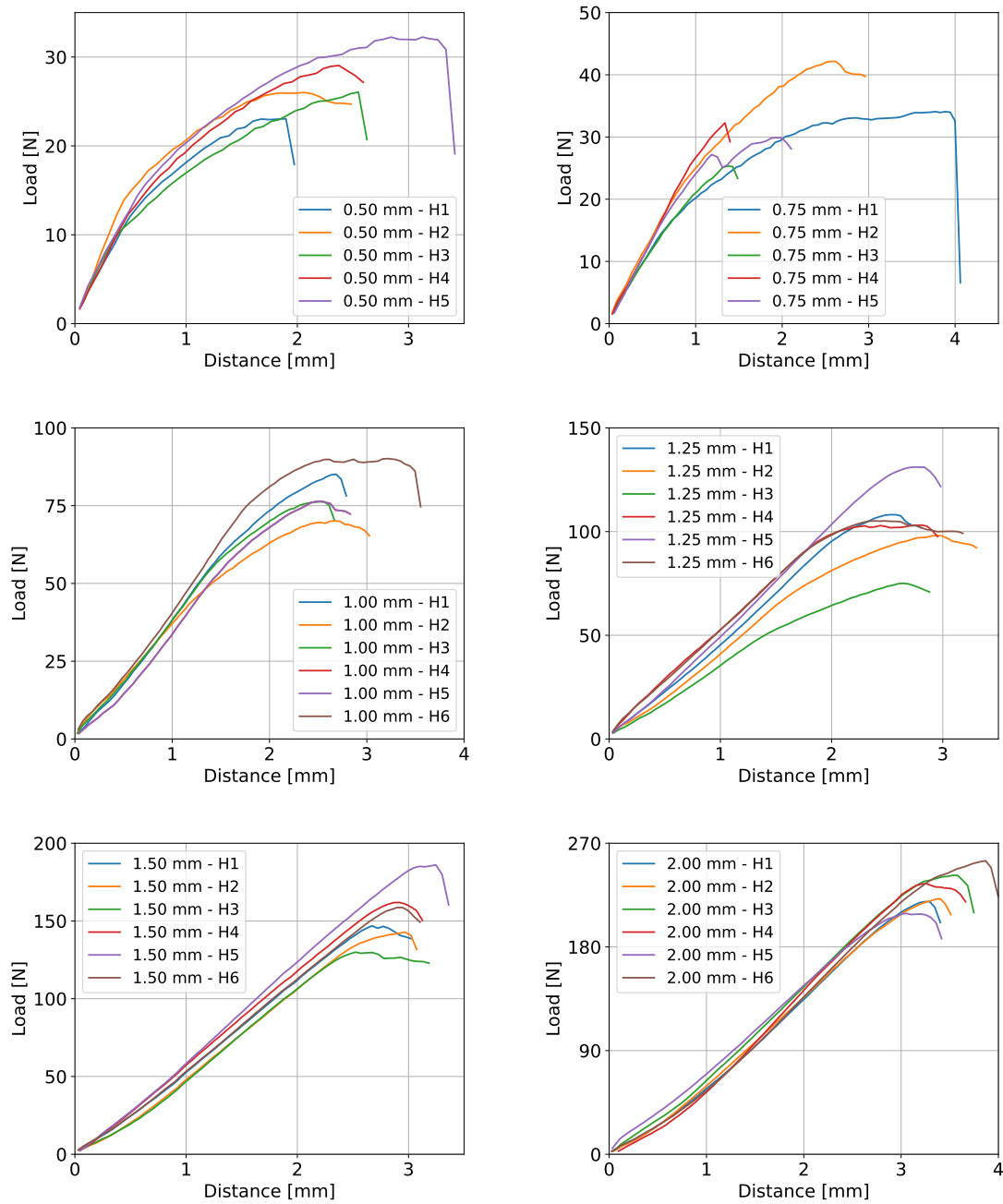
Figure 3.18: Load-distance graph for different width of SAMPLE 2 for PA12 material printed in horizontal direction. The x-axis represents the press displacement, while the y-axis represents the load necessary for achieving displacement.

The values for calculating the fracture toughness of the specimens K_Q are given in Table 3.2 and Table 3.3, where a is measured the crack length, B is the measured specimen width, W is the ligament length and F_Q is the reduced maximum force. The marking with * is for samples where the crack length had to be determined by 3D DIC. Specimens marked [+] are samples where the crack did not occur at the beginning of the tip , but at a different location.

SAMPLE	a	B	W	F_Q	K_Q
	[mm]	[mm]	[mm]	[N]	[MPa$\sqrt{\text{m}}$]
H1 - 0.50	7.88	0.54	30	25.65	1.4
H2 - 0.50	10.34	0.53	30	28.5	1.96
H3 - 0.50	6.64	0.51	30	27.55	1.42
H4 - 0.50	6.67	0.60	30	31.35	1.38
H5 - 0.50	6.61	0.59	30	35.15	1.56
H1 - 0.75	12.24	0.7	30	36.1	2.21
H2 - 0.75	4.73	0.74	30	43.7	1.28
H3 - 0.75	4.13	0.72	30	27.55	0.77
H4 - 0.75	7.94	0.77	30	34.2	1.31
H5 - 0.75	5.92	0.73	30	31.35	1.05
H1 - 1.00	5.07	1.07	30	82.65	1.73
H2 - 1.00	4.54	1.05	30	70.3	1.42
H3 - 1.00	4.32	1.05	30	76.95	1.51
H4 - 1.00	3.57	1.01	30	76.95	1.44
H5 - 1.00	5.43	1.03	30	76.95	1.74
H6 - 1.00	5.56	1.01	30	88.35	2.06
H1 - 1.25	5.23	1.29	30	105.45	1.86
H2 - 1.25	5.43	1.2	30	95.95	1.86
H3 - 1.25	7.87	1.22	30	74.1	1.79
H4 - 1.25	4.57	1.22	30	100.7	1.75
H5 - 1.25	4.02	1.32	30	127.3	1.92
H6 - 1.25	5.7	1.21	30	102.6	2.03

Table 3.2: Values used to calculate the fracture toughness of SAMPLE 2 printed in the horizontal direction with widths of 0.50 - 1.25 mm.

SAMPLE	a	B	W	F_Q	K_Q
	[mm]	[mm]	[mm]	[N]	[MPa$\sqrt{m}$]
H1 - 1.50	3.73	1.49	30	141.55	1.83
H2 - 1.50	4.2	1.48	30	137.75	1.89
H3 - 1.50	4.31	1.41	30	125.4	1.83
H4 - 1.50	3.43	1.55	30	155.8	1.86
H5 - 1.50 *	6.39	1.55	30	178.6	2.95
H6 - 1.50	6.74	1.56	30	152.0	2.58
H1 - 2.00	3.6	2.06	30	210.9	1.94
H2 - 2.00	4.94	2.08	30	212.8	2.26
H3 - 2.00 *	4.55	2.09	30	232.75	2.36
H4 - 2.00	4.76	2.04	30	225.15	2.39
H5 - 2.00	5.3	2.02	30	200.45	2.28
H6 - 2.00	6.7	2.17	30	244.15	2.97

Table 3.3: Values used to calculate the fracture toughness of SAMPLE 2 printed in the horizontal direction with widths of 1.50 and 2.00 mm.

A summary of the fracture toughness results for SAMPLE 2 printed in horizontal direction are given by Table 3.4.

B [mm]	H1	H2	H3	H4	H5	H6
0.50	1.40	1.96	1.42	1.38	1.56	-
0.75	2.21	1.28	0.77	1.61	1.05	-
1.00	1.73	1.42	1.51	1.44	1.74	2.06
1.25	1.86	1.86	1.79	1.75	1.92	2.03
1.50	1.83	1.89	1.83	1.86	2.95*	2.58
2.00	1.94	2.26	2.36*	2.39	2.28	2.97

Table 3.4: Experiment results of K_Q for SAMPLE 2 printed in horizontal direction.

I continued the experiment on SAMPLE 2 printed in the vertical direction. The cracks in specimens printed in vertical direction propagated parallel to the print layers and were therefore always straight and along the entire length of the specimen. This problem was particularly prevalent in thicker samples (1.25 - 2.00 mm). The problem with the thinner specimens was that crack propagate beyond the tips. The crack propagation on SAMPLE 2 specimens printed in the vertical direction is shown in Figure 3.19.

Figure 3.19: Cracks of all SAMPLE 2 for PA12 material printed in vertical direction.

The processed data are shown in Figure 3.20, where six graphs containing load diagrams for each specimens with different widths are presented. The x-axis shows distance in millimetres and the y-axis shows the load in newtons. These graphs shown relationship between the width of the specimens and the maximum load for crack formation.

Figure 3.20: Load-distance graph for different width of SAMPLE 2 for PA12 material printed in vertical direction. The x-axis represents the press displacement, while the y-axis represents the load necessary for achieving displacement.

The values for calculating the fracture toughness of the specimens K_Q are given in Table 3.5 and Table 3.6, where a is measured the crack length, B is the measured specimen width, W is the ligament length and F_Q is the reduced maximum force. The marking with * is for samples where the crack length had to be determined by 3D DIC. Specimens marked [+] are samples where the crack did not occur at the beginning of the tip , but at a different location.

SAMPLE	a [mm]	B [mm]	W [mm]	F_Q [N]	K_Q [MPa$\sqrt{\text{m}}$]
V1 - 0.50$^+$	13.79	0.6	30	16.15	1.33
V2 - 0.50	4.37	0.57	30	14.25	0.52
V3 - 0.50	5.95	0.57	30	17.1	0.74
V4 - 0.50$^+$	14.96	0.53	30	15.2	1.59
V5 - 0.50	5.38	0.58	30	19.0	0.76
V6 - 0.50$^+$	10.11	0.52	30	14.25	0.98
V1 - 0.75$^+$	7.84	0.69	30	17.1	0.73
V2 - 0.75$^+$	6.99	0.67	30	14.25	0.58
V3 - 0.75$^+$	7.24	0.72	30	17.1	0.66
V4 - 0.75	6.84	0.7	30	19.95	0.76
V5 - 0.75	9.23	0.7	30	19.0	0.9
V1 - 1.00	6.99	1.02	30	38.0	1.01
V2 - 1.00	4.54	1.01	30	36.1	0.76
V3 - 1.00	5.13	1.01	30	39.9	0.89
V4 - 1.00	5.23	1.03	30	38.95	0.86
V5 - 1.00	5.06	1.01	30	42.75	0.95
V6 - 1.00	6.32	0.99	30	42.75	1.1
V1 - 1.25 *	4.96	1.28	30	59.85	1.04
V2 - 1.25 *	5.01	1.32	30	64.6	1.09
V3 - 1.25 *	4.37	1.26	30	56.05	0.92
V4 - 1.25 *	4.77	1.26	30	58.9	1.01
V5 - 1.25 *	4.01	1.27	30	68.4	1.07

Table 3.5: Values used to calculate the fracture toughness of SAMPLE 2 printed in the vertical direction with widths of 0.50 - 1.25 mm.

SAMPLE	a	B	W	F_Q	K_Q
	[mm]	[mm]	[mm]	[N]	[MPa$\sqrt{\text{m}}$]
V1 - 1.50 *	4.16	1.45	30	67.45	0.94
V2 - 1.50 *	3.76	1.47	30	78.85	1.03
V3 - 1.50 *	3.11	1.47	30	78.85	0.95
V4 - 1.50 *	3.24	1.47	30	76.0	0.93
V5 - 1.50 *	4.03	1.48	30	73.15	0.99
V6 - 1.50 *	2.78	1.41	30	66.5	0.8
V1 - 2.00	8.34	2.02	30	105.45	1.6
V2 - 2.00	7.37	1.92	30	88.35	1.29
V3 - 2.00 *	4.25	2.0	30	102.6	1.05
V4 - 2.00 *	5.48	2.0	30	111.15	1.3
V5 - 2.00 *	5.23	1.98	30	101.65	1.17
V6 - 2.00 *	4.05	2.01	30	94.05	0.93

Table 3.6: Values used to calculate the fracture toughness of SAMPLE 2 printed in the vertical direction with widths of 1.50 and 2.00 mm.

A summary of the fracture toughness results for SAMPLE 2 printed in vertical direction are given by Table 3.7.

B [mm]	V1	V2	V3	V4	V5	V6
0.50	1.33[+]	0.52	0.74	1.59[+]	0.76	0.98[+]
0.75	0.73[+]	0.58[+]	0.66[+]	0.76	0.9	-
1.00	1.01	0.76	0.89	0.86	0.95	1.1
1.25	1.04*	1.09*	0.92*	1.01*	1.07*	-
1.50	0.94*	1.03*	0.95*	0.93*	0.99*	0.8*
2.00	1.6	1.29	1.05*	1.3*	1.17*	0.93*

Table 3.7: Experiment results of K_Q for SAMPLE 2 printed in vertical direction.

3.4.2 Experimental data - SAMPLE 3

In this section, data of the SAMPLE 3 measurements are processed. Crack propagation in specimens printed in the horizontal direction was still affected by the orientation of printed layers, but the crack length was much greater than in SAMPLE 2. The crack in this case often changes their direction depending on the printed layers. The crack propagation on SAMPLE 3 specimens printed in the horizontal direction is shown in Figure 3.21.

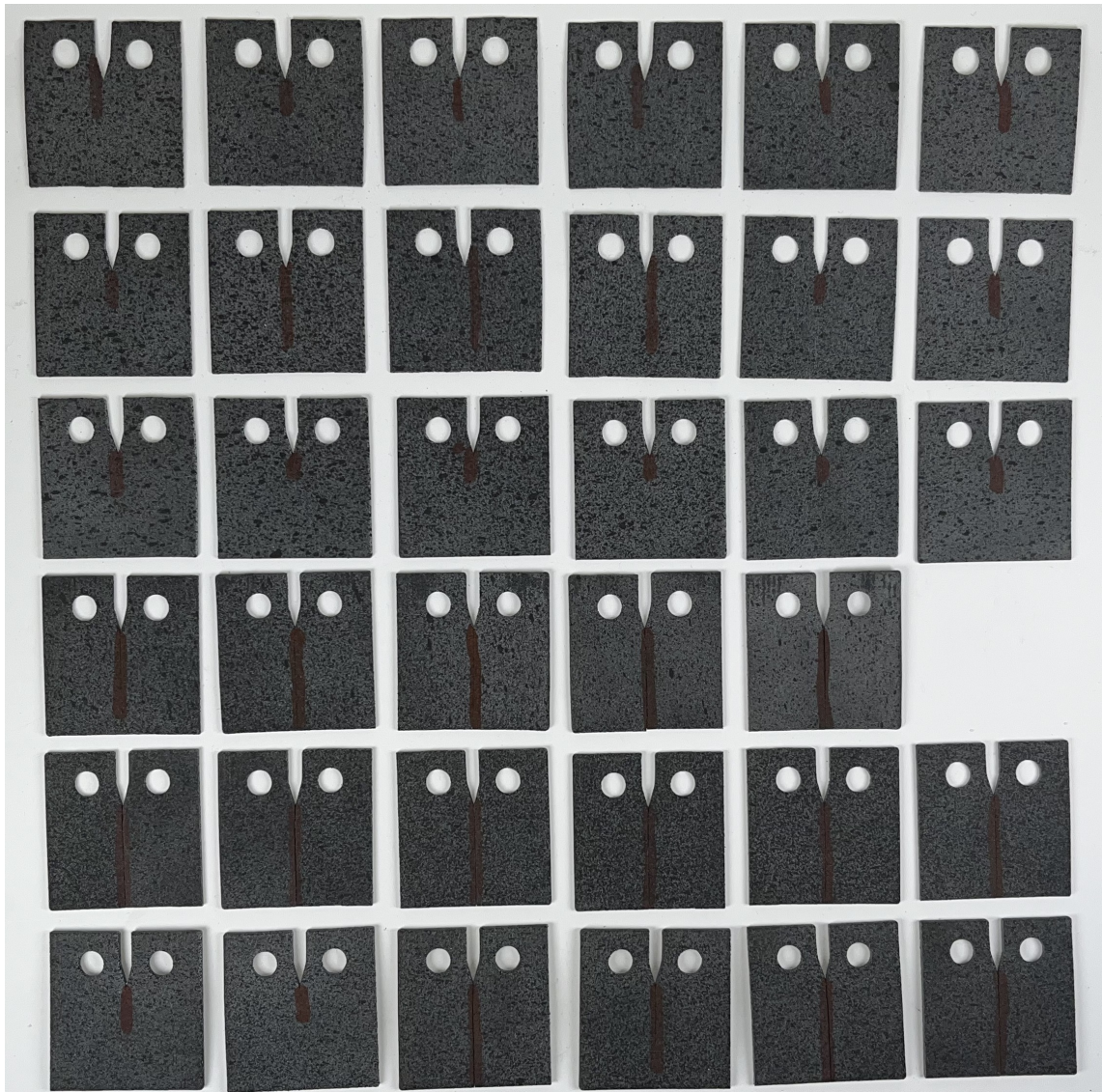**Figure 3.21:** Cracks of all SAMPLE 3 for PA12 material printed in horizontal direction.

The processed data are shown in Figure 3.22, where six graphs containing load diagrams for each specimens with different widths are presented. The x-axis shows distance in millimetres and the y-axis shows the load in newtons. These graphs shown relationship between the width of the specimens and the maximum load for crack formation.
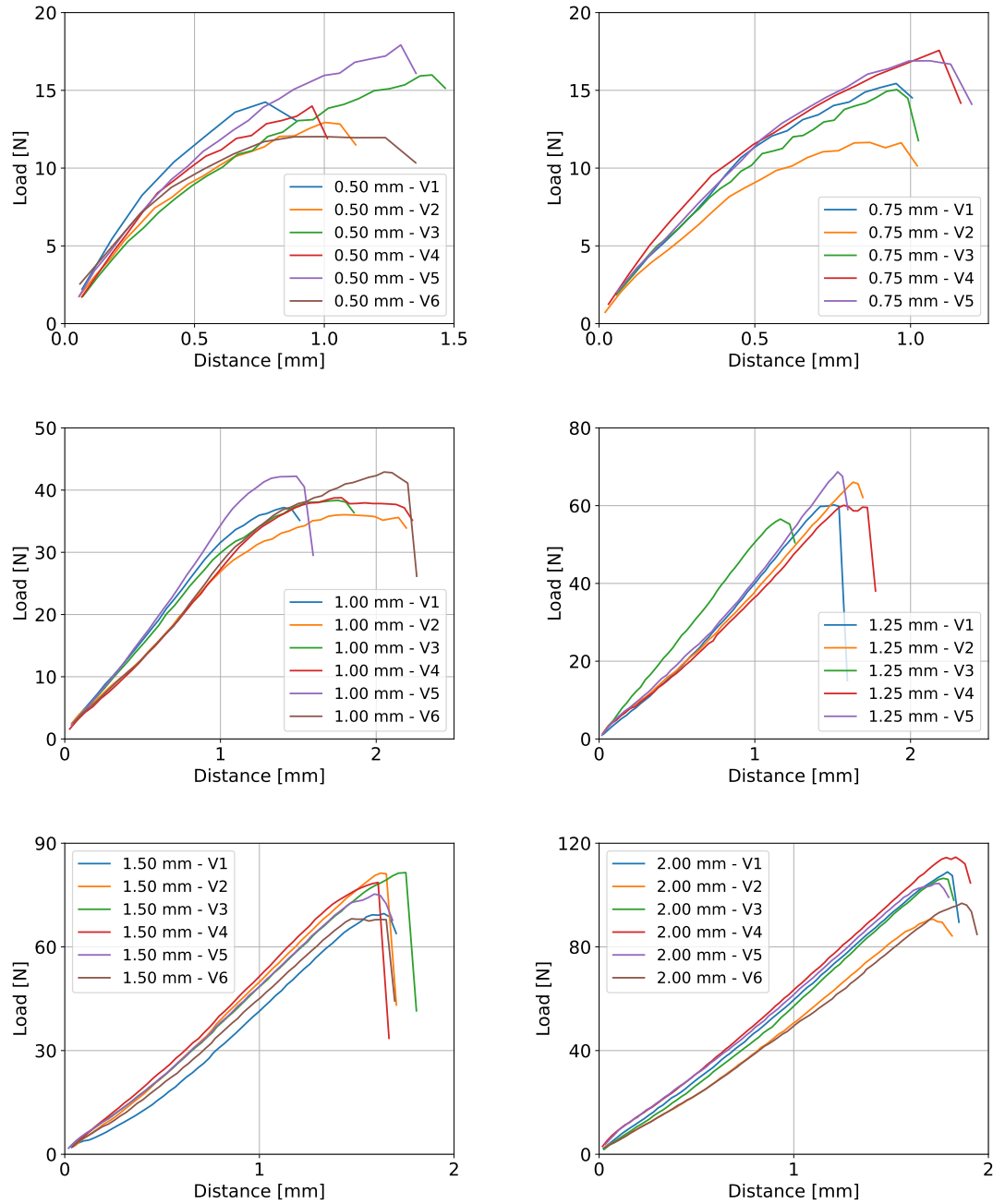
Figure 3.22: Load-distance graph for different width of SAMPLE 3 for PA12 material printed in horizontal direction. The x-axis represents the press displacement, while the y-axis represents the load necessary for achieving displacement.

The values for calculating the fracture toughness of the specimens K_Q are given in Table 3.8 and Table 3.9, where a is measured the crack length, B is the measured specimen width, W is the ligament length and F_Q is the reduced maximum force. The marking with * is for samples where the crack length had to be determined by 3D DIC. Specimens marked [+] are samples where the crack did not occur at the beginning of the tip , but at a different location.

SAMPLE	a [mm]	B [mm]	W [mm]	F_Q [N]	K_Q [MPa$\sqrt{m}$]
H1 - 0.50	9.64	0.61	35	36.1	1.67
H2 - 0.50	9.28	0.59	35	29.45	1.37
H3 - 0.50	11.63	0.54	35	30.4	1.84
H4 - 0.50	14.94	0.56	35	41.8	3.12
H5 - 0.50 *	9.54	0.59	35	41.8	1.98
H1 - 0.75	16.81	0.76	35	64.6	4.13
H2 - 0.75	19.05	0.78	35	53.2	4.06
H3 - 0.75	15.32	0.76	35	45.6	2.58
H4 - 0.75	4.03	0.8	35	53.2	1.14
H5 - 0.75 *	7.58	0.8	35	61.75	1.85
H6 - 0.75	11.77	0.75	35	46.55	2.05
H1 - 1.00 *	3.47	1.08	35	105.45	1.57
H2 - 1.00 *	3.32	1.06	35	82.65	1.24
H3 - 1.00 *	3.77	0.96	35	84.55	1.47
H4 - 1.00	4.81	1.06	35	82.65	1.45
H5 - 1.00	6.4	1.02	35	80.75	1.72
H6 - 1.00 *	4.21	0.97	35	85.5	1.54
H1 - 1.25	5.98	1.26	35	112.1	1.86
H2 - 1.25 *	8.04	1.25	35	122.55	2.44
H3 - 1.25	4.96	1.2	35	94.05	1.48
H4 - 1.25 *	4.16	1.21	35	86.45	1.25
H5 - 1.25 *	5.32	1.22	35	114.0	1.83
H6 - 1.25 *	5.12	1.19	35	94.05	1.52

Table 3.8: Values used to calculate the fracture toughness of SAMPLE 3 printed in the horizontal direction with widths of 0.50 - 1.25 mm.

SAMPLE	a	B	W	F_Q	K_Q
	[mm]	[mm]	[mm]	[N]	[MPa$\sqrt{m}$]
H1 - 1.50	7.35	1.57	35	126.35	1.89
H2 - 1.50 *	4.53	1.59	35	159.6	1.82
H3 - 1.50 *	4.2	1.57	35	173.85	1.94
H4 - 1.50 *	5.5	1.53	35	158.65	2.07
H5 - 1.50 *	6.87	1.55	35	185.25	2.7
H6 - 1.50 *	3.65	1.57	35	156.75	1.64
H1 - 2.00	7.01	1.99	35	209.0	2.4
H2 - 2.00 *	2.97	2.11	35	229.9	1.65
H3 - 2.00 *	6.11	2.09	35	212.8	2.15
H4 - 2.00 *	4.24	1.97	35	211.85	1.89
H5 - 2.00 *	6.32	1.97	35	210.9	2.31
H6 - 2.00 *	7.41	2.06	35	243.2	2.79

Table 3.9: Values used to calculate the fracture toughness of SAMPLE 3 printed in the horizontal direction with widths of 1.50 and 2.00 mm.

A summary of the fracture toughness results for SAMPLE 3 printed in hotizontal direction are given by Table 3.10.

B [mm]	H1	H2	H3	H4	H5	H6
0.50	1.67	1.37	1.84	3.12	1.98*	-
0.75	4.13	4.06	2.58	1.14	1.85*	2.05
1.00	1.57*	1.24*	1.47*	1.45	1.72	1.54*
1.25	1.86	2.44 *	1.48	1.25 *	1.83*	1.52
1.50	1.89	1.82*	1.94*	2.07*	2.7*	1.64*
2.00	2.4	1.65*	2.15*	1.89*	2.31*	2.79*

Table 3.10: Experiment results of K_Q for SAMPLE 3 printed in horizontal direction.

Last I performed an experiment with SAMPLE 3 printed in the vertical direction. The cracks in specimens printed in vertical direction again propagated parallel to the print layers and were always straight. In contrast to SAMPLE 2 printed in vertical direction, the crack length did not propagate along the entire length of the specimen, it only occurred only in specimens with width 2.00 mm. The problem with the thinner specimens was that crack propagate beyond the tips. The crack propagation on SAMPLE 2 specimens printed in the vertical direction is shown in Figure 3.23.
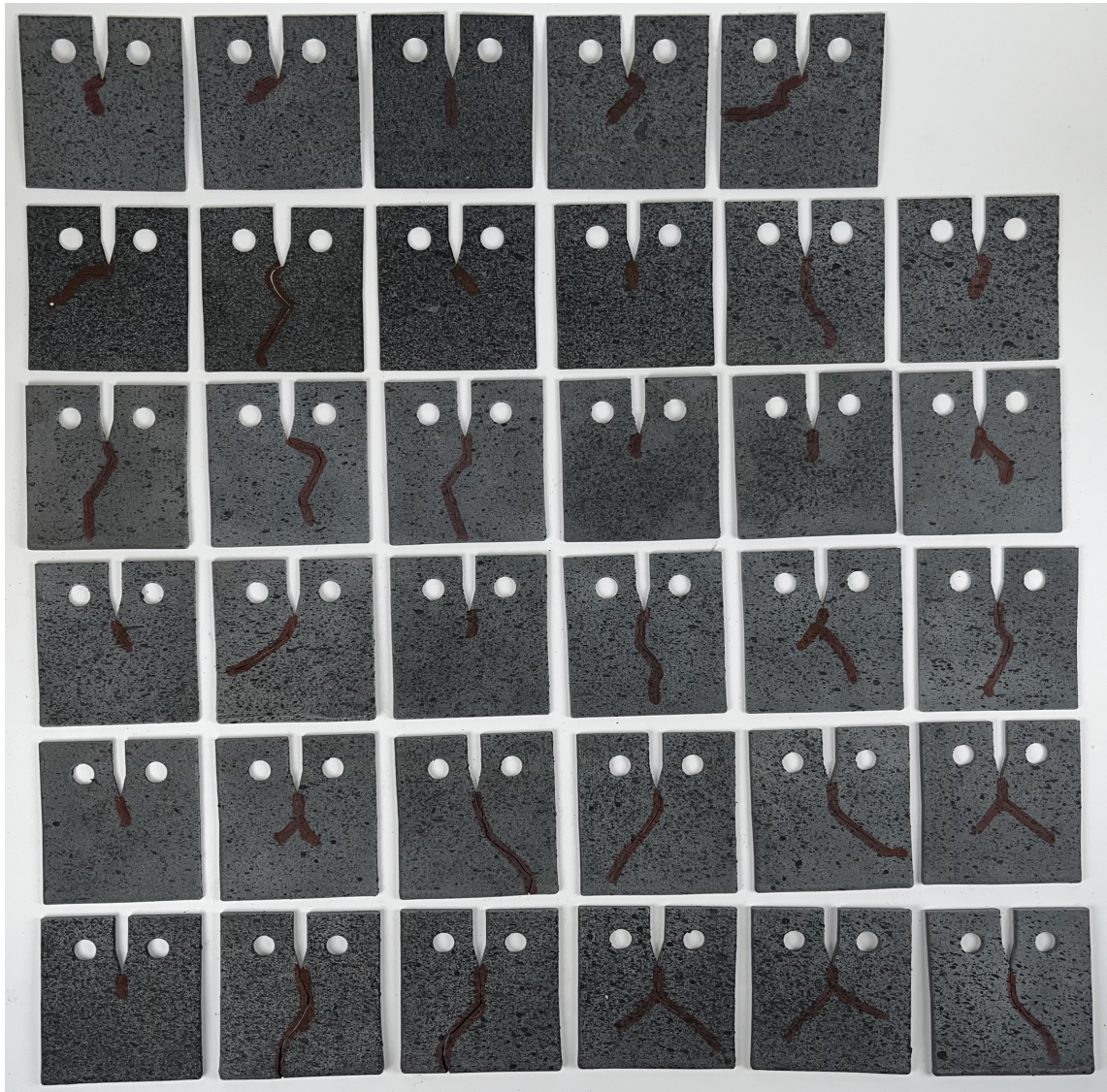

Figure 3.23: Cracks of all SAMPLE 3 for PA12 material printed in vertical direction.

The processed data are shown in Figure 3.24, where six graphs containing load diagrams for each specimens with different widths are presented. The x-axis shows distance in millimetres and the y-axis shows the load in newtons. These graphs shown relationship between the width of the specimens and the maximum load for crack formation.
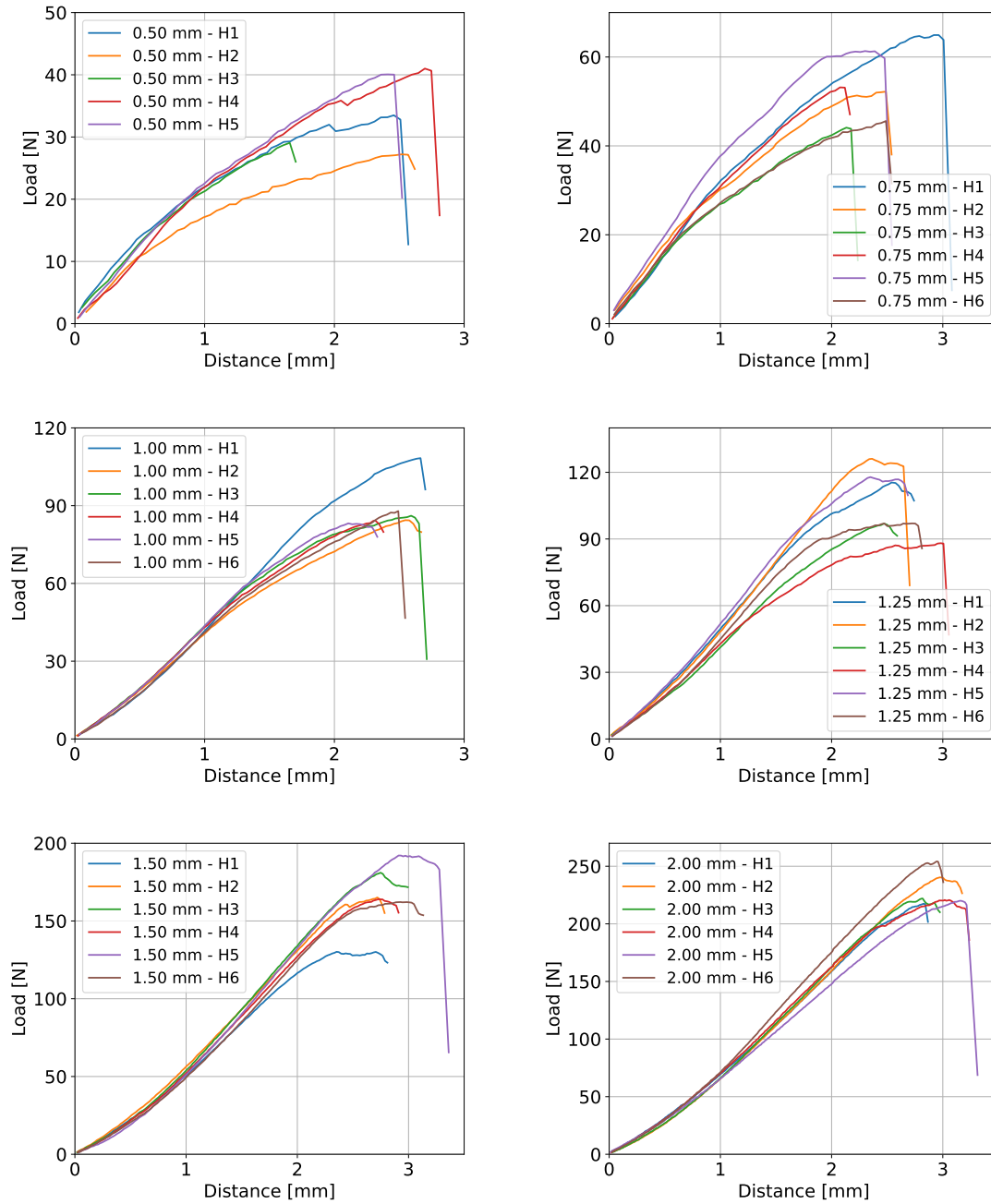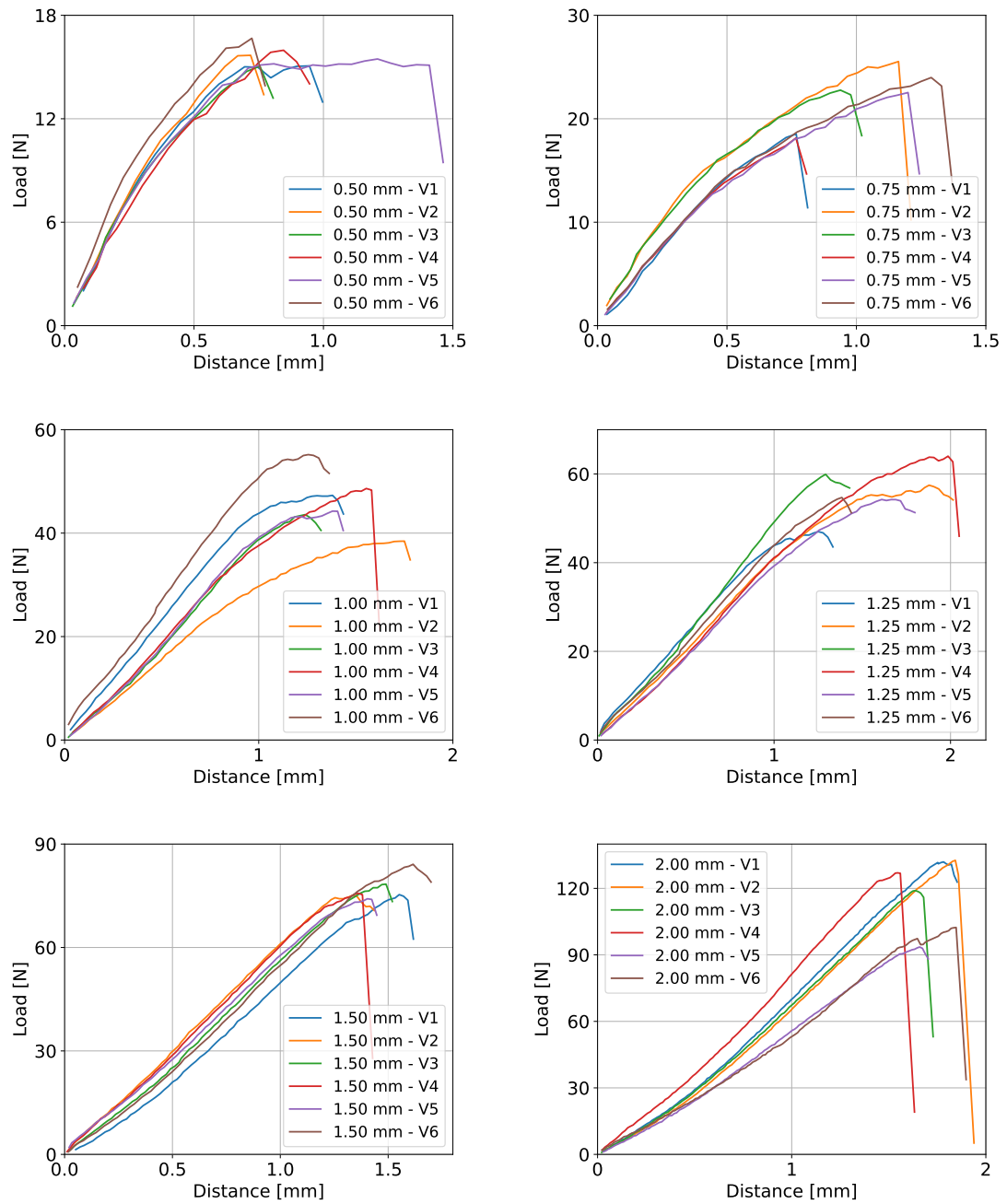
Figure 3.24: Load-distance graph for different width of SAMPLE 3 for PA12 material printed in vertical direction. The x-axis represents the press displacement, while the y-axis represents the load necessary for achieving displacement.

The values for calculating the fracture toughness of the specimens K_Q are given in Table 3.11 and Table 3.12, where a is measured the crack length, B is the measured specimen width, W is the ligament length and F_Q is the reduced maximum force. The marking with * is for samples where the crack length had to be determined by 3D DIC. Specimens marked $^+$ are samples where the crack did not occur at the beginning of the tip , but at a different location.

SAMPLE	a [mm]	B [mm]	W [mm]	F_Q [N]	K_Q [MPa$\sqrt{\text{m}}$]
V1 - 0.50$^+$	8.19	0.57	35	17.1	0.76
V2 - 0.50$^+$	9.61	0.59	35	18.05	0.86
V3 - 0.50	13.54	0.53	35	18.05	1.28
V4 - 0.50	16.87	0.57	35	18.05	1.55
V5 - 0.50$^+$	19.02	0.57	35	18.05	1.88
V6 - 0.50$^+$	8.07	0.53	35	19.0	0.89
V1 - 0.75	4.64	0.76	35	20.9	0.5
V2 - 0.75$^+$	15.45	0.72	35	27.55	1.67
V3 - 0.75	6.79	0.73	35	23.75	0.73
V4 - 0.75$^+$	8.43	0.8	35	19.95	0.64
V5 - 0.75$^+$	11.06	0.8	35	25.65	1.0
V6 - 0.75	8.09	0.67	35	24.7	0.92
V1 - 1.00	4.95	1.0	35	47.5	0.9
V2 - 1.00	7.66	0.96	35	39.9	1.0
V3 - 1.00	9.63	1.01	35	44.65	1.24
V4 - 1.00	15.41	1.01	35	44.65	1.92
V5 - 1.00	11.76	0.98	35	49.4	1.66
V6 - 1.00	5.18	1.06	35	44.65	0.82
V1 - 1.25	16.87	1.16	35	47.5	2.0
V2 - 1.25	7.67	1.22	35	57.0	1.13
V3 - 1.25	13.3	1.22	35	54.15	1.64
V4 - 1.25	6.49	1.18	35	54.15	1.0
V5 - 1.25	5.68	1.23	35	62.7	1.04
V6 - 1.25	8.23	1.18	35	55.1	1.18

Table 3.11: Values used to calculate the fracture toughness of SAMPLE 3 printed in the vertical direction with widths of 0.50 - 1.25 mm.

SAMPLE	a	B	W	F_Q	K_Q
	[mm]	[mm]	[mm]	[N]	[MPa$\sqrt{\text{m}}$]
V1 - 1.50	9.46	1.5	35	74.1	1.37
V2 - 1.50	8.53	1.48	35	74.1	1.3
V3 - 1.50	5.78	1.54	35	76.95	1.02
V4 - 1.50 *	6.47	1.49	35	75.05	1.1
V5 - 1.50	6.07	1.44	35	72.2	1.06
V6 - 1.50	8.1	1.47	35	81.7	1.39
V1 - 2.00 *	4.49	2.06	35	127.3	1.12
V2 - 2.00 *	4.2	2.01	35	128.25	1.12
V3 - 2.00 *	3.83	2.02	35	114.95	0.96
V4 - 2.00 *	4.03	2.04	35	123.5	1.04
V5 - 2.00 *	9.53	1.85	35	91.2	1.38
V6 - 2.00 *	4.5	1.94	35	98.8	0.92

Table 3.12: Values used to calculate the fracture toughness of SAMPLE 3 printed in the vertical direction with widths of 1.50 and 2.00 mm.

A summary of the fracture toughness results for SAMPLE 3 printed in vertical direction are given by Table 3.13.

B [mm]	V1	V2	V3	V4	V5	V6
0.50	0.76[+]	0.86[+]	1.28	1.55	1.88[+]	0.89[+]
0.75	0.5	1.67[+]	0.73	0.64[+]	1.0[+]	0.92
1.00	0.9	1.0	1.24	1.92	1.66	0.82
1.25	2.0	1.13	1.64	1.0	1.04	1.18
1.50	1.37	1.3	1.02	1.1*	1.06	1.39
2.00	1.12*	1.12*	0.96*	1.04*	1.38*	0.92*

Table 3.13: Experiment results of K_Q for SAMPLE 3 printed in vertical direction.

3.4.3 Summary of results and overview of crack propagation

The results of the fracture toughness from the experiment calculated in Section 3.4.1 and Section 3.4.2 for each specimen, its width and print direction are summarized in Table 3.14. As expected, the thinner samples showed large differences and deviations. This is particularly evident for samples printed in the horizontal direction. For the thicker specimens, the fracture toughness values became consistent and naturally increased with specimen thickness. The values for the vertical printed direction are mostly the same for each sample width, but thinner samples showed higher error rates than thicker ones.

B [mm]	SAMPLE 2		SAMPLE 3	
	H	V	H	V
0.50	2.0 ± 0.6	0.99 ± 0.37	1.54 ± 0.22	1.2 ± 0.41
0.75	2.64 ± 1.12	0.91 ± 0.38	1.33 ± 0.48	0.72 ± 0.11
1.00	1.65 ± 0.23	0.93 ± 0.11	1.5 ± 0.15	1.3 ± 0.42
1.25	1.87 ± 0.09	1.35 ± 0.35	1.73 ± 0.38	1.03 ± 0.06
1.50	2.16 ± 0.45	0.94 ± 0.07	2.01 ± 0.33	1.21 ± 0.15
2.00	2.37 ± 0.31	1.09 ± 0.15	2.2 ± 0.36	1.09 ± 0.15

Table 3.14: Summary of experiment results of K_Q for PA12 material printed in horizontal and vertical directions with their deviation of results.

For these values, I made graphs shown in Figure 3.25, which clearly show that the fracture toughness values for horizontal printed specimens begin to stabilize from s width 1.00 mm and increase with specimen width. For vertical specimens, the value does not change much and is around 1.00 MPa$\sqrt{\text{m}}$.
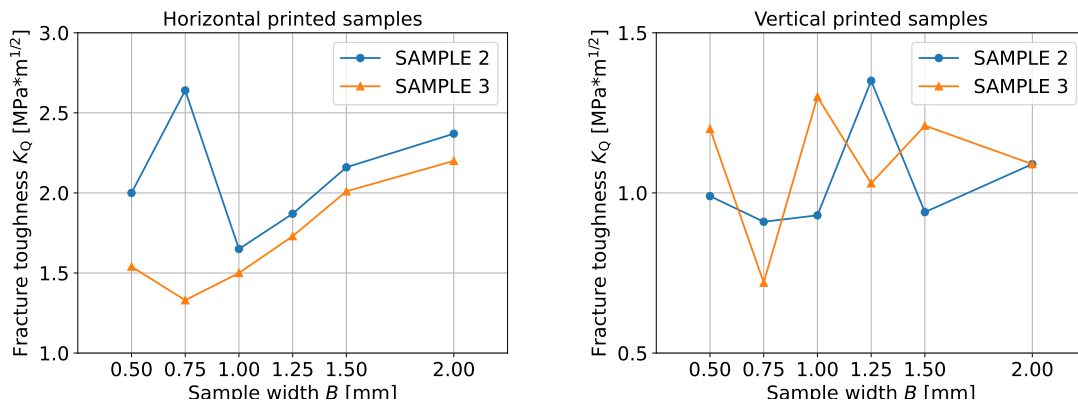

Figure 3.25: Graphs with fracture toughness values for individual specimens printed in horizontal and vertical direction.

The experimental data were processed in a Python script in PyCharm editor, which is greatly accelerated the data processing. The amount of measured data in the

.csv file for pre-test 96 files and for following experiment 140 files. This adds up to 236 files, which would have been very difficult to process without the script. The script was written primarily to produce good quality graphs and calculate fracture toughness values.

In the experiment, 8 types of crack propagation were found for different print orientations, which is shown in Figure 3.26. Samples with vertical print orientation have mostly straight crack propagation parallel to the printed layers. The ideal type of crack propagation for vertical printed samples were type 1, where the crack length could be easily measured. Thicker specimens were often destroyed by entire length crack propagation of the specimen (type 2) and for thinner specimens the problem was that the crack did not propagate at the tip (type 3). Samples with horizontal print orientation had a crack propagation type 4-8. The crack was influenced by the direction of the printed layers, which controlled the direction of crack propagation.
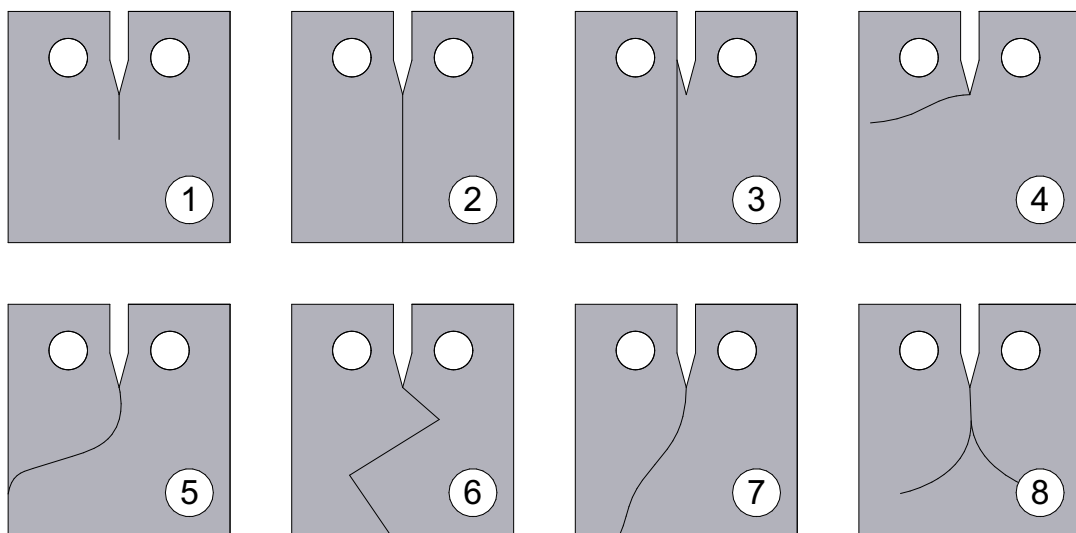
Figure 3.26: Crack propagation, where type 1-3 were found for samples printed in the vertical direction and type 4-8 were found for samples printed in the horizontal direction.

For two selected samples with a crack propagation across the entire sample for both print orientations, I used a microscope to examine the crack. I was trying to determine if the crack was propagating in the joints between the dust particles, or if the crack was dividing the laser melted dust particles. Figure 3.27 shows the close-up view of the crack in horizontally printed samples, where can be said propagate at the joints between particles. Figure 3.28 shows same propagation for samples printed in the vertical printing orientation. However, the zoom of microscope was not sufficient, so it was not possible to determine exactly whether the crack propagates in the joints between particles or thought the particles. A more detail and better microscope, such as SEM technology, should be used to investigate this issue in more detail.
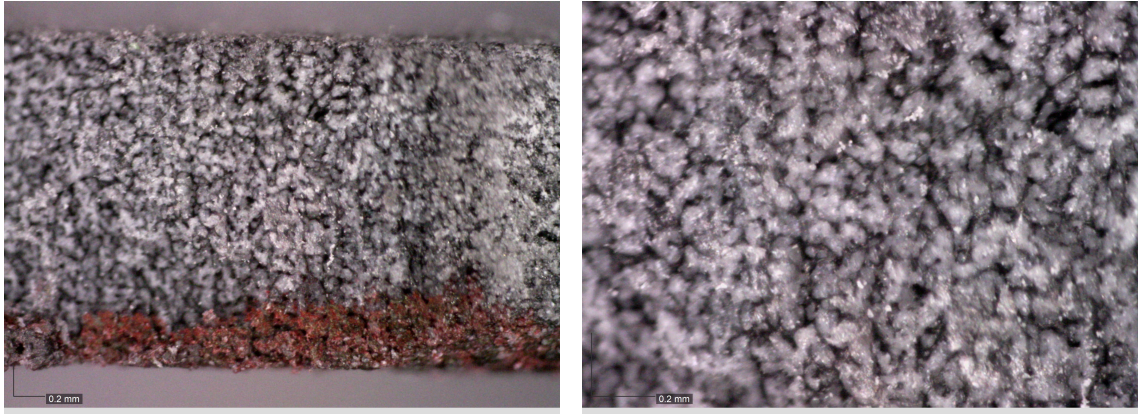
Figure 3.27: A detail view of the images for the sample with horizontal print orientation. Images are taken below the tip where the crack formation and initiation of propagate occurred.
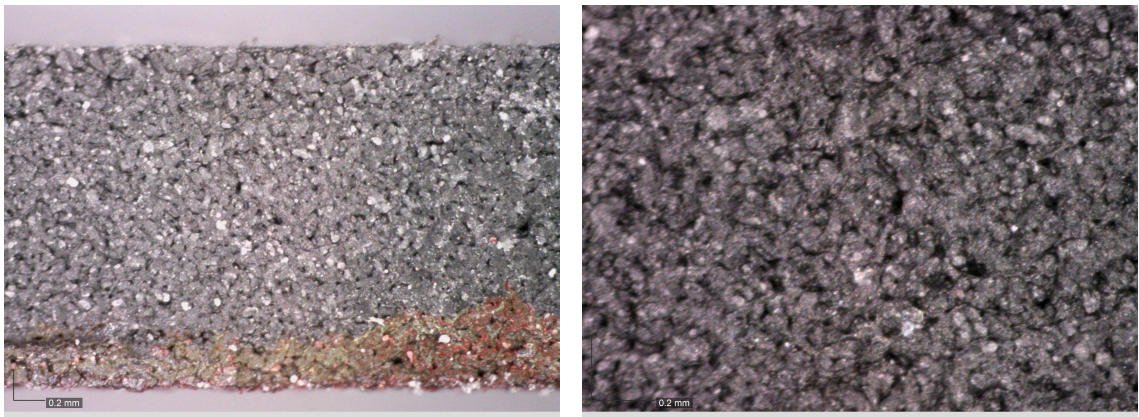
Figure 3.28: A detail view of the images for the sample with vertical print orientation. Images are taken below the tip where the crack formation and initiation of propagate occurred.

Figure 3.29 and Figure 3.30 show the monitoring of crack propagation using 3D DIC. To demonstrate crack propagation, I prepared one example for SAMPLE 2 printed in vertical and horizontal directions. I have shown the crack propagation with logarithmic principal strain, where the first image shows the beginning of crack formation, the second image shows the maximal principal strain, and the last image shows the strain before the specimen is completely destroyed or before the load stops. I used frequency of 2 images per 1 second, which meant taking approximately 70-80 frames for one sample. A finer frequency could been used to the capture the crack propagation more accurately and take more images, but for my experiment this number of images was sufficient.
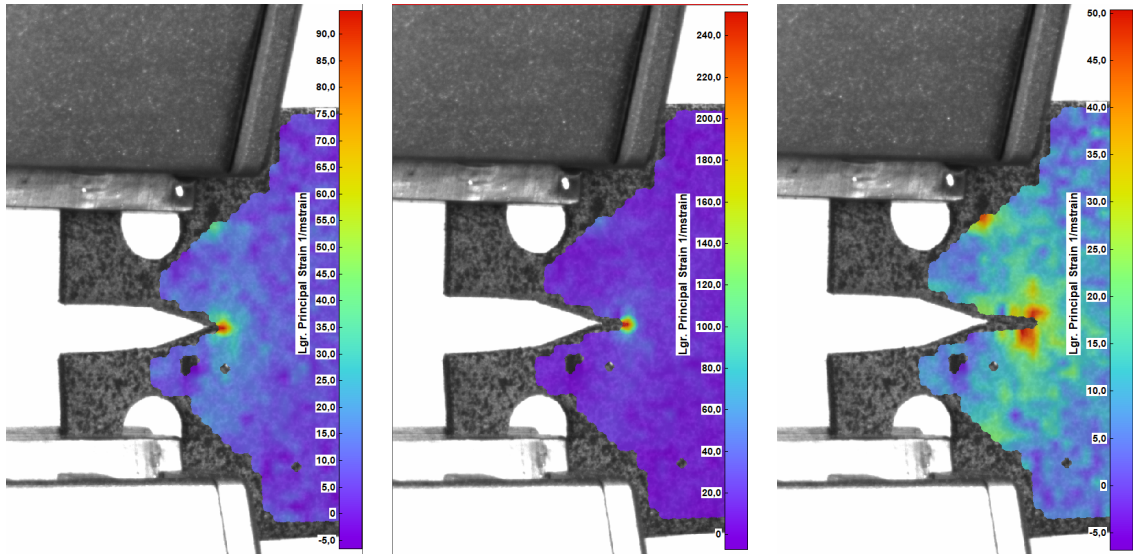
Figure 3.29: DIC results of principal strain for SAMPLE 2 printed in horizontal orientation. The first image is the beginning of the crack propagation, the second is the maximum strain during loading and the last image is the strain before complete destroy of specimen.

Figure 3.30: DIC results of principal strain for SAMPLE 2 printed in vertical orientation. The first image is the beginning of the crack propagation, the second is the maximum strain during loading and the last image is the strain before complete destroy of specimen.

3.4.4 Nonlinear analysis

This section describes numerical nonlinear analysis. I used Atena software, which deals with the nonlinear analysis of concrete. Atena has 4 types of analyses (Static, Creep, Transport and Dynamic) and Static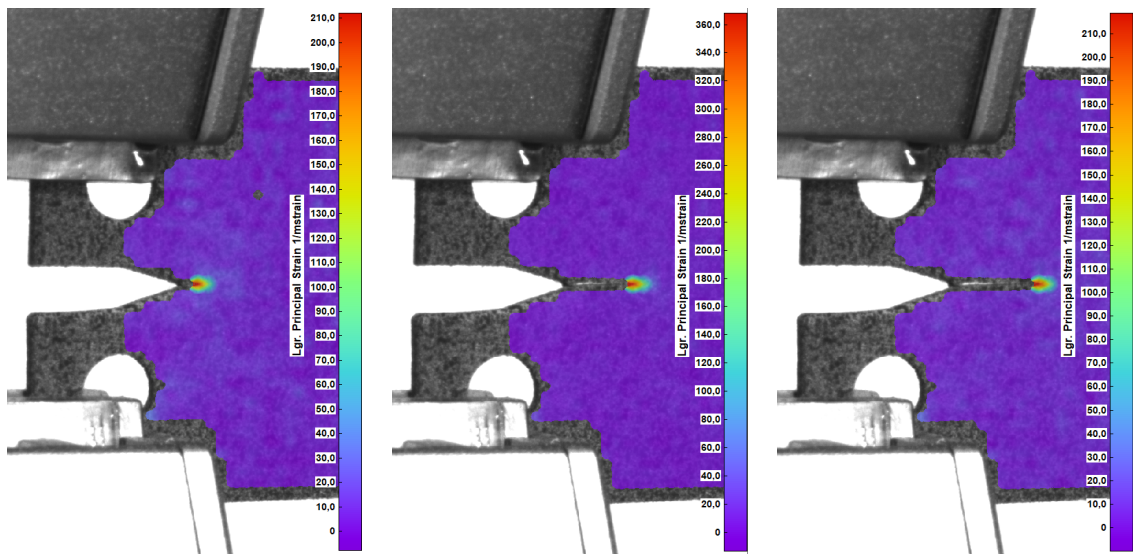 was used to simulate my experiment. The calculation procedure started by determining the mechanical properties to define the PA12 material in the software. Then, I modeled 3 samples with different width (0.50 mm, 1.25 mm, 2.00 mm) in GiD 16.0.6 and set the boundary condition for the calculation. After the calculation, the result were postprocessed in Atena 2023.

Since there are no strictly given mechanical properties for polyamide material, I had to use parameters from others experiments. I specially searched for data from CT experiments because it is the same type of experiment as mine. Sinterit provides technical data sheets where the Young's modulus is 1.47 GPa and tension strength is 32 MPa [68]. Experiments examining the Poisson's ration have similar values, which are around 0.37-0.43 [64, 69, 70, 71]. An experiment by Lammens and colleagues showed that the compression strength of PA12 materials is around 60-62 MPa [69]. The compression strength from Schneider and Kumar's experiment showed a value of about 62 MPa [64]. Another important property for nonlinear analysis is the fracture energy, whose value according to experiments is around 6.2-7 kN/m [71, 72]. A summary of these values is given in Table 3.15.

Material properties	PA12 material
Young's modulus E [GPa]	1.47
Poisson's Ratio μ [-]	0.4
Density ρ [kg/m^3]	1010
Thermal expansion α [kg/m^3]	$10^{(-12)}$
Tension Strength f_t [MPa]	32
Compression strength f_c [MPa]	62
Fracture Energy G_f [N/m]	7000

Table 3.15: Material properties for nonlinear analysis of PA12

I modeled the sample geometry as solid elements with hexahedral mesh. The load bars are also meshed by a hexahedral mesh using semi-structured mesh. The area of the most interest for crack formation below the tip has the smallest elements of 0.25x0.25 mm. A single solid element of 0.25 mm width was modeled below the tip to assist the software to propagate a crack and subsequently plot the crack propagation. To reduce the size of elements I used the 'Concentrate elements' function, which is used to change the size of elements along the length of the solid. A detailed view of this area is shown in Figure 3.31. I tried to minimize fixed contacts, so I modeled the sample geometry as a whole, since the fixed contacts affect the complexity and computation time. Fixed contact were used to connect loading bars to the sample. The load bars were divide into two volumes in their middle. The line in the middle of

bar was also divided to create a points in the middle of the load bar with a circular shape. At these points all the condition to calculating are defined.
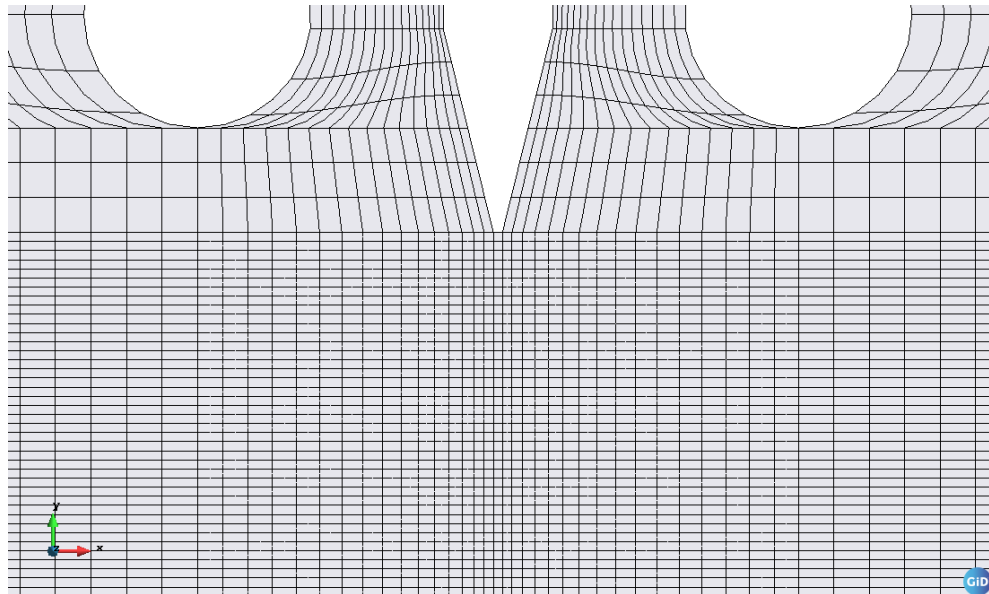
Figure 3.31: Detail view of the mesh under the tip to form the crack. The sample is meshed with hexahedrals.

The material properties of PA12 material are described in Table 3.15 and have been set to the region of interest for the sample geometry. The other area of sample were set up to an elastic material with Young's module, Poisson's Ratio and density identical to the PA12 material. The elastic material was chosen to investigate the crack mainly below the tip and thus eliminate cracks in the loading region. For the load bars, an elastic material with Young's module $E = 31$ GPa was set. This solid had function only for loading sample, so it is not necessary to deal with this material in more detail. Figure 3.32 shown the determination of the material for individual solids.

Figure 3.32: Material definitions for each solids.

Figure 3.33 shows the boundary condition for my calculation. In the middle of the load bar is supports at a points, with the left load bar has support in x and y axis direction and the right load bar has support only in the y axis. On the right bar, the load condition is the displacement at the point, which is set to 4 mm. On the lines with these boundary conditions, a maxmonitor is set to monitor the reaction (force) in support in the x-axis support and the displacement in the x-axis direction, which is the main interest to produce a Load-Distance graphs as and output from the calculation. For the connection of the load bars and sample, a fixed 'Master-Slave' contact was set up, with master contact set on sample and slave contact set on load bar.
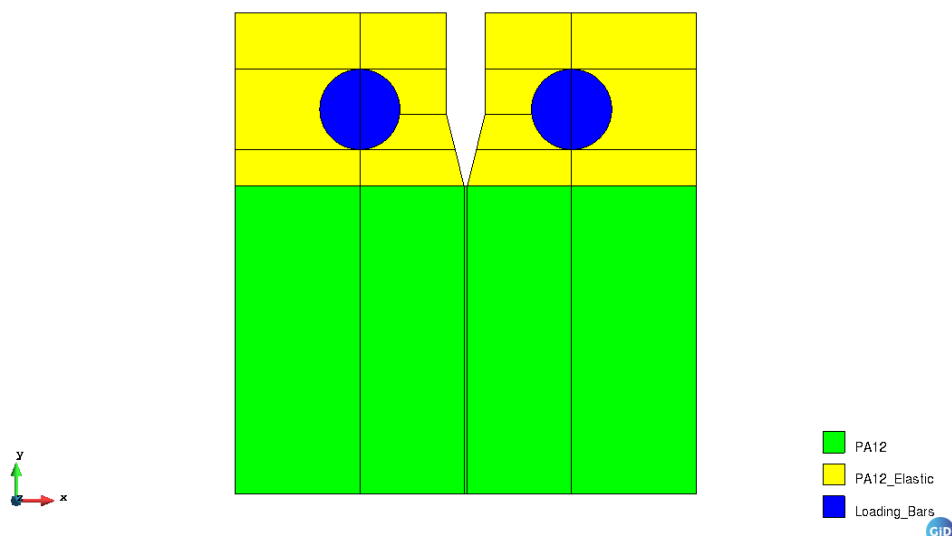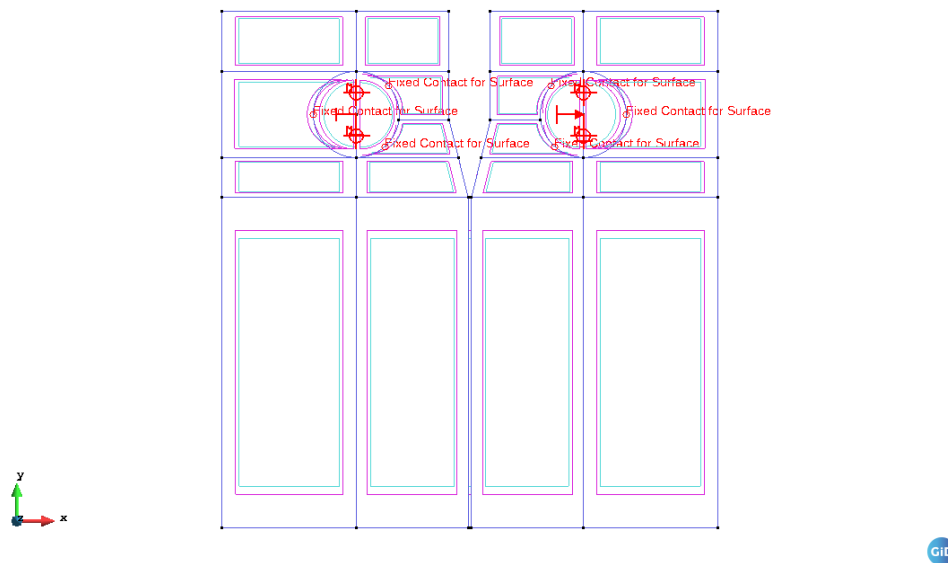

Figure 3.33: Boundary condition for calculation.

In my case, I used displacement for the loading in my experiment, where I loaded the specimens at 4 mm/min, so I used 4 mm displacement in the numerical model for loading. The solution parameter was Newton-Raphson iteration methods, which is a great choice for nonlinear analysis with displacement loading. First, I set up a mesh as normal, meaning that the nodes were only at the vertices of the hexagons. This calculation had about 30000 nodes and the calculation was completed in under 2 hour with 60 iteration steps. I then set the mesh criteria to a quadratic, which added nodes in the middle of hexgones lines, so the number of nodes for a single element increased from 8 to 20, bringing total number of nodes to about 140 thousand. This greatly affected the computation time and one calculation took about 16-18 hours. Figures 3.34 to Figure 3.39 show the calculation results for each samples. The load-displacements graphs and the crack length at the peak load are shown.

Figure 3.34: Results of the nonlinear analysis for SAMPLE 2 - 0.50 mm. Load-distance diagram on the left, the crack width and crack propagation on right, both calculated by Atena 2023 software.
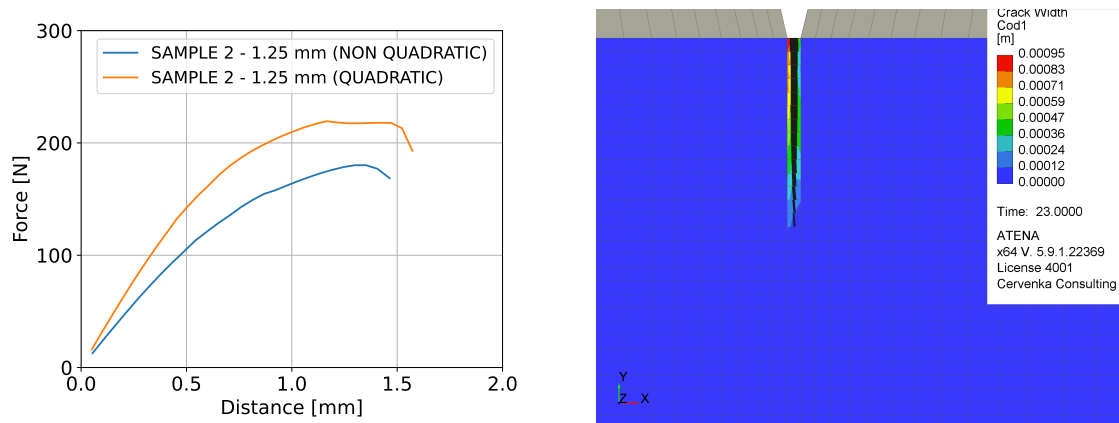
Figure 3.35: Results of the nonlinear analysis for SAMPLE 2 - 1.25 mm. Load-distance diagram on the left, the crack width and crack propagation on right, both calculated by Atena 2023 software.
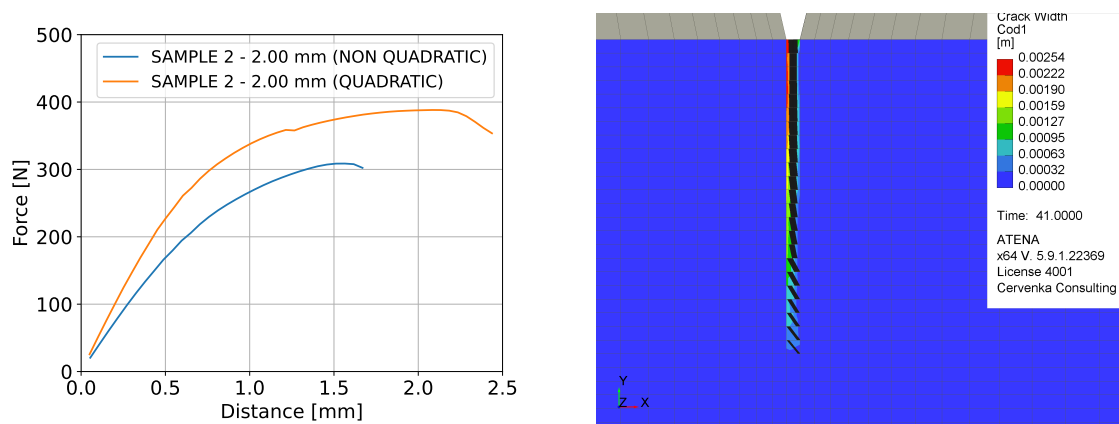
Figure 3.36: Results of the nonlinear analysis for SAMPLE 2 - 2.00 mm. Load-distance diagram on the left, the crack width and crack propagation on right, both calculated by Atena 2023 software.

Figure 3.37: Results of nonlinear analysis for SAMPLE 3 - 0.50 mm. Load-distance diagram on the left, the crack width and crack propagation on right, both calculated by Atena 2023 software.

Figure 3.38: Results of nonlinear analysis for SAMPLE 3 - 1.25 mm. Load-distance diagram on the left, the crack width and crack propagation on right, both calculated by Atena 2023 software.

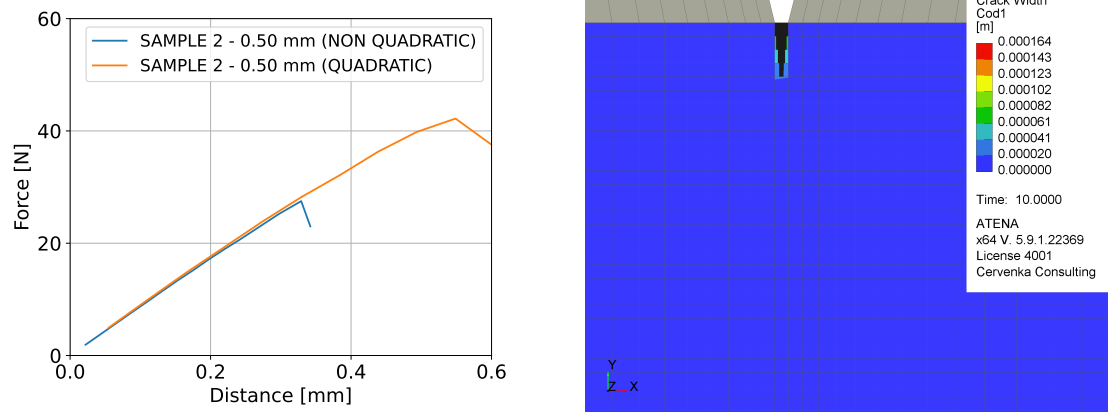**Figure 3.39:** Results of nonlinear analysis for SAMPLE 3 - 2.00 mm. Load-distance diagram on the left, the crack width and crack propagation on right, both calculated by Atena 2023 software.
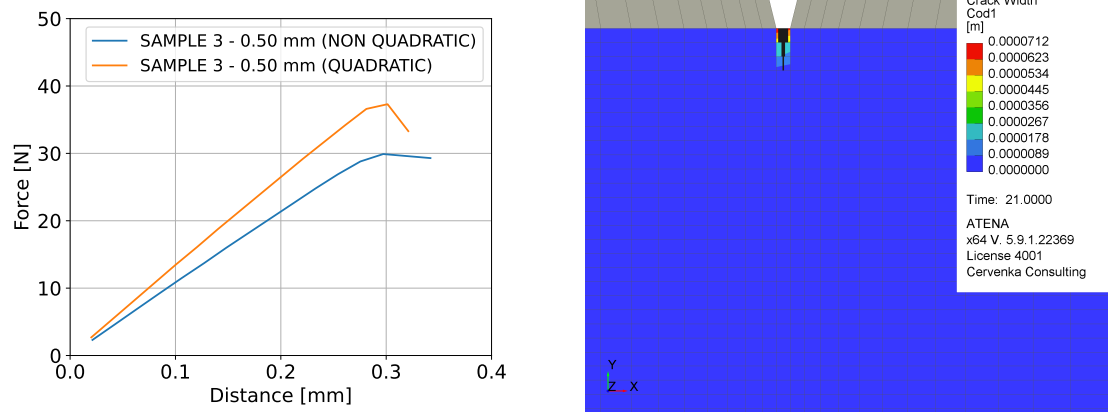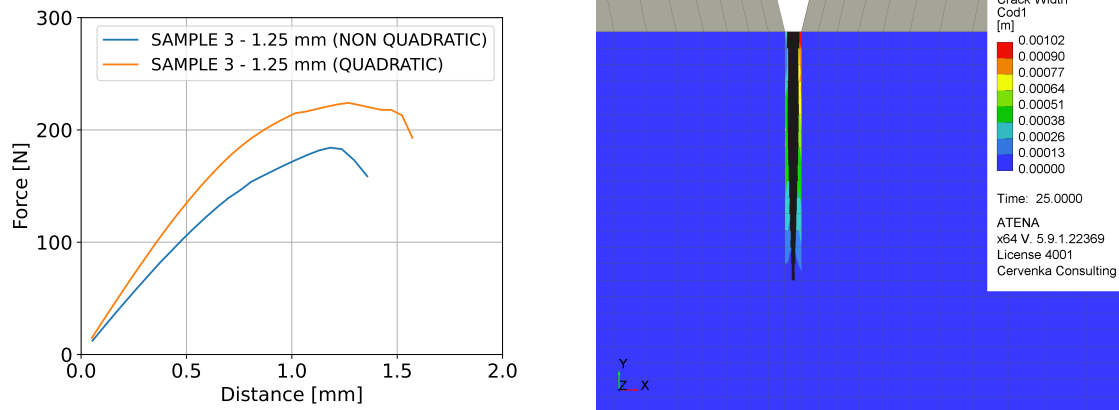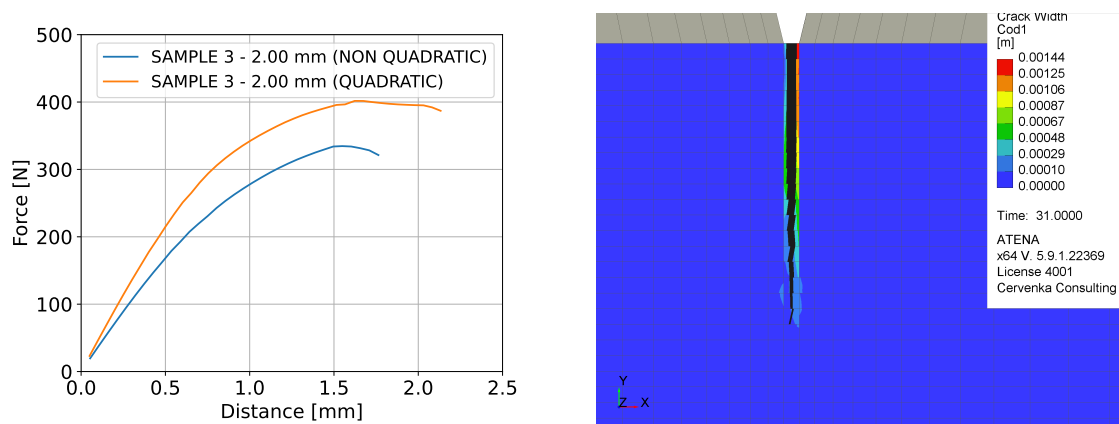
Conclusion

I performed a fracture toughness experiment on thin samples made by additive manufacture. Since this is a pilot study to test fracture toughness of very thin samples used in bioapplication, PA12 polyamide material was chosen instead of metallic material (titanium alloys), which is much cheaper and easier to produce. I designed the experiment and samples selection according to EN ISO 12737, which is norm for testing metallic material.

The main objective of this work was to set up an experiment and evaluation the fracture toughness results of very thin samples. I designed 4 types of geometries with 6 different widths (0.50, 0.75, 1.00, 1.25, 1.50 and 2.00 mm), printed the samples using SLS 3D printing technology and performed a pre-test for 96 samples in total. After evaluation of the samples, 2 types (SAMPLE 2 and SAMPLE 3) were selected as the best geometries for further experiment. Another idea was to observe the crack propagation of samples in different printing direction, where horizontal printing direction means that layers were printed perpendicular to the expected crack propagation and for vertical printing direction, the layers were printed parallel to the expected crack propagation.

The experiment continued by testing SAMPLE 2 and SAMPLE 3 with different print orientation. A total of 140 samples were tested (69 in horizontal print direction and 71 in vertical print direction). The experiment was complemented with 3D DIC technology, which is excellent tool for detailed monitoring the crack propagation. In many cases, DIC helped me to determine the crack length for calculation of fracture toughness. Because in cases where the specimens had ruptured along their entire length, the crack length had to be determined using DIC. This consisted of finding the image just before the full destroy and then reading the crack length on that image. This length was then used to calculate the fracture toughness of that specimen.

The horizontally printed samples showed consistent results and values from a certain width and the fracture toughness increase as would be expect. Printed samples with width of 0.50 and 0.75 mm showed very inconsistent results and their values varied considerably. Vertical printed samples showed no increase in values and all values were around 1.00 MPa$\sqrt{\text{m}}$. However, thicker samples had lower error rate and more similar results than the thinner samples.

I simulated my experiment by nonlinear analysis, so I created a numerical model in GiD 16.0.6 and calculated it using Atena software. Currently, the PA12 material does not have strictly defined mechanical properties, so I had to choose the values from other experiments. For the selected thicknesses (0.50 mm as the thinner width, 1.25 mm as the middle width and 2.00 mm as the thicker width) I created a numerical model for both samples geometries, in total i had 6 different models. For these 6 models I used a linear (non quadratic) and quadratic mesh for the calculation. A comparison of values for selected sample (vertically printed sample) from the experiment and the calculation are shown in Figure 3.40.
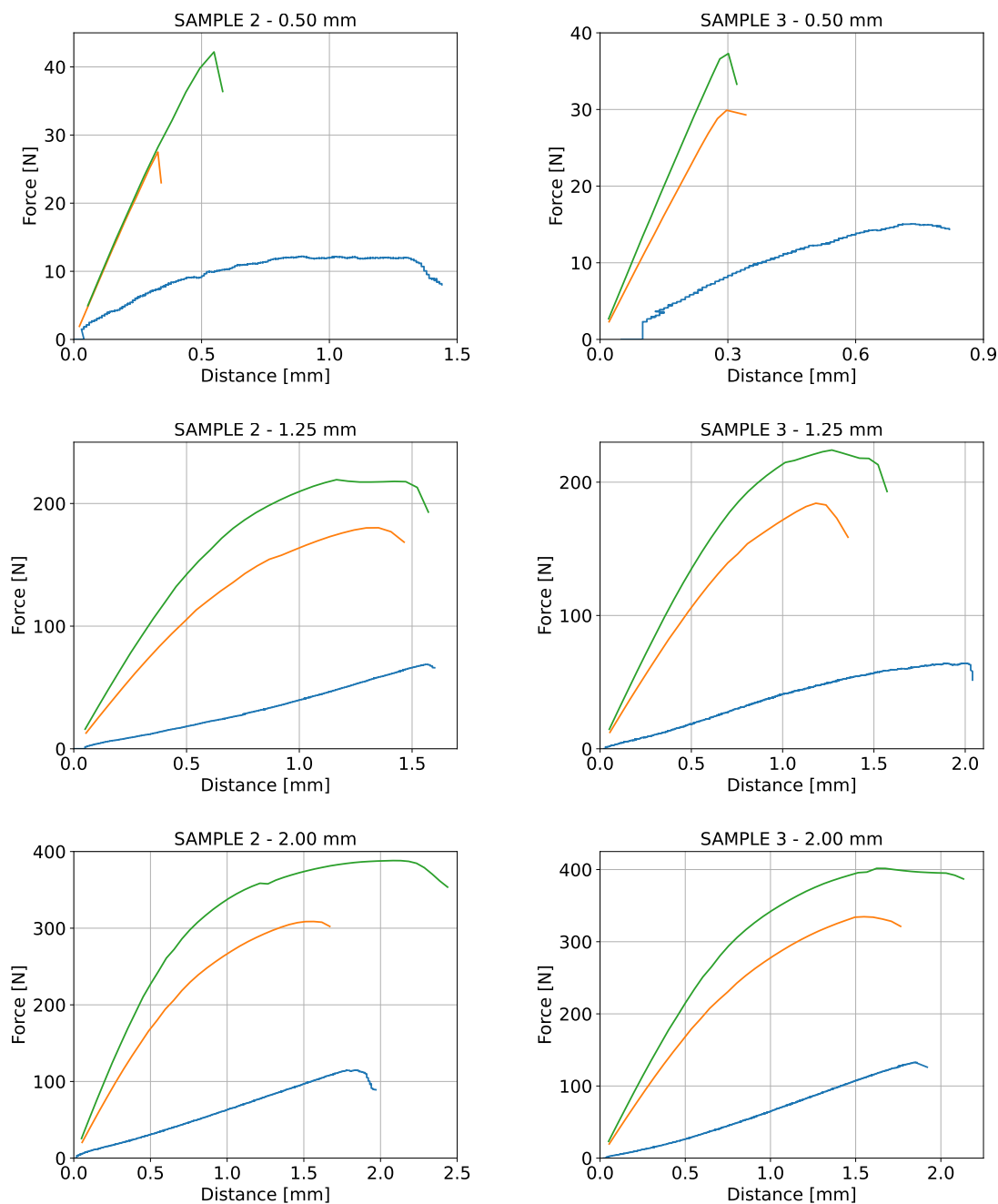

Figure 3.40: Load-displacement graphs for one selected sample from the experiment and 2 types numerical models, where the orange line is the numerical model with linear elements, the green line is the numerical model with quadratic elements and the blue line is the experimental data.

As expected, the numerical models did not fit the experimental data. This is mainly due to the imperfect material numerical model for materials produced by additive technologies, which is the main concern of GAČR project No. 23-04971S. However, can seen a trend where samples with increasing width approach the values from the numerical model to those from the experiments.

The large differences in the experiment results are due to the imperfections of 3D printing and sample preparation procedure after printing. The problem with printing is that the technology is not yet good enough for the individual powder beads on the surface of the sample to melt together sufficiently. These powder beads can then "fall off" when the sample is handled, which weakens the thickness of the sample. This aspect is then fatal for very thin samples. Furthermore, after printing I cleaned the samples with a fine abrasive, this cleaning procedure can cause further loss of powder beads on the sample surface. The roughness and the large differences in thicknesses on the sample surface were examined on a confocal microscope and are shown in Figure 3.41.
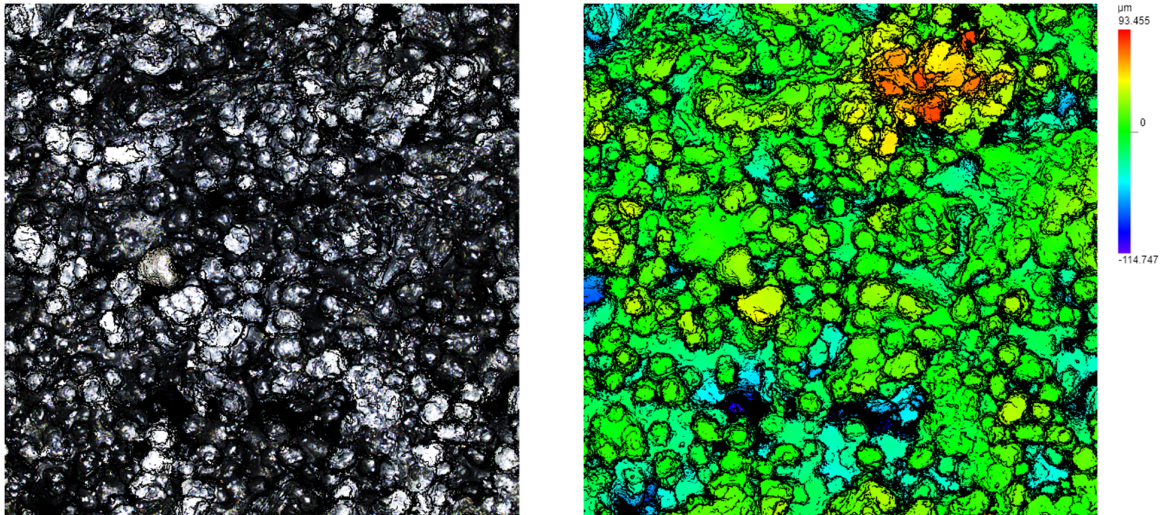
Figure 3.41: Images taken with a confocal microscope showing surface irregularities and roughness.

From my knowledge gained from these thesis, I would recommend this procedure for experiments on metals. However, for further experiments I would recommend increasing the frame rate of the 3D DIC measurements, going from 2 frames to say 5 frames per second, for a more detailed view of crack propagation. For the 3D DIC I would also use the fracture toughness calculation module, which was only released by Dantec Dynamic in December 2023, so it could not be used in my thesis. I would also recommend looking more into the microstructure of specimens and use technologies that can do this (e.g. SEM technology).

Bibliography

1. TAKEDA, Osamu; OUCHI, Takanari; OKABE, Toru H. Recent progress in titanium extraction and recycling. *Metallurgical and Materials Transactions B.* 2020, roč. 51, č. 4, pp. 1315–1328.

2. OOSTHUIZEN, SJ. Titanium: the innovators' metal-Historical case studies tracing titanium process and product innovation. *Journal of the Southern African Institute of Mining and Metallurgy.* 2011, roč. 111, č. 11, pp. 781–786.

3. ZYKOVA, Marina; VORONINA, Elena; CHEPURNOV, Alexander; RYMKE-VICH, Dmitry; TANKEEV, Aleksey; VLASOV, Sergey; CHUB, Alexander; AVETISSOV, Igor. Role of Magnesium in Ultra-Low-Radioactive Titanium Production for Future Direct Dark Matter Search Detectors. *Materials.* 2022, roč. 15, č. 24, p. 8872.

4. YUMAK, Nihal; ASLANTAŞ, Kubilay. A review on heat treatment efficiency in metastable β titanium alloys: the role of treatment process and parameters. *Journal of materials research and technology.* 2020, roč. 9, č. 6, pp. 15360–15380.

5. LIN, Cheng; YIN, Guili; ZHAO, Yongqing; WANG, Jianzhong. Analysis of the effect of alloy elements on allotropic transformation in titanium alloys with the use of cohesive energy. *Computational Materials Science.* 2016, roč. 111, pp. 41–46.

6. VEIGA, Celestino; DAVIM, J Paulo; LOUREIRO, AJR. Properties and applications of titanium alloys: a brief review. *Rev. Adv. Mater. Sci.* 2012, roč. 32, č. 2, pp. 133–148.

7. MANIVASAGAM, Vignesh K; SABINO, Roberta M; KANTAM, Prem; POPAT, Ketul C. Surface modification strategies to improve titanium hemocompatibility: A comprehensive review. *Materials Advances.* 2021, roč. 2, č. 18, pp. 5824–5842.

8. BANERJEE, Dipankar; WILLIAMS, JC. Perspectives on titanium science and technology. *Acta Materialia.* 2013, roč. 61, č. 3, pp. 844–879.

9. LIU, Xuanyong; CHU, Paul K; DING, Chuanxian. Surface modification of titanium, titanium alloys, and related materials for biomedical applications. *Materials Science and Engineering: R: Reports.* 2004, roč. 47, č. 3-4, pp. 49–121.

10. GOBBI, Silvio. Requirements for Selection/Development of a Biomaterial. *Biomedical Journal of Scientific & Technical Research.* 2019, roč. 14.

11. JIMENEZ-MARCOS, Cristina; MIRZA-ROSCA, Julia Claudia; BALTATU, Madalina Simona; VIZUREANU, Petrica. Experimental research on new developed titanium alloys for biomedical applications. *Bioengineering.* 2022, roč. 9, č. 11, p. 686.

12. CHEN, Liang-Yu; CUI, Yu-Wei; ZHANG, Lai-Chang. Recent development in beta titanium alloys for biomedical applications. *Metals.* 2020, roč. 10, č. 9, p. 1139.

13. GEPREEL, Mohamed Abdel-Hady; NIINOMI, Mitsuo. Biocompatibility of Ti-alloys for long-term implantation. *Journal of the mechanical behavior of biomedical materials.* 2013, roč. 20, pp. 407–415.

14. RANDHAWA, Kawaljit Singh; PATEL, Ashwin D. A review on tribo-mechanical properties of micro-and nanoparticulate-filled nylon composites. *Journal of Polymer Engineering.* 2021, roč. 41, č. 5, pp. 339–355.

15. SHAKIBA, Mohamadreza; REZVANI GHOMI, Erfan; KHOSRAVI, Fatemeh; JOUYBAR, Shirzad; BIGHAM, Ashkan; ZARE, Mina; ABDOUSS, Majid; MOAREF, Roxana; RAMAKRISHNA, Seeram. Nylon—A material introduction and overview for biomedical applications. *Polymers for advanced technologies.* 2021, roč. 32, č. 9, pp. 3368–3383.

16. KAMAL, Tahseen; PARK, Soo-Young; PARK, Jung-Hyun; CHANG, Young-Wook. Structural evolution of poly (ether-b-amide12) elastomers during the uniaxial stretching: An in situ wide-angle X-ray scattering study. *Macromolecular Research.* 2012, roč. 20, pp. 725–731.

17. DAI, Ruixin; HUANG, Miaoming; MA, Lili; LIU, Wentao; HE, Suqin; LIU, Hao; ZHU, Chengshen; WANG, Yujie; ZHANG, Zhenya; SUN, Aihua. Study on crystal structure and phase transitions of polyamide 12 via wide-angle X-ray diffraction with variable temperature. *Advanced Composites and Hybrid Materials.* 2020, roč. 3, pp. 522–529.

18. MA, Ning; LIU, Wentao; MA, Lili; HE, Suqin; LIU, Hao; ZHANG, Zhenya; SUN, Aihua; HUANG, Miaoming; ZHU, Chengshen. Crystal transition and thermal behavior of Nylon 12. *e-Polymers.* 2020, roč. 20, č. 1, pp. 346–352.

19. VARGHESE, Maria; GRINSTAFF, Mark W. Beyond nylon 6: polyamides via ring opening polymerization of designer lactam monomers for biomedical applications. *Chemical Society Reviews.* 2022.

20. RG, Asuwin Prabu; BAJAJ, Gauri; JOHN, Amy Elsa; CHANDRAN, Sharan; KUMAR, Vishnu Vijay; RAMAKRISHNA, Seeram. A review on the recent applications of synthetic biopolymers in 3D printing for biomedical applications. *Journal of Materials Science: Materials in Medicine.* 2023, roč. 34, č. 12, p. 62.

21. ØDEGAARD, Kristin S; TORGERSEN, Jan; ELVERUM, Christer W. Structural and biomedical properties of common additively manufactured biomaterials: A concise review. *Metals.* 2020, roč. 10, č. 12, p. 1677.

22. VYAVAHARE, Swapnil; MAHESH, Vinyas; MAHESH, Vishwas; HARURSAMPATH, Dineshkumar. Additively manufactured meta-biomaterials: A state-of-the-art review. *Composite Structures.* 2023, roč. 305, p. 116491.

23. NGO, Tuan D; KASHANI, Alireza; IMBALZANO, Gabriele; NGUYEN, Kate TQ; HUI, David. Additive manufacturing (3D printing): A review of materials, methods, applications and challenges. *Composites Part B: Engineering.* 2018, roč. 143, pp. 172–196.

24. WANG, Xin; JIANG, Man; ZHOU, Zuowan; GOU, Jihua; HUI, David. 3D printing of polymer matrix composites: A review and prospective. *Composites Part B: Engineering.* 2017, roč. 110, pp. 442–458.

25. GROSSIN, David; MONTÓN, Alejandro; NAVARRETE-SEGADO, Pedro; ÖZMEN, Eren; URRUTH, Giovanni; MAURY, Francis; MAURY, Delphine; FRANCES, Christine; TOURBIN, Mallorie; LENORMAND, Pascal et al. A review of additive manufacturing of ceramics by powder bed selective laser processing (sintering/melting): Calcium phosphate, silicon carbide, zirconia, alumina, and their composites. *Open Ceramics.* 2021, roč. 5, p. 100073.

26. LADANI, Leila; SADEGHILARIDJANI, Maryam. Review of powder bed fusion additive manufacturing for metals. *Metals.* 2021, roč. 11, č. 9, p. 1391.

27. CHATHAM, Camden A; LONG, Timothy E; WILLIAMS, Christopher B. A review of the process physics and material screening methods for polymer powder bed fusion additive manufacturing. *Progress in Polymer Science.* 2019, roč. 93, pp. 68–95.

28. ASHRAF, Mahmud; GIBSON, Ian; RASHED, M Golam. Challenges and prospects of 3D printing in structural engineering. In: *Proceedings of the 13th International Conference on Steel, Space and Composite Structures, Perth, WA, Australia.* 2018, sv. 11.

29. KIM, Huhn; JEONG, Seongwon. Case study: Hybrid model for the customized wrist orthosis using 3D printing. *Journal of Mechanical Science and Technology.* 2025, roč. 12, č. 29, pp. 5151–5156.

30. JÍRA, A.; ŠEJNOHA, M.; KREJČÍ, T.; VOREL, J.; ŘEHOUNEK, L.; MARSEGLIA, G. Mechanical properties of porous structures for dental implants: experimental study and computational homogenization. *Materials.* 2021, roč. -, č. -, pp. 1–25. V recezním řízení (08/2021).

31. BOBYN, J. D.; PILLIAR, R. M.; CAMERON, H. U.; WEATHERLY, G. C. The Optimum Pore Size for the Fixation of Porous-Surfaced Metal Implants by the Ingrowth of Bone. *Clinical Orthopaedics and Related Research.* 1980, roč. 150, č. -, pp. 263–270.

32. FROSCH, Karl-Heinz; BARVENCIK, Florian; VIERECK, Volker; LOHMANN Christoph, H; DRESING, Klaus; BREME, Jürgen; BRUNNER, Edgar; STÜRMER Klaus, Michael. Growth Behaviour, Matrix Production, and Gene Expression of Human Osteoblasts in Defined Cylindrical Titanium Channels. *Journal of Biomedical Materials Research.* 2004, roč. 68, č. 2, pp. 325–334.

33. BAEL VAN, S.; CHAI Y, C; TRUSCELLO, S; MOESEN, M; KERCKHOF, G; OOSTERWYCK VAN, H; KRUTHA J, P; SCHROOTENC, J. The Effect of Pore Geometry on the In Vitro Biological Behaviour of Human Periosteumderived Cells Seeded on Selective Laser-melted Ti6Al4V Bone Scaffold. *Acta Biomaterialia.* 2012, roč. 8, č. 7, pp. 2824–2834.

34. SHAH, F. A.; SNIS, A.; MATIC, A.; THOMSEN, P.; PALMQUIST, A. 3D printed Ti6Al4V implant surface promotes bone maturation and retains a higher density of less aged osteocytes at the bone-implant interface. *Acta biomaterialia*. 2016, roč. 30, č. -, pp. 357–367.

35. ŘEHOUNEK, Luboš; JÍRA, Aleš; HÁJKOVÁ, Petra; ČEJKA, Zdeněk. *Optimalizace 3D tištěných trabekulárních struktur pro potřeby implantologie a jejich mechanické analýzy*. 2017. Nepublikovaná zpráva z projektu TAČR č. TJ01000328.

36. SCHOEN, A. H. *Infinite periodic minimal surfaces without self-intersections*. 1970. NASA Technical Report.

37. JÍRA, A.; ŘEHOUNEK, L.; JAVORSKÁ, G. Variability of the Gyroid Structure for Biomedical Applications. In: *59th International Scientific Conference on Experimental Stress Analysis*. Litomyšl, Czech Republic, 2021.

38. JÍRA, Aleš; ŘEHOUNEK, Luboš; JAVORSKÁ, Gabriela; PADEVĚD, Pavel. Experimental investigation of defects of thin 3D-printed plates. In: *60th Annual Conference on Experimental Stress Analysis*. Prague, Czech Republic, 2022.

39. ZHU, Xian-Kui; JOYCE, James A. Review of fracture toughness (G, K, J, CTOD, CTOA) testing and standardization. *Engineering fracture mechanics*. 2012, roč. 85, pp. 1–46.

40. LI, Guodong; AN, Qi; DUAN, Bo; BORGSMILLER, Leah; AL MALKI, Muath; AGNE, Matthias; AYDEMIR, Umut; ZHAI, Pengcheng; ZHANG, Qingjie; MOROZOV, Sergey I et al. Fracture toughness of thermoelectric materials. *Materials Science and Engineering: R: Reports*. 2021, roč. 144, p. 100607.

41. SODERHOLM, Karl-Johan. Review of the fracture toughness approach. *Dental Materials*. 2010, roč. 26, č. 2, e63–e77.

42. BORST, Rene de. Fracture in quasi-brittle materials: a review of continuum damage-based approaches. *Engineering fracture mechanics*. 2002, roč. 69, č. 2, pp. 95–112.

43. TORIBIO, J; ÁLVAREZ, N; GONZÁLEZ, B; MATOS, JC. A critical review of stress intensity factor solutions for surface cracks in round bars subjected to tension loading. *Engineering Failure Analysis*. 2009, roč. 16, č. 3, pp. 794–809.

44. ANTOLOVICH, Stephen D; SAXENA, Ashok; GERBERICH, William W. Fracture mechanics–An interpretive technical history. *Mechanics Research Communications*. 2018, roč. 91, pp. 46–86.

45. POOK, LP. The linear elastic analysis of cracked bodies and crack paths. *Theoretical and Applied Fracture Mechanics*. 2015, roč. 79, pp. 34–50.

46. LEE, YUNG-LI; PAN, JWO; HATHAWAY, RICHARD B.; BARKEY, MARK E. (ed.). 6 - FRACTURE MECHANICS and FATIGUE CRACK PROPAGATION. In: *Fatigue Testing and Analysis*. Burlington: Butterworth-Heinemann, 2005, pp. 237–284.

47. ROYLANCE, David. Introduction to fracture mechanics. 2001.

48. PATIL, Sandeep P; HEIDER, Yousef. A review on brittle fracture nanomechanics by all-atom simulations. *Nanomaterials*. 2019, roč. 9, č. 7, p. 1050.

49. EINAV, Itai. Fracture propagation in brittle granular matter. *Proceedings of the Royal Society A: Mathematical, Physical and Engineering Sciences*. 2007, roč. 463, č. 2087, pp. 3021–3035.

50. PEREZ, Nestor; PEREZ, Nestor. Introduction to fracture mechanics. *Fracture Mechanics*. 2017, pp. 53–77.

51. ANDERSON, Ted L. *Fracture mechanics: fundamentals and applications*. CRC press, 2017.

52. TAYLOR, David; CORNETTI, Pietro; PUGNO, Nicola. The fracture mechanics of finite crack extension. *Engineering fracture mechanics*. 2005, roč. 72, č. 7, pp. 1021–1038.

53. BROBERG, KB. Critical review of some theories in fracture mechanics. *International Journal of Fracture Mechanics*. 1968, roč. 4, pp. 11–19.

54. MAITI, Surjya Kumar. *Fracture mechanics: fundamentals and applications*. Cambridge University Press, 2015.

55. SAXENA, Ashok. *Basic Fracture Mechanics and Its Applications*. CRC Press, 2022.

56. GDOUTOS, Emmanuel E. *Fracture mechanics: an introduction*. Sv. 263. Springer Nature, 2020.

57. BRUNET, Joseph; PIERRAT, Baptiste; BADEL, Pierre. Review of current advances in the mechanical description and quantification of aortic dissection mechanisms. *IEEE Reviews in Biomedical Engineering*. 2020, roč. 14, pp. 240–255.

58. AYATOLLAHI, MR; ZAKERI, M. An improved definition for mode I and mode II crack problems. *Engineering fracture mechanics*. 2017, roč. 175, pp. 235–246.

59. CHRISTOPHER, CJ; JAMES, MN; PATTERSON, EA; TEE, KF. Towards a new model of crack tip stress fields. *International Journal of Fracture*. 2007, roč. 148, pp. 361–371.

60. ATKINSON, C; CRASTER, RV. Theoretical aspects of fracture mechanics. *Progress in Aerospace Sciences*. 1995, roč. 31, č. 1, pp. 1–83.

61. RADAJ, D. State-of-the-art review on extended stress intensity factor concepts. *Fatigue & Fracture of Engineering Materials & Structures*. 2014, roč. 37, č. 1, pp. 1–28.

62. MIANNAY, Dominique P. *Fracture mechanics*. Springer Science & Business Media, 1997.

63. *Kovové materiály - Stanovení lomové houževnatosti při rovinné deformaci*. Český normalizační institut, 2011. Č. ČSN EN ISO 12737 (42 0348).

64. SCHNEIDER, Johannes; KUMAR, S. Multiscale characterization and constitutive parameters identification of polyamide (PA12) processed via selective laser sintering. *Polymer Testing*. 2020, roč. 86, p. 106357.

65. SALAZAR, A; RICO, A; RODRÍGUEZ, J; ESCUDERO, J Segurado; SELTZER, R; ESCALERA CUTILLAS, F Martin de la. Monotonic loading and fatigue response of a bio-based polyamide PA11 and a petrol-based polyamide PA12 manufactured by selective laser sintering. *European polymer journal*. 2014, roč. 59, pp. 36–45.

66. LINUL, Emanoil; MARSAVINA, Liviu; STOIA, Dan Ioan. Mode I and II fracture toughness investigation of Laser-Sintered Polyamide. *Theoretical and Applied Fracture Mechanics*. 2020, roč. 106, p. 102497.

67. ZHAO, Jianlong; SANG, Yong; DUAN, Fuhai. The state of the art of two-dimensional digital image correlation computational method. *Engineering reports*. 2019, roč. 1, č. 2, e12038.

68. *PA12 Smooth - Material's Technical Data Sheet*. 2022. Tech. rep. Sinterir sp. z o.o.

69. LAMMENS, Nicolas; KERSEMANS, Mathias; DE BAERE, Ives; VAN PAE-PEGEM, Wim. On the visco-elasto-plastic response of additively manufactured polyamide-12 (PA-12) through selective laser sintering. *Polymer Testing*. 2017, roč. 57, pp. 149–155.

70. COBIAN, L; RUEDA-RUIZ, M; FERNANDEZ-BLAZQUEZ, JP; MARTI-NEZ, V; GALVEZ, F; KARAYAGIZ, F; LÜCK, T; SEGURADO, J; MONCLUS, MA. Micromechanical characterization of the material response in a PA12-SLS fabricated lattice structure and its correlation with bulk behavior. *Polymer Testing*. 2022, roč. 110, p. 107556.

71. SALAZAR, A; CANO, AJ; RODRÍGUEZ, J. Mechanical and fatigue behaviour of polyamide 12 processed via injection moulding and selective laser sintering. Analysis based on Kitagawa-Takahashi diagrams. *Engineering Fracture Mechanics*. 2022, roč. 275, p. 108825.

72. CANO, AJ; SALAZAR, A; RODRÍGUEZ, J. Effect of temperature on the fracture behavior of polyamide 12 and glass-filled polyamide 12 processed by selective laser sintering. *Engineering Fracture Mechanics*. 2018, roč. 203, pp. 66–80.